DISSERTATION

Search for dark sector physics and performance of the Belle II detector in final state events with muons and large missing energy

zur Erlangung des akademischen Grades

Doktor der Technischen Wissenschaften

im Rahmen des Studiums

Technische Physik

eingereicht von

Michel Bertemes, MSc

Matrikelnummer: 11838925

ausgeführt am Atominstitut

der Fakultät für Physik der Technischen Universität Wien

in Zusammenarbeit mit dem

Institut für Hochenergiephysik der Österreichischen Akademie der Wissenschaften

Betreuung : Privatdoz. Dipl.-Ing. Dr. techn. Christoph Schwanda

Mitbetreuung : Dr. Gianluca Inguglia

Wien, am 9. September 2021

Unterschrift StudentIn

Unterschrift BetreuerIn

Kurzfassung

Diese Arbeit handelt von der Suche nach Physik des dunklen Sektors in Ereignissen mit Myonen und großer fehlender Energie. Für die verschiedenen Analysen werden Datensätze vom Belle II Experiment verwendet, welches sich am Elektron-Positron Beschleuniger SuperKEKB in Tsukuba (Japan) befindet. Die erste Studie befasst sich mit der gleichzeitigen Erzeugung eines dunklen Photons A', sowie eines dunklen Higgs h' in der so-genannten dunklen Higgsstrahlung $e^+e^- \to A'h'$; $A' \to \mu^+\mu^-$ und $h' \to$ invisible. In einem zuvor unerforschten Bereich werden obere Schranken für den Mischparameter und die Kopplungsstärke $\epsilon^2 \times \alpha_D$ im 90% Konfidenzintervall berechnet. Weiterhin wird nach dem unsichtbaren Zerfall eines Z' Bosons in dem Prozess $e^+e^- \to \mu^+\mu^- Z'$ gesucht. Dieses gehört zu einer abelschen Eichsymmetrie, welche auf der $L_\mu - L_\tau$ Zahl basiert und verschiedene Anomalien der Flavor Physik erklären könnte. Für dessen Kopplungskonstante g' werden obere Schranken im 90% Konfidenzintervall berechnet. Die Leistung des Belle II Trigger-Systems bezüglich der genannten Ereignisse wird zusätzlich evaluiert.

Abstract

This thesis presents two different searches for dark sector mediators in final state events consisting of a pair of muons and large missing energy. Both searches are performed using data collected at the Belle II experiment which is located at the SuperKEKB e^+e^--accelerator in Tsukuba, Japan. A first analysis is looking for the simultaneous production of a dark photon A' and a dark Higgs h' in the so-called Dark Higgsstrahlung process $e^+e^- \to A'h'$; $A' \to \mu^+\mu^-$ and $h' \to$ invisible. 90% CL upper limits on the product of mixing parameter times dark coupling constant $\epsilon^2 \times \alpha_D$ are set in a fully unexplored region, greatly extending the mass range investigated by the KLOE experiment. Another project focuses on the first search for the invisible decay of a Z' in the process $e^+e^- \to \mu^+\mu^- Z'$. This neutral boson belongs to an Abelian symmetry indicated as $L_\mu - L_\tau$ and may explain different flavor anomalies. Upper limits are set at the 90% CL on the g' coupling constant. Finally, the performance of the Belle II trigger system in identifying the studied low multiplicity events is evaluated.

Contents

I. Preliminaries **3**

1. Theory **5**
1.1. Standard Model . . . 5
1.2. Dark Matter . . . 6
1.2.1. Dark Higgsstrahlung . . . 9
1.2.2. Invisible Z' . . . 12

2. SuperKEKB and Belle II **15**
2.1. SuperKEKB . . . 15
2.2. Belle II . . . 16
2.2.1. VXD . . . 17
2.2.2. CDC . . . 19
2.2.3. PID . . . 19
2.2.4. ECL . . . 21
2.2.5. KLM . . . 22
2.2.6. Trigger system . . . 22

II. Physics Performance **27**

3. Trigger performance studies **29**
3.1. Introduction . . . 29
3.2. Data samples and event selection . . . 30
3.3. Performance Overview . . . 30
3.3.1. CDC . . . 30
3.3.2. KLM . . . 33
3.4. TSIM . . . 37
3.4.1. Activation curve . . . 37
3.4.2. Dependencies . . . 38
3.4.3. Overall efficiency . . . 38
3.5. Dark Sector . . . 40
3.6. Additional tables . . . 42

III. Physics Analysis **45**

4. Dark Higgsstrahlung **47**
4.1. Analysis overview . . . 47
4.2. Data sets . . . 48
4.3. Candidate reconstruction . . . 49
4.4. Event selection . . . 50
4.4.1. Preselections . . . 50
4.4.2. Mass windows . . . 52
4.4.3. Final background suppression . . . 55
4.4.4. Selection optimization . . . 59
4.5. Signal resolution studies . . . 61
4.6. Data validation . . . 64
4.6.1. Data validation in macro regions . . . 67
4.6.2. Data validation of background shapes after preselections . . . 68
4.6.3. Data validation of the A_E selection . . . 71
4.7. Systematic uncertainties . . . 74
4.7.1. Mass resolution . . . 75
4.7.2. muonID effects . . . 82
4.7.3. Preselection effects . . . 83
4.7.4. Results . . . 84
4.8. Statistical interpretation . . . 85
4.8.1. Look-Elsewhere-Effect . . . 86
4.9. Results and Outlook . . . 91

5. Z' to invisible **93**
5.1. Analysis overview . . . 93
5.2. Data sets . . . 94
5.3. Candidate reconstruction . . . 94
5.3.1. Standard Z' to invisible . . . 94
5.3.2. LFV Z' to invisible . . . 95
5.4. Event selection . . . 95
5.4.1. Standard Z' . . . 95
5.4.2. Mass windows and tau suppression . . . 96
5.4.3. LFV Z' . . . 97
5.5. Signal resolution studies . . . 101
5.6. Detector effects and systematic uncertainties . . . 104
5.6.1. Trigger selection . . . 104
5.6.2. Tracking efficiency . . . 104
5.6.3. Particle ID selection . . . 104
5.6.4. Recoil mass resolution . . . 104
5.7. Data validation . . . 107
5.7.1. ee sample . . . 108
5.7.2. $\mu\mu\gamma$ sample . . . 108

5.7.3. Reversed tau suppression sample 110
5.7.4. Data validation summary 110
5.8. Statistical interpretation 114
5.9. Results and Outlook 115
5.9.1. Standard Z' 116
5.9.2. LFV Z' 116
5.9.3. Outlook 116

Bibliography **i**

Introduction

The Standard Model is the most rigorous theory of particle physics. With its great predictive power, it has passed many precision tests and provides an adequate description of the building blocks of nature: six quarks, six leptons, four force-carrier particles, and the Higgs boson, governed by the electromagnetic, weak and strong forces. Despite its many successes, the Standard Model is not complete and fails to address five crucial issues.

Like photons, neutrinos should be massless. However, the different neutrino states were found to oscillate into each other, which is only possible if they have mass after all. In addition, the Standard Model does not include gravity, while the latter is observed to have no impact on subatomic interactions. The question therefore arises, if there could be a new particle associated with the force of gravity. When the Universe was formed in the Big Bang, matter and antimatter should have been produced in equal parts. Today, the Universe is dominated by matter and the imbalance cannot be explained by the Standard Model. The latest measurements indicate that the Universe's expansion is speeding up: This is believed to be caused by an unexplained property of space-time called dark energy, that supposedly makes up around 69 percent of the energy in the Universe. Finally, the presence of dark matter has been inferred from the angular velocities of galaxies. In fact, they are rotating so fast that the gravity generated by their observable matter could not hold them together on its own. Dark matter, which has yet to be detected directly, must be giving additional mass and hence generating the extra gravity for the galaxies to stay intact. It is not included in the Standard Model, but thought to make up 26 percent of the contents of the universe. In order to study the origin of dark matter, various experiments search for interactions of dark matter with ordinary matter.

The SuperKEKB accelerator, located in Tsukuba (Japan), is colliding electrons and positrons on a circumference of 3 km. At the interaction point of the two beams, there is the Belle II experiment, which is measuring the particle collisions with the highest precision. Belle II started data taking in 2019 with the aim of collecting a data set of unprecedented integrated luminosity. Different extensions to the Standard Model are foreseen, in which a mediator acts as a portal to the dark sector while also coupling to the known Standard Model particles. If assumed to be light enough, these mediators could be produced at Belle II. They would however not interact with the detector material and escape unnoticed, while their existence could be inferred from the amount of energy and momentum they carry away.

My thesis is structured as follows: In the first Part I, I introduce two different dark sector mediators, and provide a more detailed description of SuperKEKB and Belle II, while the second Part II summarizes the results of a physics performance study of the Belle II trigger system, leading to the main Part III where I elaborate two different

searches for dark sector mediators with data collected by Belle II.

Part I.

Preliminaries

1. Theory

1.1. Standard Model

Particle Physics is concerned with the fundamental constituents of the Universe, elementary particles and the interactions between them, the forces. Our current understanding is embodied in the Standard Model (SM), which provides a mathematical description of the particle interactions and the underlying dynamics. In atoms, negatively charged electrons (e^-) orbit around a central nucleus consisting of positively charged protons and electrically neutral neutrons. They are bound to the nucleus by the electrostatic attraction between opposite charges, a manifestation of Quantum Electrodynamics (QED), the fundamental theory of electromagnetism. As what concerns the protons and neutrons in the nucleus, it is the strong nuclear force that binds them together, described by the theory of Quantum Chromodynamics (QCD). The weak force, which is responsible for nuclear β-decays of radioactive isotopes and nuclear fusion processes in the Sun, is the third type of fundamental particle interaction. In both of the aforementioned processes, another particle, the electron neutrino (ν_e) is produced. Most of the physical phenomena can be described in terms of electron, electron neutrino, proton and neutron interacting via electromagnetic, weak and strong force. At larger energy scales, proton and neutron are found to be bound states of quarks, with the proton consisting of two up-quarks and a down-quark (uud), and the neutron consisting of two down-quarks and an up-quark (udd). Finally, there is gravity, which is relevant for large-scale structure formation in the Universe.

Electron, electron neutrino, up- and down-quark are referred to as the first generation of elementary particles. They represent the building blocks of the Universe. For each of the four first-generation particles, there are exactly two copies, which differ only in their masses. The additional eight particles make up the second and third generations. For example, the muon (μ^-) and tau (τ^-) can be seen as a heavier version of the electron with masses $m_\mu \approx 200 m_e$ and $m_\tau \approx 3500 m_e$ respectively. On the other hand, the masses of the different neutrinos are sufficiently small and have yet to be determined. The most recent upper limits predict the associated values to be at the order of eV. Electron, muon, tau and their respective neutrinos are collectively referred to as leptons. All twelve quarks and leptons undergo weak interactions. With the exception of neutrinos, which are electrically neutral, the remaining nine particles participate in the electromagnetic interactions of QED. In QCD, the equivalent of electric charge is called color charge and is solely carried by quarks. It is therefore only the latter that interact via the strong force. Due to the nature of QCD, quarks are never observed as free particles but are always confined to bound states, called hadrons. Both quarks and leptons are spin-half

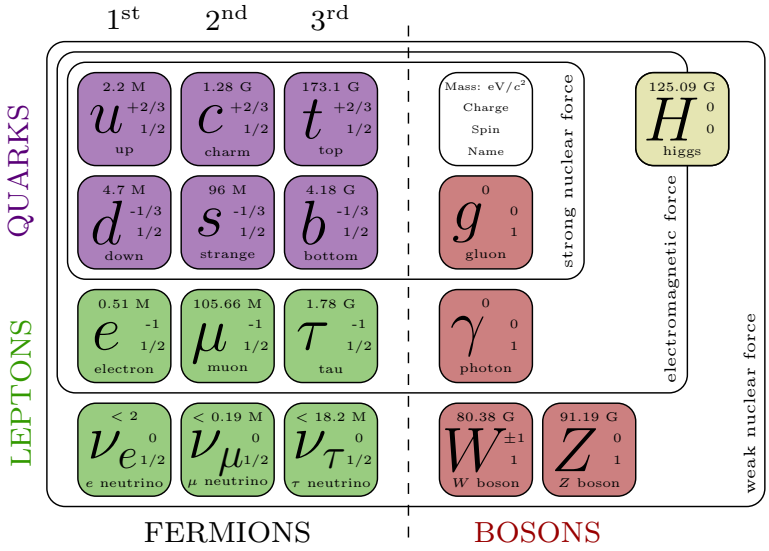

Figure 1.1.: Fundamental particles of the SM and their interactions

particles and can be grouped together as fermions.

In particle physics, each of the three relevant forces are described by a Quantum Field Theory (QFT), corresponding to the exchange of a spin-1 force-carrying particle, referred to as gauge boson. In case of QED, interactions are mediated by the exchange of virtual photons. The gluon, which is massless like the photon, is the force-carrying particle of strong interactions. The weak charged-current is mediated by the charged W^+ and W^- bosons. Finally, there is also the weak neutral-current interaction, mediated by the neutral Z boson. Both Z and W bosons are approximately eighty times more massive than the proton. The mechanism by which all particles acquire mass is provided by the Higgs boson. It plays a special role in the SM. Unlike the fermions and gauge bosons, the Higgs boson is the only fundamental scalar particle discovered to date. In QFT, the Higgs boson can be seen as an excitation of the Higgs field. In opposite to the fields associated to the fundamental fermions and bosons, the Higgs field has a non-zero vacuum expectation value. The initially massless particles obtain their mass by interacting with this non-zero Higgs field.

An overview of all the fundamental particles and their respective interactions is given in Figure 1.1.

1.2. Dark Matter

The SM is not the ultimate theory of particle physics. Despite its many successes in reproducing experimental results and having passed several precision tests, there are many unanswered questions. Compelling evidence for physics beyond the SM is given by the existence of dark matter. Since the 1930s, it has been known that a significant

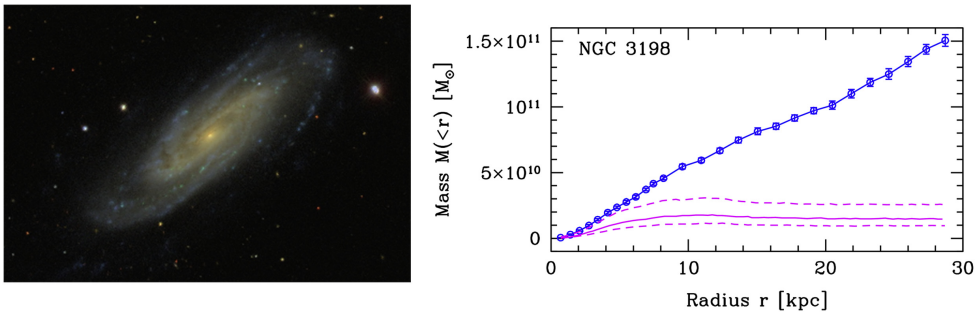

Figure 1.2.: Left: Spiral galaxy NGC 3198, imaged by Sloan Digital Sky Survey. The distance from the centre to the edge of the visible disk is approximately 8 kpc=2.5×10^{19} m. Right: The mass $M(< r)$ enclosed within a radius r as inferred from the distribution of visible stars (pink line) and from rotational velocities of stars (blue data points) [1].

fraction of the mass in the Universe is not bound up in the luminous stars. The galaxy NGC 3198, pictured on the left in Figure 1.2, is a spiral galaxy like the Milky Way, where the majority of the luminous mass is located in the central bulge. While the stars orbit around the centre, it is the gravity of the system that keeps them bound to the galaxy. By equating the centripetal force experienced by an orbiting star of mass m with the gravitational force, one can see that the faster the stars rotate around the centre, the more mass is needed to keep them bound:

$$\frac{mv^2}{r} = \frac{GM(< r)m}{r^2} \rightarrow M(< r) = \frac{v^2 r}{G} \tag{1.1}$$

where G is the gravitational constant, v the velocity of the star orbiting at a radius r, and $M(< r)$ the mass of the galaxy enclosed by the star's orbit. The right panel of Figure 1.2 shows data collected from the NGC 3198 galaxy. The mass $M_*(< r)$ as inferred from the distribution of visible stars, i.e. the stellar mass, is shown in pink with the associated uncertainty indicated in dashed lines. This can be compared to the total mass $M(< r)$, which is depicted in blue and has been computed with Doppler measurements of the rotation speed at different radii and the use of Equation 1.1. While the total mass grows with increasing radius, the stellar mass becomes a constant at roughly 8 kpc, where the visible stellar disk ends. This discrepancy provides strong evidence to support the theory of dark matter.

Further cosmological observations and in particular measurements related to the fluctuations in the cosmic microwave background (CMB) helped in establishing the ΛCDM model, which is the standard model of cosmology. Within the ΛCDM model, the total energy-matter density Ω is equal to the density that gives zero global curvature and hence a flat geometry of space-time. Furthermore, only 5% of Ω are in the form of normal baryonic matter, $\Omega_b \simeq 0.05$. An additional 26% arises from *cold dark matter* (CDM), $\Omega_c \simeq 0.26$, while the majority comes from *dark energy*, $\Omega_\Lambda \simeq 0.69$. The latter is at-

tributed to a non-zero cosmological constant, $\Lambda \neq 0$, that can be included in Einstein's equations of general relativity and tends to accelerate the expansion of the Universe.

Our current understanding of cosmology has reached the level of precision where it now sets constraints on particle physics. Even though there is no impact (yet) from the existence of dark energy, the constraints arising from dark matter are highly relevant. The formation of large-scale structure depends significantly on the particle content in the Universe. Whereas light particles, such as neutrinos, remain relativistic throughout the expansion and cooling of the Universe, massive particles become non-relativistic a few years after the Big Bang. It is therefore known that the majority of the energy-mass density related to dark matter is due to cold (non-relativistic) matter instead of hot and relativistic particles. In addition, the leading theory for the nature of cold dark matter suggests that it is mostly made of non-baryonic particles that only interact with baryons through gravity and the weak nuclear force. These new type of weakly interacting massive particles (WIMP), with masses in the range GeV-TeV, appear in different extensions to the Standard Model, as for example in many supersymmetric models where the lightest supersymmetric particle is the stable weakly interacting neutralino $\tilde{\chi}_1^0$.

WIMPs would interact with matter via elastic scattering with atomic nuclei, i.e $\chi + N \rightarrow \chi + N$. Direct detection experiments attempt to measure the recoil of a nucleus after the scattering process. For WIMP masses greater than 10 GeV, the resulting recoil energies are in the range of 1-10 keV, which is challenging to detect. Two main approaches exist to measure the nuclear recoil: The ionization produced by the recoiling nucleus may be detected by the scintillation light emitted in sodium iodide crystals or liquid noble gas detectors. In cryogenic detectors made of silicon or germanium crystals, particle interactions lead to phonons that can be measured. The local number density of WIMPs is expected to be relatively low, around $n \sim 0.3/m_\chi[\text{GeV}]\text{cm}^{-1}$. In combination with the small weak interaction cross sections, this will lead to low event rates, typically at the order of a few events per year in 10 kg-scale detectors. Finally, backgrounds from natural radioactivity require a careful investigation.

An alternative avenue is given by collider searches, which instead of looking for DM candidates directly, focus on the particles mediating its interactions with the SM. Besides gravity, there are only a few interactions allowed by SM symmetries that provide a *portal* from the SM into the dark sector, depending on mediator spin and parity. A new vector particle A' can couple to a SM current via the vector portal:

$$\mathcal{L} \supset -\frac{\epsilon}{2\cos\theta_W} B_{\mu\nu} F'^{\mu\nu} \tag{1.2}$$

where $B_{\mu\nu} \equiv \partial_\mu B_\nu - \partial_\nu B_\mu$ is the hypercharge field strength tensor, θ_W is the weak mixing angle and $F'_{\mu\nu} \equiv \partial_\mu A'_\nu - \partial_\nu A'_\mu$ is the field strength of a dark vector boson, referred to as *dark photon*.

A new scalar particle S can couple to the SM Higgs field H via the Higgs portal:

$$\mathcal{L} \supset (\mu S + \lambda S^2) H^\dagger H \tag{1.3}$$

The neutrino portal provides another option:

$$\mathcal{L} \subset y_N L H N \tag{1.4}$$

where N is a fermionic mediator with Yukawa coupling y_N, H is again the SM Higgs doublet and L a lepton doublet of any generation.

Whereas these first three operators are renormalizable (dimension-4), the axion portal, with a pseudo-scalar a, is dimension-5 and suppressed by some (high) mass scale f_A.

$$\mathcal{L} \supset \frac{a}{f_A} F_{\mu\nu} \tilde{F}^{\mu\nu} \tag{1.5}$$

where $F_{\mu\nu}(\tilde{F}_{\mu\nu})$ is the (dual) field-strength tensor of the SM photon field.

As mentioned above, each of these new particles can act as a mediator between SM and another (stable) particle in the dark sector. The role of the mediator consists of keeping the DM particle in thermal equilibrium with the SM in the early Universe in order to reproduce the observed DM relic abundance via thermal freeze-out and the associated annihilation processes. Depending on the structure of the model, the mediator may then either couple only to quarks (leptophobic), or only to leptons (leptophilic) or both of them. (Pseudo)scalar mediators can couple in addition to fermions proportional to their mass. In opposite to DM candidates from portal interactions, mediators may have sizeable couplings to SM, that can possibly be probed in particle physics experiments. I now present and discuss two different models and how they can be searched for at electron-positron colliders, such as the SuperKEKB accelerator and the Belle II experiment (see Chapter 2).

1.2.1. Dark Higgsstrahlung

The vector portal, with kinetic mixing of a new $U(1)'$ gauge field with hypercharge $U(1)_Y$, stands out in terms of current detection capabilities, as it implies a renormalizable coupling with the photon and the Z boson, whose properties are well-measured. The kinetic mixing parameter ϵ is well-constrained and expected to be at the order of $10^{-4} - 10^{-2}$, so that effects can be observed at both colliders and fixed target experiments operated in the GeV region. While several searches for the dark photon A' have been performed in recent years, no excess was observed, resulting in upper limits for ϵ (shown in Figure 1.3): A1 [2, 3], APEX [4], WASA [5], HADES [6], KLOE [7, 8, 9, 10, 11], BaBar [12], BESIII [13], LHCb [14].

I will now present the minimal implementation of such a secluded $U(1)'$, based on [16]. In addition to the $U(1)'$ gauge boson A', a dark Higgs field ϕ responsible for spontaneous symmetry breaking is introduced. This new sector is not charged under the SM, so that all interactions proceed through kinetic mixing of A' with the photon (mixing with Z will be ignored in the following). The Lagrangian then takes the form:

$$\mathcal{L} = -\frac{1}{4} F'^2_{\mu\nu} - \frac{\epsilon}{2} F'_{\mu\nu} F^{\mu\nu} + |D_\mu \phi|^2 - V(\phi) \tag{1.6}$$

where $F_{\mu\nu}$, $F'_{\mu\nu}$ are the photon and dark photon field strengths respectively, and the covariant derivative is $D_\mu = \partial_\mu + ie' A'_\mu$ with $U(1)'$ charge e'. When neglecting mixing with the SM Higgs (irrelevant for low-energy colliders), the dark Higgs potential can be defined as $V(\phi) = -\mu^2 |\phi|^2 + \lambda |\phi|^4$, and the dark Higgs acquires a vacuum expectation

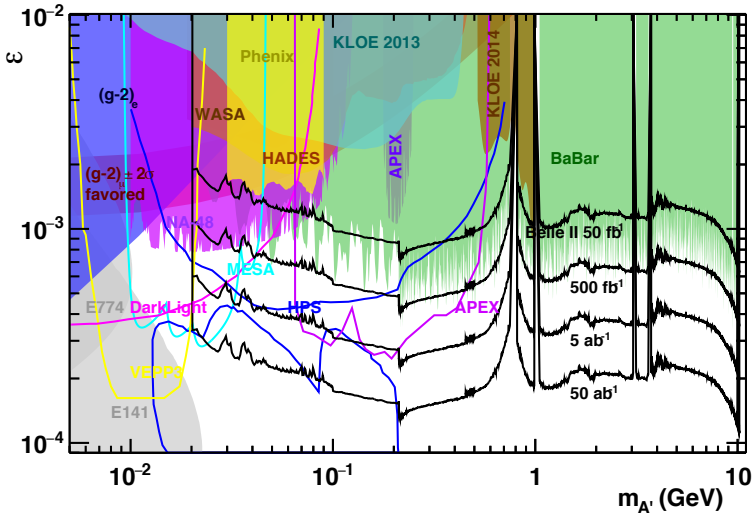

Figure 1.3.: Existing exclusion regions on the kinetic mixing parameter ϵ and dark photon mass $m_{A'}$ for $A' \to l\bar{l}$, [15]

value $\langle\phi\rangle = v'/\sqrt{2}$ with $v' = \sqrt{\mu^2/\lambda}$. After expanding around $\phi = (v' + h')/\sqrt{2}$, the unitary-gauge Lagrangian containing the physical dark Higgs field h' is obtained to be:

$$\mathcal{L} = -\frac{1}{4}F'^2_{\mu\nu} + \frac{1}{2}m^2_{A'}A'^2_\mu + \frac{1}{2}(\partial_\mu h')^2 - \frac{1}{2}m^2_{h'}h'^2_\mu + \mathcal{L}_{int} \tag{1.7}$$

where $m_{A'} = e'v'$ and $m_{h'} = \sqrt{2\lambda}v'$. The interactions terms are:

$$\mathcal{L}_{int} = -\frac{\epsilon}{2}F'_{\mu\nu}F^{\mu\nu} + \frac{m^2_{A'}}{v'}h'A'^2_\mu + \frac{m^2_{A'}}{v'^2}h'^2A'^2_\mu - \frac{m^2_{h'}}{2v'}h'^3 - \frac{m^2_{h'}}{8v'^2}h'^4 \tag{1.8}$$

As what concerns the decay widths of A' and h', every final state will consist of SM particles under the assumption that any other state coupled to them is heavy. After mixing with the photon, the A' will decay into SM leptons with partial width:

$$\Gamma_{A'\to l\bar{l}} = \frac{1}{3}\alpha\epsilon^2 m_{A'}\sqrt{1 - \frac{4m_l^2}{m^2_{A'}}}\left(1 + \frac{2m_l^2}{m^2_{A'}}\right) \tag{1.9}$$

If $m_{A'} > 2m_\pi$, A' will also decay into hadrons:

$$\Gamma_{A'\to\text{hadrons}} = \frac{1}{3}\alpha\epsilon^2 m_{A'}\sqrt{1 - \frac{4m_\mu^2}{m^2_{A'}}}\left(1 + \frac{2m_\mu^2}{m^2_{A'}}\right)R(s = m^2_{A'}) \tag{1.10}$$

where $R = \sigma_{e^+e^-\to\text{hadrons}}/\sigma_{e^+e^-\to\mu^+\mu^-}$. The total width and branching ratios for $\epsilon = 10^{-2}$ are shown in Figure 1.4. For the majority of the displayed mass region, the dark photon A' will mostly decay into leptons, unless $m_{A'}$ coincides with a hadronic resonance.

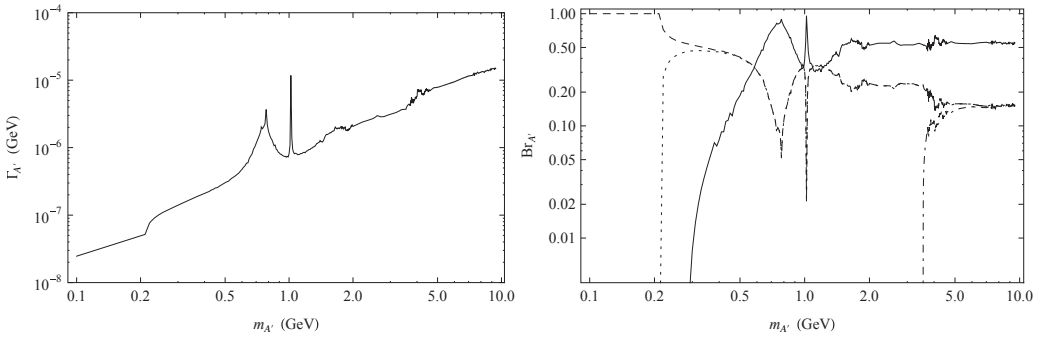

Figure 1.4.: The total width $\Gamma_{A'}$ is shown on the left, while the respective branching ratios for $A' \to e^+e^-$ (dashed), $A' \to \mu^+\mu^-$ (dotted), $A' \to \tau^+\tau^-$ (dot-dashed) and $A' \to$ hadrons (solid) are shown on the right for $\epsilon = 10^{-2}$ and $\alpha_D = \alpha$. [16]

Regarding the decay properties of the dark Higgs h', they strongly depend on the respective relationship in between $m_{A'}$ and $m_{h'}$. If the dark Higgs is heavier than 2 times the dark photon mass, h' will decay into a pair of real dark photons, followed by a subsequent decay into SM particles and a four-particle final state:

$$\Gamma_{h' \to A'A'} = \frac{\alpha_D m_{h'}^3}{8 m_{A'}^2} \sqrt{1 - \frac{4m_{A'}^2}{m_{h'}^2}} \left(1 - \frac{4m_{A'}^2}{m_{h'}^2} + \frac{12 m_{A'}^4}{m_{h'}^4}\right) \tag{1.11}$$

where $\alpha_D = e'^2/4\pi$. If $m_{h'} < m_{A'}$, then the dark Higgs will decay into leptons and hadrons via two off-shell vectors A'^*:

$$\Gamma_{h' \to A'^* A'^*} = \frac{1}{\pi^2} \int_0^{m_h'^2} \frac{dq_1^2 m_{A'} \Gamma_{A'}}{(q_1^2 - m_{A'}^2) + m_{A'}^2 \Gamma_{A'}^2} \int_0^{(m_h' - q_1)^2} \frac{dq_2^2 m_{A'} \Gamma_{A'}}{(q_2^2 - m_{A'}^2) + m_{A'}^2 \Gamma_{A'}^2} \Gamma_0 \tag{1.12}$$

with

$$\Gamma_0 = \frac{\alpha_D m_{h'}^3}{8 m_{A'}^2} \sqrt{\lambda\left(1, \frac{q_1^2}{m_{h'}^2}, \frac{q_2^2}{m_{h'}^2}\right)} \left[\lambda\left(1, \frac{q_1^2}{m_{h'}^2}, \frac{q_2^2}{m_{h'}^2}\right) + \frac{12 q_1^2 q_2^2}{m_{h'}^4}\right] \tag{1.13}$$

and $\lambda(A, B, C) = A^2 + B^2 + C^2 - 2AB - 2AC - 2BC$. If the dark Higgs is light, then loop induced decays become important, with a rate proportional to $\epsilon^4 \times (\text{loop factor})^2$. In the latter case, h' will decay directly into SM particles, leading to a two-particle final state. The total decay width as well as the branching ratios are presented in Figure 1.5 for a dark photon of $m_{A'} = 2\,\text{GeV}$.

The B-factories such as Belle II (see Chapter 2) are particularly well suited to probe this model with their centre-of-mass energies of $\sqrt{s} = 10\,\text{GeV}$ and large integrated luminosities. As the dark photon is observed to be very narrow, single particle resonant production of A' will be very unlikely. I therefore focus on the two-particle production mechanisms. The most promising channel is the dark Higgsstrahlung, $e^+e^- \to A'h'$,

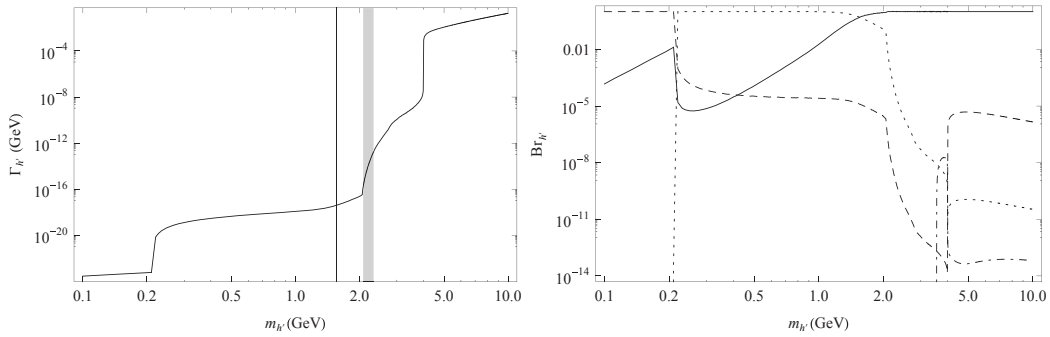

Figure 1.5.: The total width $\Gamma_{h'}$ is shown on the left, while the respective branching ratios for $h' \to e^+e^-$ (dashed), $h' \to \mu^+\mu^-$ (dotted), $h' \to \tau^+\tau^-$ (dot-dashed) and $h' \to A'A'$ (solid) are shown on the right for $\epsilon = 10^{-2}$, $\alpha_D = \alpha$ and $m_{A'} = 2\,\mathrm{GeV}$. The vertical line on the left side indicates the boundary separating two- and four-particle final states. The mass range where the decay distance increases from 1 mm to 1 m, resulting in displaced vertices, is given by the grey band. [16]

which is only minimally suppressed by ϵ^2. The associated Feynman diagram is shown in Figure 1.6, while the total cross section is given by:

$$\sigma_{e^+e^-\to A'h'} = \frac{\pi\alpha\alpha_D\epsilon^2}{3s}\left(1-\frac{m_{A'}^2}{s}\right)^{-2}\sqrt{\lambda\left(1,\frac{m_{h'}^2}{s}\frac{m_{A'}^2}{s}\right)}\left[\lambda\left(1,\frac{m_{h'}^2}{s}\frac{m_{A'}^2}{s}\right)+\frac{12m_{A'}^2}{s}\right] \tag{1.14}$$

According to the values for $m_{A'}$ and $m_{h'}$, the dark Higgsstrahlung process can lead to different experimental signatures. If $m_{h'} > m_{A'}$, the dark Higgs would decay predominantly and promptly into a A' pair, thus giving rise to a six charged particle final state (the scenario with $m_{A'} < m_{h'} < 2m_{A'}$ is similar, with one off-shell A'). This process was searched for by the BaBar [17] and Belle [18] experiment. On the other hand, if $m_{h'} < m_{A'}$, the dark Higgs will be long-lived, escape detection and result in a two leptons plus missing energy signature. This case was only investigated by the KLOE experiment [19], for dark photon masses up to $\simeq 1\,\mathrm{GeV}$. In Chapter 4, I present the measurement of the latter case with the Belle II experiment.

1.2.2. Invisible Z'

In the previous model, I presented the simplest way of extending the SM gauge group: adding a new group $U(1)'$, that is coupled to the SM via kinetic mixing, while the SM fields maintain their complete neutrality with respect to the $U(1)'$. However, one could also think of an alternative approach in which the SM fields carry a charge under the new force. As these models need to be valid up to very high-energy scales, only those anomaly-free combinations remain that gauge $X = yB - \sum_i x_i L_i$ (B is the baryon number, L_i are the individual lepton flavor numbers and y, x_i the constants related to the anomaly-free

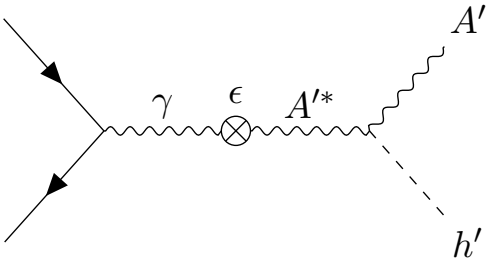

Figure 1.6.: Feynman diagram for the Higgsstrahlung process

requirement $3y = x_e + x_\mu + x_\tau$). The cases where y, $x_e \neq 0$ are well-constrained by previous results from collider and neutrino scattering experiments. On the other hand, the combination $y = x_e$ and $x_\mu = -x_\tau$, gauging the lepton number difference $L_\mu - L_\tau$, makes a compelling case [20, 21]. As it only affects neutrinos and the unstable leptons of the second and third generations, it is well-hidden from most-experiments and more difficult to probe.

This model gives rise to a new vector boson Z', with a mass in the range $M_{Z'} \sim$ MeV $-$ GeV and a coupling $g' \sim 10^{-6} - 10^{-2}$. In addition, it could address open issues in particle physics, such as the anomaly in the muon anomalous magnetic moment [22], and hints for lepton flavor universality violation reported by the LHCb experiment in $b \to s\mu^+\mu^-$ decays [23]. Both these measurements were updated with new results at the time of writing, either confirming and/or increasing the existing tension between experiment and theory. Beyond being able to explain these anomalies, the Z' could also couple to dark matter provided extra matter is charged under the $L_\mu - L_\tau$ symmetry [20, 26]. The mass of the Z' can either be generated by a Stueckelberg mechanism, or by a spontaneous symmetry breaking mechanism as was explained for the previous model. The interaction Lagrangian is given by:

$$\mathcal{L} = \sum_l \theta g' \bar{l} \gamma^\mu Z'_\mu l \tag{1.15}$$

where the index of summation $l = \mu$, τ, $\nu_{\mu,L}$, $\nu_{\tau,L}$ includes the heavy leptons and their respective (left-handed) neutrinos, with $\theta = -1$ if $l = \mu$, $\nu_{\mu,L}$ and $\theta = 1$ if $l = \tau$, $\nu_{\tau,L}$. In Chapter 5, I present the first measurement of the invisible decay topology $e^+e^- \to \mu^+\mu^- Z'$, $Z' \to$ invisible. The Feynman diagram for this process is shown in Figure 1.7, where the Z' production occurs via radiation off a final state muon. Similar searches have already been performed by the BaBar and CMS experiment respectively, both searching for Z' decaying into two muons [24][25]. I obtain the partial decay widths from [26]:

$$\Gamma_{Z' \to l\bar{l}} = \frac{g'^2 M_{Z'}}{12\pi} \left(1 + \frac{2M_l^2}{M_{Z'}^2}\right) \sqrt{1 - \frac{4M_l^2}{M_{Z'}^2}} \tag{1.16}$$

and

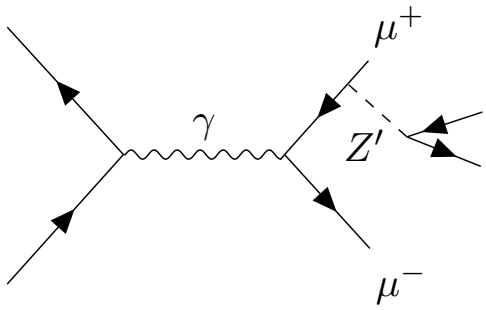

Figure 1.7.: Feynman diagram for the Z' produced along side two muons.

$$\Gamma_{Z' \to \nu_l \bar{\nu}_l} = \frac{g'^2 M_{Z'}}{24\pi} \tag{1.17}$$

The branching fraction for invisible Z' decays is therefore given by:

$$\mathrm{BF}(Z' \to \text{invisible}) = \frac{2\Gamma_{Z' \to \nu_l \bar{\nu}_l}}{2\Gamma_{Z' \to \nu_l \bar{\nu}_l} + \Gamma_{Z' \to \mu^+ \mu^-} + \Gamma_{Z' \to \tau^+ \tau^-}} \tag{1.18}$$

where the branching fraction to one neutrino species is half of the value to one charged lepton flavor. This is due to the fact, that the Z' only couples to left-handed neutrino chiralities whereas it couples to both left- and right-handed charged leptons. The expected branching fractions to neutrino decays are therefore:

$$\begin{aligned} M_{Z'} < 2M_\mu &\implies \mathrm{BF}(Z' \to \text{invisible}) = 1 \\ 2M_\mu < M_{Z'} < 2M_\tau &\implies \mathrm{BF}(Z' \to \text{invisible}) \simeq 1/2 \\ M_{Z'} > 2M_\tau &\implies \mathrm{BF}(Z' \to \text{invisible}) \simeq 1/3 \end{aligned} \tag{1.19}$$

In case decays to dark matter particles $\chi(\bar{\chi})$ become kinematically accessible, i.e. $M_{Z'} > 2M_\chi$, $\mathrm{BF}(Z' \to \chi\bar{\chi})$ is expected to be equal to 1.

2. SuperKEKB and Belle II

Belle II, the next generation of B-factories, is hosted at the High Energy Accelerator Research Organization (KEK) in Tsukuba, Japan. The asymmetric energy collider SuperKEKB accelerates electrons and positrons on a total circumference of 3 km at respective beam energies of 7 and 4 GeV. Located at the interaction point of both beams, the Belle II experiment aims to collect 50 times more data than the precursor Belle did, i.e. $50\,\mathrm{ab}^{-1}$. Belle II has a rich physics program including B and D physics, quarkonium, τ and low mass dark sector [15]. The following chapter will present the main features of SuperKEKB and Belle II.

2.1. SuperKEKB

The SuperKEKB accelerator complex consists of a 7 GeV electron ring (high energy ring, HER), a 4 GeV positron ring (low energy ring, LER) as well as an injector linear accelerator (linac) with a 1.1 GeV positron damping ring, all shown in Figure 2.1 [27].

The target luminosity of SuperKEKB is $6 \times 10^{35}\,\mathrm{cm}^{-2}\,\mathrm{s}^{-1}$, a factor 30 times higher than what was achieved by its predecessor KEKB, which operated until June 2010. This increase in luminosity will be achieved by reducing the beam size at the interaction point (IP) by a factor of 20 from 1 µm to 50 nm and simultaneously increasing the beam currents to 1.5 times the KEKB values. This so-called "nano-beam" scheme was developed by P. Raimondi for the Italian super B factory [28]. In addition, a larger crossing angle of 83 mrad is adopted in comparison to 22 mrad at KEKB. For this collision scheme a new final-focus superconducting magnet system (QCS) was employed. It consists of 8 quadrupoles magnets, 43 corrector magnets and 4 compensation solenoid coils, where the latter ones are used to cancel the effect of the solenoid field of the Belle II detector on the beams. All the QCS magnets are assembled in two cryostats on the left and right side of the IP.

The beam energies are chosen such that the resulting centre-of-mass energy is 10.58 GeV, which is equal to the $\Upsilon(4S)$ mass. While the vast majority of data will be collected at this resonance, the flexibility of the beam energies will allow to cover the full range from just below the $\Upsilon(1S)$ (9.46 GeV) to just above the $\Upsilon(6S)$ (11.24 GeV) for physics operation. The asymmetric beam energies lead to a Lorentz boost of $\beta\gamma = 0.28$ which provides a boost to the centre-of-mass system and in turn allows for time-dependent charge parity measurements. In comparison with KEKB the boost is slightly less ($\beta\gamma = 0.42$), which is advantageous for analyses with missing energies but requires a better vertex resolution.

The commissioning of SuperKEKB was carried out from February to June 2016 without the Belle II detector and QCS. This so-called "Phase 1" is succeeded by different phases

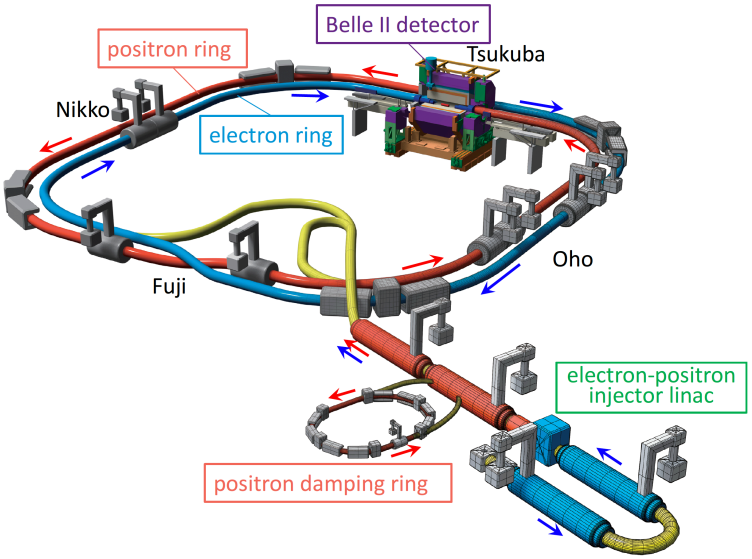

Figure 2.1.: Schematic view of SuperKEKB, showing the electron ring (HER), positron ring (LER) and the Belle II detector located at the IP of the two beams [27]

of data taking:

- Phase 2 represented the first phase of collision data taking and started in March 2018. During a running period of 4 months, SuperKEKB delivered a peak luminosity of $0.5 \times 10^{34}\,\mathrm{cm}^{-2}\,\mathrm{s}^{-1}$ and collected a data set of $0.5\,\mathrm{fb}^{-1}$, which were analysed in the first two physics publications of Belle II. Different background sensors (BEAST [29]) were installed instead of the full vertex detector whose installation only started at the end of Phase 2.

- With the full detector installed, the second collision phase, Phase 3, started in March 2019. So far a data set of $213\,\mathrm{fb}^{-1}$ was collected (July 2021), while SuperKEKB was able to set a new record in instantaneous luminosity of $3.12 \times 10^{34}\,\mathrm{cm}^{-2}\,\mathrm{s}^{-1}$.

2.2. Belle II

The Belle II detector surrounds the interaction region of the HER and LER [30]. It consists of several sub-detectors, dedicated to different tasks such as reconstruction of charged tracks, detection of clusters and particle identification. Figure 2.2 shows a schematic of the Belle II detector. The exact arrangement of the different sub-detectors can be seen in Figure 2.3.

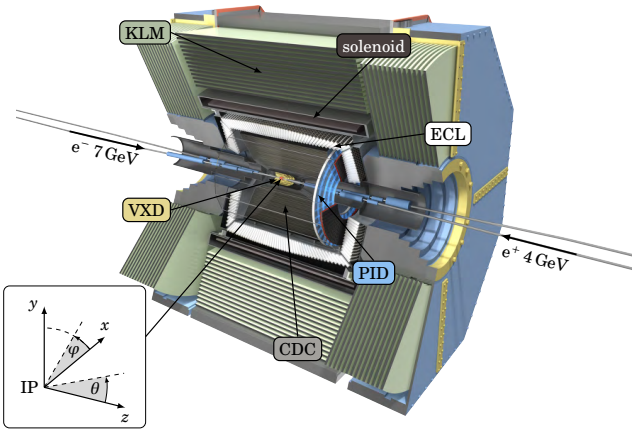

Figure 2.2.: A schematic of the Belle II detector where arrows indicate the different sub-detectors. The coordinate system centred at the IP is shown in addition.

2.2.1. VXD

The sub-detector closest to the interaction point is the Belle II vertex detector (VXD). It plays a fundamental role in the measurement of impact parameters of charged tracks as well as in the reconstruction of primary and secondary decay vertices of B and D mesons. The VXD is composed of two inner layers of pixel detector (PXD) followed by 4 layers of silicon vertex detector (SVD) which are based on depleted p-channel field effect transistor (DEPFET, [31]) and double-sided silicon strip technology respectively. A rendering of the VXD is shown in Figure 2.4.

The PXD consists of two approximately cylindrical layers situated just outside the beam pipe at radii of 14 mm and 22 mm. Two mirrored modules are glued face to face to form a ladder. The inner layer holds eight ladders whereas the outer one holds twelve, leading to a total of 20 ladders and 40 sensors. Altogether the PXD consists of nearly 8 million pixels. Due to a delay in the ladder assembly, only two ladders of the outer layer and the full inner layer are currently installed. The installation of the full PXD is foreseen for the long shutdown in 2022.

The SVD is composed of four layers at radii of 39, 80, 104 and 135 mm respectively. Every layer has a barrel-shaped part with rectangular sensors. In addition, the three outermost layers have a lamp-shade geometry with trapezoidal sensors in the forward direction. The layers consist of 7-16 ladders, with 2 to 5 sensors per ladder, leading to a total of 35 ladders and 172 sensors. Results of the first physics run show a good performance of the SVD with sensor efficiencies at the level of 99% and signal-to-noise ratio between 15 and 30 [33].

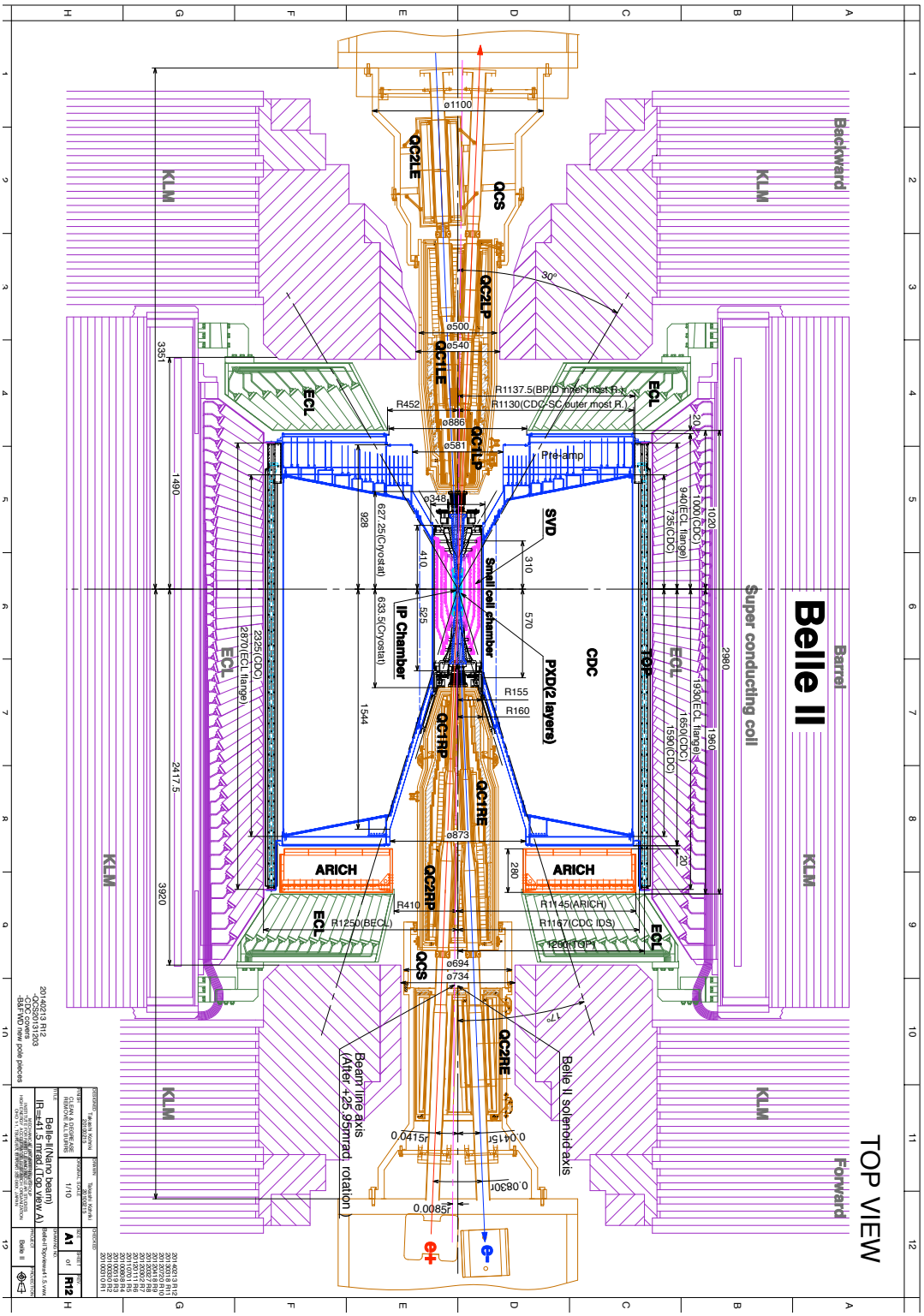

Figure 2.3.: A longitudinal cut of the Belle II detector along the $z - y$ plane, [15]

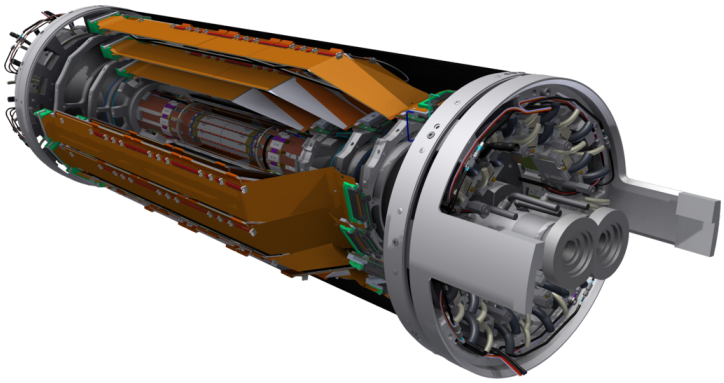

Figure 2.4.: The Belle II vertex detector, the PXD is located at the centre whereas the four outermost layers represent the SVD, [32]

2.2.2. CDC

The outermost tracking detector of Belle II is the central drift chamber (CDC). Charged particles pass through the CDC while ionizing the He-C_2H_6 gas mixture. Charges accumulate at the 14000 sense wires which are arranged in layers. Six or eight adjacent layers form a superlayer as is shown in Figure 2.5. The superlayers alternate between axial (A) and stereo (U,V) orientation, where axial wires are aligned with the beam axis and stereo wires are skewed by an angle between 45.4 and 74 mrad in the positive and negative direction w.r.t the beam axis. Hits in axial and stereo wires can be combined for full 3D track reconstruction. Within the CDC, charged track reconstruction may be performed with high momentum resolution given that it covers the major part of the tracking volume up to $l \times r = 2.3\,\mathrm{m} \times 2.2\,\mathrm{m}$. In addition it allows for particle identification through measurement of the energy loss in the gas volume. This is particularly useful for particles which do not reach the sub-detectors dedicated to particle identification (see Section 2.2.3). Finally it provides trigger signals as described in Section 2.2.6.1.

2.2.3. PID

2.2.3.1. TOP

In the barrel region a time-of propagation counter (TOP) is used for particle identification. It is composed of sixteen modules arranged around the outer wall of the CDC. Each module consists of four different parts: two quartz bars acting as Cherenkov radiator, a mirror at the front end of the bar and a prism that couples the bar to an array of micro-channel-plate photomultiplier tubes (MCP-PMTs). A schematic view of one module is shown in Figure 2.6.

Due to the high refractive index of quartz (n=1.44 at $\lambda = 405\,\mathrm{nm}$), some Cherenkov radiation emitted by the particles travelling through the bar will be trapped by total internal reflection and propagate to the MCP-PMT array. The Cherenkov image is

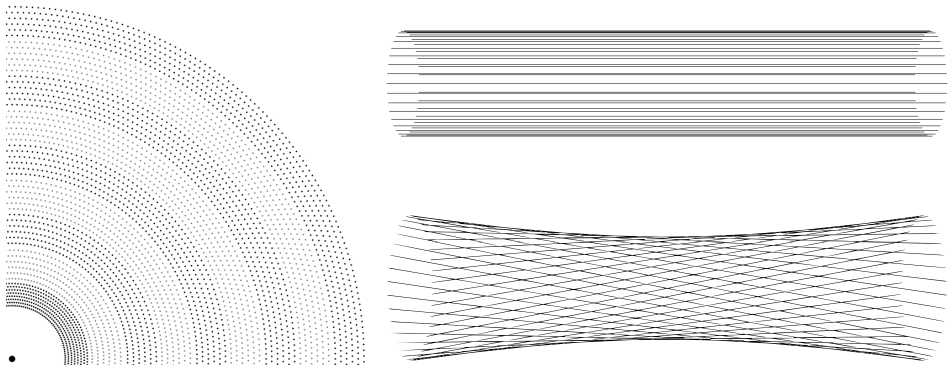

Figure 2.5.: Left: a quadrant of a slice of the $x-y$ projection of the drift chamber. Right: wire orientation for axial (top) and stereo (bottom) layers. [32]

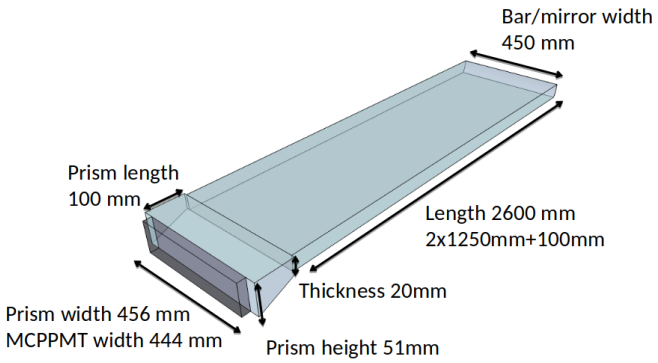

Figure 2.6.: A schematic view of one of the 16 modules of the TOP detector, from [34]

reconstructed by combining the information of the photon position coordinates and the measurement of their detection time. The particle identification information is then extracted by comparing the distribution of photon detection time with the probability density function expected for six different particle hypotheses (e, μ, π, K, p, d). The associated likelihood ratios are used to assign identification probabilities. Early MC simulations show a kaon identification efficiency of 90% with a pion fake rate below 5% in the momentum range between 0.5 and 2 GeV/c. These estimates were confirmed in the Phase II run [34].

2.2.3.2. ARICH

In the forward endcap, the proximity-focusing aerogel ring-imaging Cherenkov detector (ARICH) is the second sub-detector to provide particle identification. It is able to separate pions and kaons in the momentum region from 0.4 to 4 GeV/c. Its main components include aerogel tiles as radiator, an array of position sensitive photon detectors and a

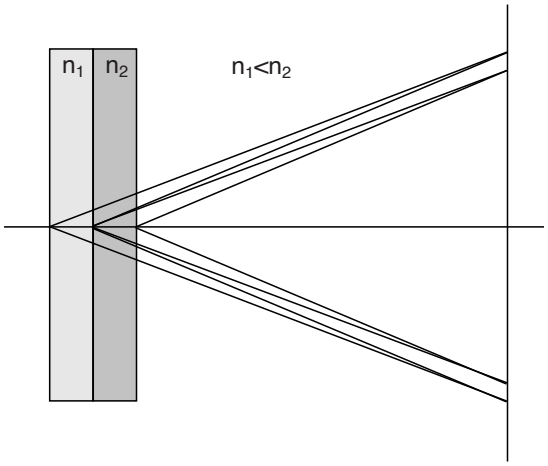

Figure 2.7.: The focusing configuration of ARICH, resulting from the appropriate choice of refractive indices ($n_1 = 1.045$ and $n_2 = 1.055$) from [30]

readout system. The aerogel radiator was chosen to be inhomogeneous, i.e. consisting of multiple layers of varying refractive index in order to increase the number of detected Cherenkov photons and simultaneously avoid the degradation of Cherenkov angle resolution [35]. The refractive indices have been chosen in such a way that corresponding Cherenkov rings from consecutive layers overlap at the photo-detection plane (n=1.045 for upstream and n=1.055 for downstream tiles respectively). Regarding the detection of photons for ARICH, the hybrid avalanche photo-detector (HAPD) which was developed in a joint effort with Hamamatsu is used. It is particularly sensitive to single photon detection, immune to the magnetic field and able to provide position information.

2.2.4. ECL

The main tasks of the electromagnetic calorimeter (ECL) include the detection of photons, the measurement of their energy and position, identification of electrons and generation of trigger signals. It is split into three different detector regions: a barrel section and two annular endcaps (forward and backward) which are instrumented with a total of 8736 thallium-doped caesium iodide CsI(Tl) crystals covering about 90% of the solid angle in the centre-of-mass system. Each crystal is equipped with two photodiodes glued to the rear end. During data-taking the two signals emitted by both photodiodes are first summed then digitized and the resulting waveform is processed online by field-programmable-gate-array's (FPGA's) to measure the magnitude and time of the energy deposit in the crystal. Additional information characterizing the shape of the waveform is also extracted by the FPGA's which allows for pulse shape discrimination (PSD). PSD is an effective method to perform hadron and photon shower separation, and it is the first time applied at an electron-positron collider [36].

2.2.5. KLM

The outermost sub-detector of Belle II is the K_L and muon detector (KLM). Alternating layers of iron plates and active detector elements make up its structure in the two endcaps (forward and backward) and the barrel region (see Figure 2.3). The KLM surrounds the superconducting solenoid which creates a uniform magnetic field of 1.5 T at the centre of the detector.

The detector elements are based on glass-electrode resistive plate chambers (RPC). The glass-electrodes are separated by gas-filled gaps and high voltage is distributed among them. A charged particle passes through the chamber and ionizes the gas molecules along its path, followed by an accelerated motion of the electrons and ions toward the anode and the cathode respectively. This process is amplified by the strong electric field ($4.3\,\mathrm{kV\,mm^{-1}}$) in the gap, leading to more ionizations and a streamer discharge between the electrodes which can be measured. K_L mesons that interact in the iron plates create a hadronic shower that can be detected by the described process.

Under high background rates, the long dead time of the RPCs during the recovery time of the electric field after a discharge will lead to a reduction of the detection efficiency. RPCs have therefore been replaced with layers of scintillator strips and silicon photomultipliers for read-out in the endcaps and the inner two layers of the barrel.

2.2.6. Trigger system

The Belle II trigger system is composed of two consecutive levels: the low level trigger (L1) which is implemented in dead-time-free pipelined hardware, followed by the software based high level trigger (HLT). The common goal is to identify and select events of interest over various sources of beam backgrounds expected from SuperKEKB. The main characteristics of these processes are 1-2 tracks in the CDC and a similar amount of clusters in the ECL. These topologies can therefore mimic those emerging from primary collision events with low multiplicity final states, so that an efficient operation of the trigger system becomes crucial. Flavour measurements including B and D mesons will be less affected by this issue as the studied event signatures include multiple tracks and clusters in the CDC and ECL respectively. The following beam backgrounds are the most dominant in the Belle II environment and will impact the performance of the trigger system:

- *Touschek effect*: The electrons of a particle bunch may scatter off each other, leading to energy deviations inside the bunch and these particles being lost in the beam pipe. In case the loss occurs close to the IP, the resulting shower might reach the active detector material. Horizontal and vertical collimators are therefore placed all around the ring and just before the interaction region to mitigate these effects. At SuperKEKB the effect is enhanced due to the nano-beam scheme. The scattering rate is proportional to the beam bunch current and the number of bunches, and inversely proportional to the beam size and the third power of the beam energy.

- *Beam-gas scattering*: Another background arises from scattering of beam particles by residual gas molecules in the beam pipe. This effect can proceed either via Bremsstrahlung scattering, effectively reducing the energy of the particle or Coulomb scattering which impacts its direction. The expected contribution of this background depends on the beam current, the vacuum pressure in the rings and the material surrounding the magnets. Similar countermeasures as for the Touschek effect are applied.

- *Synchrotron radiation*: Being proportional to the beam energy squared and the magnetic field strength squared, synchrotron radiation (SR) will be mostly emitted by electrons from the HER beam. The inner surface of the beryllium beam pipe is coated with a gold layer to prevent SR photons from reaching the inner detectors (PXD and SVD).

- *Radiative Bhabha process*: Photons produced by the radiative Bhabha process travel along the beam axis and then interact with the iron of the magnets. This leads to a large production of neutrons through the giant resonance process in the nuclei of the magnets. The rate of neutron production is proportional to the luminosity, so that additional shielding is necessary in the accelerator tunnel.

- *Two photon process*: Another luminosity-dependent background is given by the low momentum electron-positron pairs which have been created via the two-photon process $e^+e^- \rightarrow e^+e^-e^+e^-$. These particles may spiral around the solenoid field lines and leave multiple hits in the inner detectors.

2.2.6.1. L1Trigger

The L1 trigger is designed for a maximum average trigger rate of 30 kHz and consists of four sub-detector triggers: CDC, TOP, ECL and KLM. Within a given clock cycle, the different sub-triggers send information of an event to the Global Decision Logic (GDL) which then decides based on the received inputs whether or not to stop the pipeline and send the event to the HLT inside a 5 µs latency window. The CDC sub-trigger finds and characterizes the charged tracks detected by the drift chamber. Energy deposits and single/multiple clusters in the calorimeter are identified by the ECL trigger. Precise timing information is provided by the TOP trigger. Finally the KLM trigger is tracking $\mu\mu$-pair events independently from the CDC sub-trigger. More detailed information is given below:

- Tracking: The 2D track finder of the CDC sub-trigger provides tracks in the transverse $x-y$ plane, namely "full" and "short" tracks (full tracks need to pass through all superlayers, whereas short tracks only need to reach the fourth superlayer). A more detailed description is given in Figure 2.8. In order to reject the aforementioned beam background and in general events which do not originate from the IP, additional information regarding the z-vertex of the event is required (see Figure 2.9). This is provided by the Neural Network trigger which uses the output from

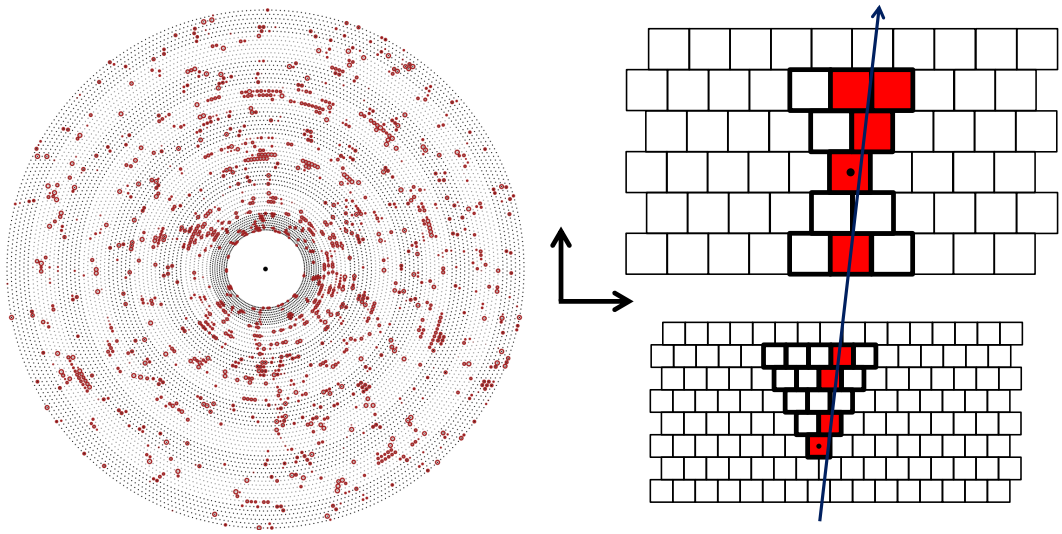

Figure 2.8.: The hits measured by the CDC in case of an event at nominal luminosity are shown on the left. The strategy of the 2D track finder is based on so-called track segments (TS), which are defined by an "hour-glass" shaped arrangement of 5 given layers within a superlayer with a "priority wire" in the centre layer (right: TS for superlayer 0 (bottom), superlayer 1-8 (top), centre wire is indicated with a dot). For every superlayer these TS are predefined to cover the full azimuthal range. A TS hit is registered if at least 4 hits are found in the 5 TS layers. The TSs from superlayers with axial wire orientation are then combined to form 2D tracks using the Hough transformation procedure.

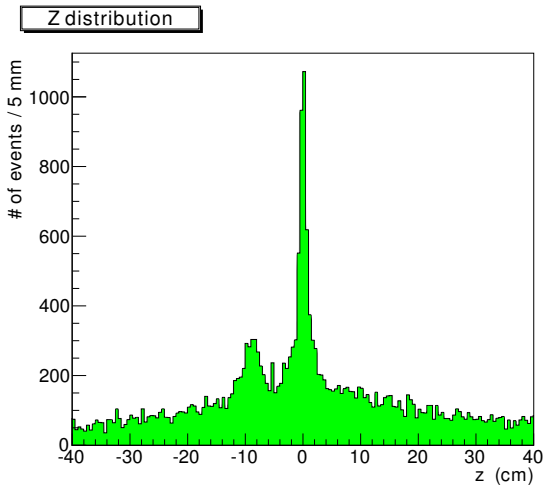

Figure 2.9.: The distribution of the $z-$position of reconstructed vertices at the Belle experiment. The peak at $z = 0\,\text{cm}$ corresponds to signal decays, the wide background is due to the Touschek effect and beam-gas interactions. The peak at $z = -10\,\text{cm}$ is an artefact of the bunch structure.

the 2D track finder and related stereo wire hits to estimate a z-vertex position and polar angle θ for the track. It is implemented in the hardware based on machine learning methods (multilayer perceptron) and provides the "neuro" tracks to the GDL.

- Calorimeter: The background rate from radiative Bhabha scattering will be reduced by exploiting the distinctive event topology of the latter, i.e two clusters in the ECL with energy deposits greater than $3\,\text{GeV}/c$ and a large opening angle in between these clusters in both polar and azimuthal direction. A special 3D Bhabha veto is implemented in the GDL to veto such events based on the selection criteria.

- Trigger menu: The trigger menu consists of many trigger lines aimed at the different physics analysis targets of Belle II. Combinations of full, short and neuro tracks will allow to efficiently trigger on low multiplicity events, while a single photon trigger, which identifies single high energy clusters in the ECL will be used for Dark Sector searches.

2.2.6.2. HLT

Before being stored offline, the registered events will be filtered by the HLT, which is running a software reconstruction and reducing the event rate to 10 kHz. The information of all the sub-detectors contribute to the HLT decision except for the PXD. Long integration times and an overall high data rate prohibit the full storage of all the pixel hits. The reduction of the number of hits is achieved by defining so-called regions of

interest (ROI) which are defined by extrapolating tracks reconstructed by the CDC and SVD back to the PXD plane. Only events within these rectangular areas will be sent to storage.

Part II.

Physics Performance

3. Trigger performance studies

The following work was done solely by the author, while additional guidance was provided by Gianluca Inguglia.

3.1. Introduction

The performance of the L1 trigger system is evaluated for low multiplicity events with data collected by the Belle II experiment in 2019 and 2020. As described in Section 2.2.6.1, there is an abundance of different trigger lines available in the Belle II trigger menu. In the following study, I focus on the CDC track trigger and compute the associated efficiency by using orthogonal trigger lines. Trigger lines are said to be orthogonal when they are fired by essentially different and independent signatures, such as tracks in the CDC or energy deposits in the ECL. One event can fire simultaneously multiple orthogonal trigger lines, if it contains all the information required to fire these same trigger lines. A set of two orthogonal trigger lines δ_i may then be used to calculate the efficiency of one of them (δ_{test}) by assigning the other as reference trigger (δ_{ref}):

$$\epsilon(\delta_{\text{test}}) = \frac{N(\delta_{\text{test}}) \cap N(\delta_{\text{ref}})}{N(\delta_{\text{ref}})} \tag{3.1}$$

where $N(\delta_{\text{test}})$ and $N(\delta_{\text{ref}})$ are the number of events firing the trigger line to be tested and the reference trigger respectively. In particular, I will investigate:

- *hie*: requires a high energy ECL cluster with an energy larger than 1 GeV and the event is not a Bhabha event.
- *ffo*: at least two full tracks (see Section 2.2.6.1) with an opening angle in the transverse plane of $\Delta\phi > 90°$.
- *ff30*: at least two full tracks with an opening angle in the transverse plane of $\Delta\phi > 30°$.
- *mu_ b2b*: two clusters in the KLM located back-to-back and at least two full tracks

The ffo and ff30 trigger lines are tested w.r.t the hie trigger for selected $e^+e^- \to \mu^+\mu^-\gamma$ events, where the γ fires the hie, while ffo is activated by the two μ tracks. In addition, the mu_b2b trigger is evaluated with ffo as reference for selected $e^+e^- \to \mu^+\mu^-$ events. After having established an overview of the performance of the different triggers in data, I repeat the study with simulated data sets and finally analyze the results further in the context of a dark sector analysis.

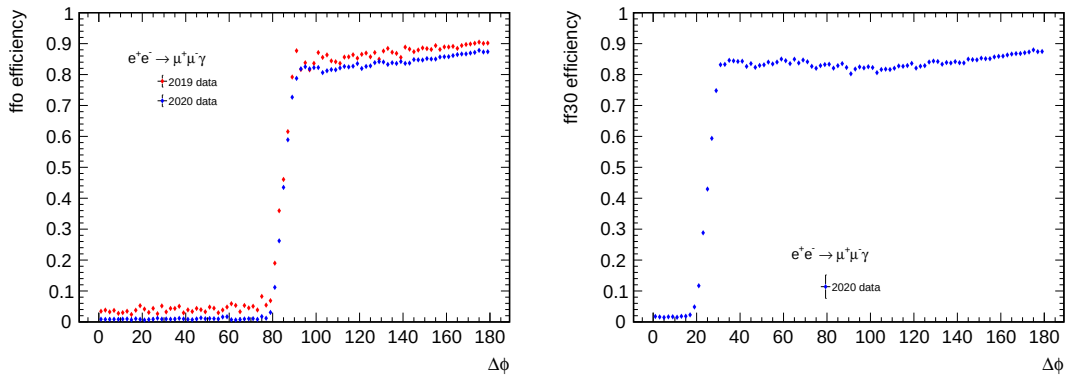

Figure 3.1.: Activation curve of ffo (left) and ffo30 (right) for selected $e^+e^- \to \mu^+\mu^-\gamma$ events

3.2. Data samples and event selection

For this work I use the data collected during 2019 and 2020 with respective integrated luminosities of $8.7\,\mathrm{fb}^{-1}$ and $31.2\,\mathrm{fb}^{-1}$. A few of the trigger lines mentioned above have only been activated in the course of data taking so that only a reduced data set is available for their study. In particular ff30 and mu_b2b have been included in the trigger menu a few months into the 2020 data taking period.

In addition, a Monte Carlo (MC) sample containing $\mu^+\mu^-(\gamma)$ and $\tau^+\tau^-(\gamma)$ events with a size corresponding to the 2019 data set, i.e. $8.7\,\mathrm{fb}^{-1}$, is used for a comparative study. For the reaction $e^+e^- \to \mu^+\mu^-\gamma$, events are selected requiring two "cleaned" tracks originating from the vertex (see Section 4.3). The events are required to fire the hie trigger bit. Both muon tracks are required to be in the ECL barrel region. Photons are selected according to the criteria presented in Section 4.3.

3.3. Performance Overview

3.3.1. CDC

3.3.1.1. Activation curve

The activation curve is a good indication of the overall performance of a trigger line. It is expressed as the efficiency of the trigger line to select events as a function of a variable used by this same trigger line to select or reject events. In case of the ffo and ff30 triggers, the variable in question is the 2D opening angle in azimuthal direction $\Delta\phi$ of the two tracks. The associated activation curves may be seen in Figure 3.1.

The activation curve has the expected shape of a sigmoid function where the activation of the trigger itself can be seen at $\Delta\phi = 90°$ and $30°$ respectively. As what concerns the average efficiency after activation, an overall higher value is reached by ffo in the 2019 data set w.r.t to the 2020 one. This is related to the increase in instantaneous luminosity

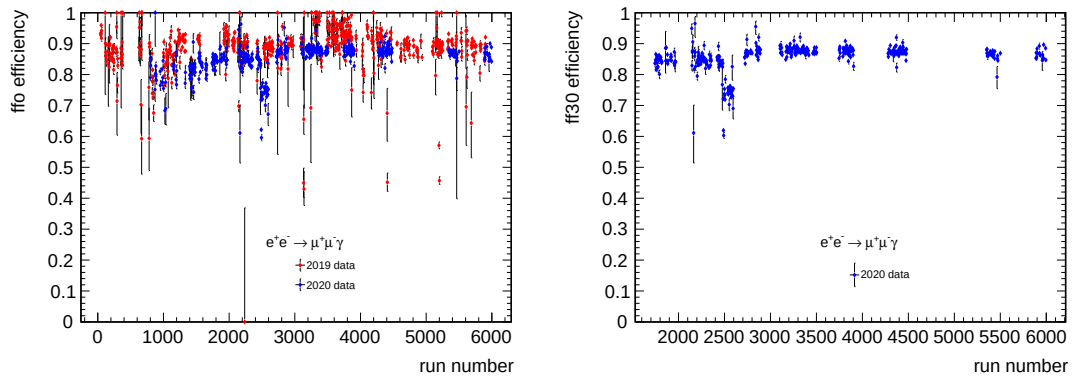

Figure 3.2.: ffo (left) and ff30 (right) efficiency w.r.t. run number for selected $e^+e^- \to \mu^+\mu^-\gamma$ events

of SuperKEKB in 2020, which in turn lead to higher beam background levels (see Section 2.2.6) and thereby decreasing the performance of the trigger system.

3.3.1.2. Dependencies

In order to evaluate possible systematic effects to be considered when using events triggered by ffo and ff30 in physics analyses, I checked the run by run efficiency and the dependencies of the efficiency on kinematic variables such as the track polar angle θ in the laboratory frame and the transverse momentum. Since the trigger efficiency should not depend on these variables, any dependencies will be considered as a systematic effect and will be assigned to the final value of the efficiency that will be provided in Section 3.3.1.3. In fact the plateau efficiency, defined as the average efficiency for two tracks events with an opening angle between the tracks larger than 90° (30°) will be studied in the following. It will be referred to as efficiency from now on.

Run number The run-by-run efficiency of the ffo and ff30 trigger is given in Figure 3.2. I observe an overall efficiency of roughly 86-88%. A few bad runs with efficiencies of less than or equal to 70% are spotted for the 2019 data set with run numbers around 800, 3200, 4400 and 5200 as well as for the 2020 data set with run numbers around 2500. Bad runs can arise from individual sub-detector failures or miscalibrations of processed data. The concerned runs may be excluded for analysis purposes.

Polar angle The efficiency w.r.t the polar angle of track 1 (μ^+) and track 2 (μ^-) is shown in Figure 3.3. For both tracks we observe a slight drop in efficiency for $\cos(\theta)$ values of around 0 and major drops for values approaching -0.6 and 0.8, corresponding to the border of the ECL barrel. Tracks with $\cos(\theta) = 0$ are created by particles travelling on a straight trajectory upwards through the detector and hitting the CDC wires perpendicularly (where the latter are oriented in parallel to the z-axis). Due to this impact

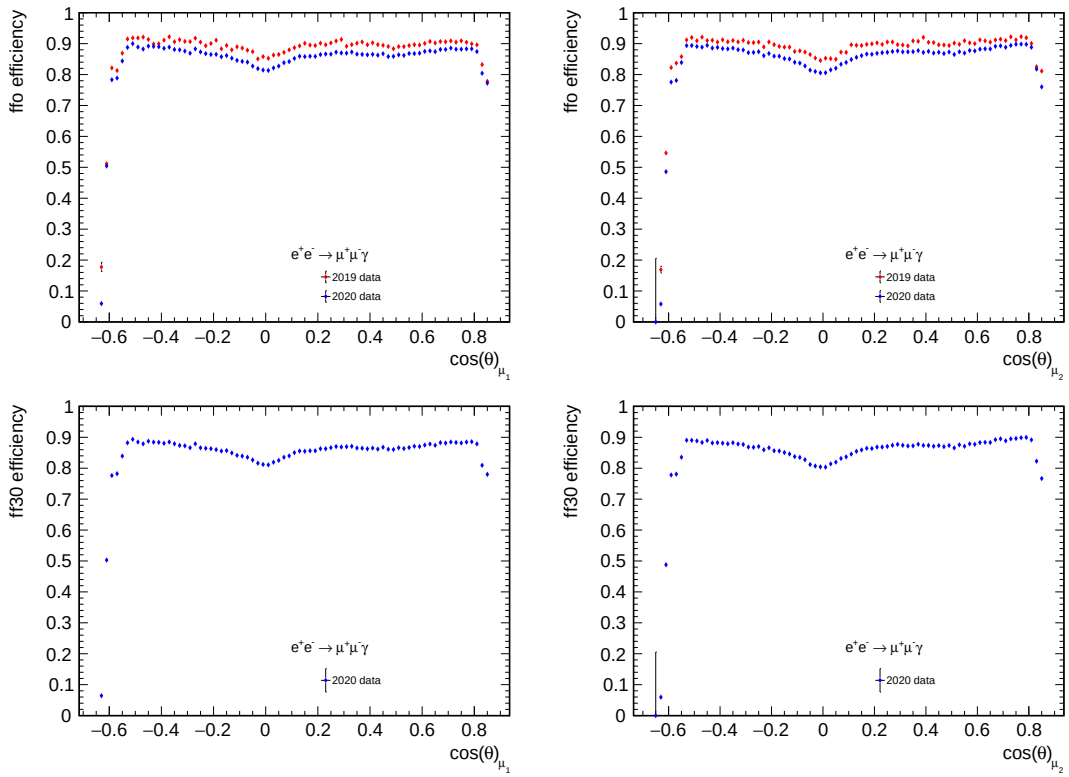

Figure 3.3.: ffo (top) and ff30 (bottom) efficiency w.r.t. $\cos(\theta_{\mu_1})$ and $\cos(\theta_{\mu_2})$ for selected $e^+e^- \to \mu^+\mu^-\gamma$ events

angle, an increased amount of charge can accumulate on the corresponding wire, so that space-charge effects can increase the dead-time and reduce the resulting trigger efficiency.

Transverse momenta Finally the efficiency is shown in Figure 3.4 w.r.t the minimal transverse momentum of the $\mu^+\mu^-$ tracks. The overall efficiency is flat with values around 88% and an expected drop for (very) low momentum values. The latter will curl inside the CDC and not reach the outermost superlayer, which is the requirement for the track to be triggered as "full" track.

3.3.1.3. Overall efficiency

As an overall efficiency for ffo w.r.t hie we get:

- 2019: $0.8920 \pm 0.0002 \pm 0.1740$
- 2020: $0.8606 \pm 0.0002 \pm 0.1799$

and for ffo30 w.r.t hie:

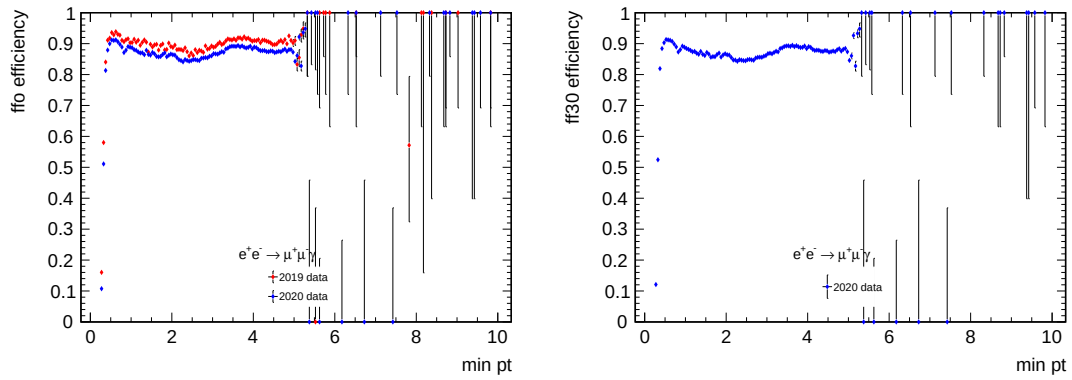

Figure 3.4.: ffo (left) and ff30 (right) efficiency w.r.t. minimal transverse momentum for selected $e^+e^- \to \mu^+\mu^-\gamma$ events

- 2020: $0.8599 \pm 0.0002 \pm 0.1772$

where the errors indicated are statistical and systematic respectively. Systematic effects are evaluated as the standard deviation in the plateau efficiency among different bins of the selected variables. The different contributions are given in Table 3.1 in case of ffo and Table 3.2 for ff30. Systematic effects due to the azimuthal angle dependence of the trigger efficiency are accounted for from the study of the variation in the trigger efficiency as function of the 2D opening angle (defined as the difference in the azimuthal angle of the two tracks $\Delta\phi$). The largest systematic effect is given by the polar angle dependency estimated as 9-10% for both ffo and ff30. These values are due to the efficiency drop near the border of the ECL barrel (see Figure 3.3). Dependencies on the track momentum of the tracks are found to systematically affect the efficiency at a level of 8%. All systematics contributions are summed in quadrature. These results will be further discussed in Section 3.5.

3.3.2. KLM

Both CDC trigger lines studied in the previous section are at risk of being prescaled. The high beam background levels will not only worsen their efficiency but also increase the corresponding trigger rate. Due to the limited bandwidth, only every Xth event (X being the prescale value, usually at the order of 10, 50 or 100) could thus be registered and further used in data analysis. It is therefore crucial to explore different approaches to trigger these events. I provide here an initial look at the performance of the KLM mu_b2b trigger bit which has been activated in the middle of 2020 data taking. It is in particular interesting for the 2-track muon events and it requires a similar logic to ffo and ff30. Due to the topology selected by the mu_b2b trigger bit (2 back-to-back tracks in BKLM sectors), we omit the photon from the reconstruction of the final state and apply further selection criteria to focus on $\mu^+\mu^-$ events reaching the BKLM and study it w.r.t ffo:

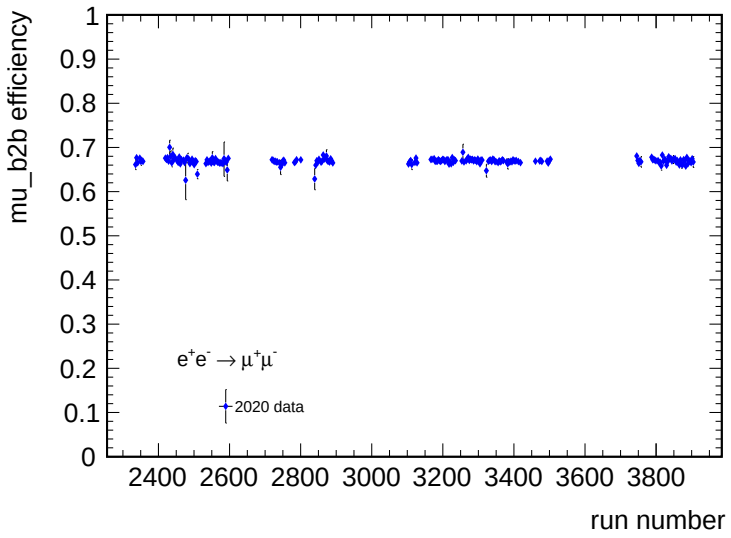

Figure 3.5.: mu_b2b efficiency w.r.t. run number for selected $e^+e^- \to \mu^+\mu^-$ events

- $p_T > 1\,\text{GeV}$ (0.7 GeV being the minimal value for muons to reach the BKLM)
- $-0.4 < \cos(\theta) < 0.62$ (require both tracks to be in BKLM)

3.3.2.1. Dependencies

Run number The run-by-run efficiency of mu_b2b shown in Figure 3.5 shows a constant performance at the level of 70% throughout the 2020 data taking. The visible gaps are due to some bad runs in which changes were made to the KLM subdetector configuration.

Azimuthal angle In Figure 3.6 the efficiency of mu_b2b is shown w.r.t the azimuthal angle of both tracks. The drops in efficiency appearing in equal distances correspond to the discontinuity regions in between the 8 BKLM sectors.

Polar angle The mu_b2b efficiency can be seen in Figure 3.7 w.r.t the polar angle of both tracks. For $\cos(\theta)$ values of 0.2-0.3, the efficiency drops to less than 10%. This should be due to the fact that the BKLM is split into two sections (forward and backward) and that tracks with concerned $\cos(\theta)$ values pass through both of them.

Transverse momentum Finally in Figure 3.8 the efficiency is shown w.r.t the minimum transverse momentum value of both tracks. The efficiency reaches its maximal value as expected for tracks sharing the beam energy equally (and maximum opening angle of 180°). The dip at momentum values of 3 GeV is not yet understood.

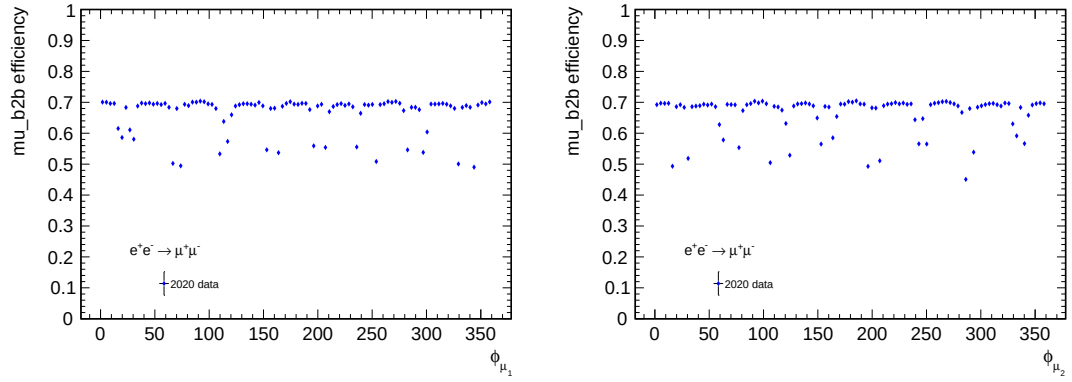

Figure 3.6.: mu_b2b efficiency w.r.t. ϕ_{μ_1} and ϕ_{μ_2} for selected $e^+e^- \to \mu^+\mu^-$ events

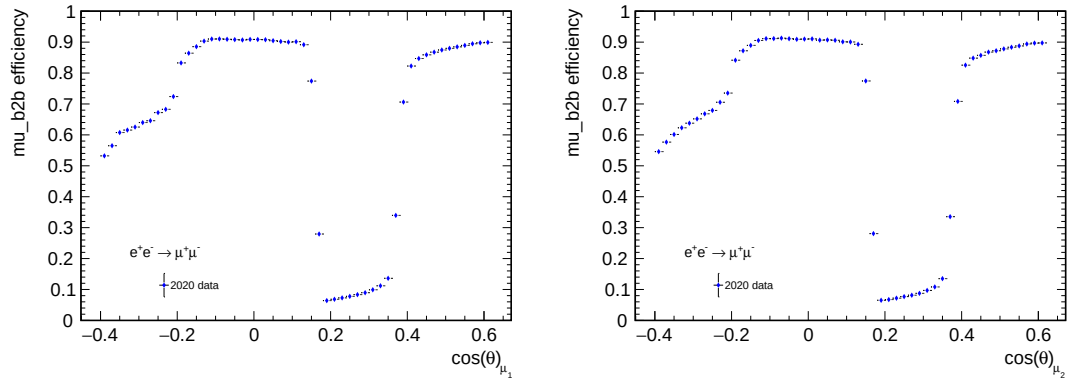

Figure 3.7.: mu_b2b efficiency w.r.t. $\cos(\theta_{\mu_1})$ and $\cos(\theta_{\mu_2})$ for selected $e^+e^- \to \mu^+\mu^-$ events

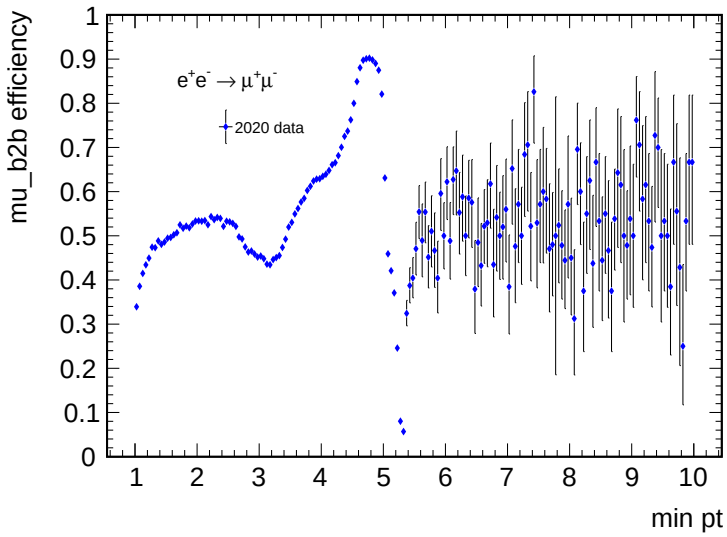

Figure 3.8.: mu_b2b efficiency w.r.t. minimum transverse momentum for selected $e^+e^- \to \mu^+\mu^-$ events

3.3.2.2. Overall efficiency

I compute the overall efficiency of mu_b2b w.r.t. ffo to be:

- 2020: 0.6693 ± 0.0002

where the indicated error is statistical. I do not provide an evaluation of the systematic contributions to the overall efficiency, as the dependencies of the trigger efficiency w.r.t. the different track parameters require further studies.
As an additional check I studied the impact on the muonID cut value on the overall efficiency value and provide the results below:

- 2020: 0.6810 ± 0.0002 (muonID> 0.9)
- 2020: 0.6825 ± 0.0002 (muonID> 0.95)

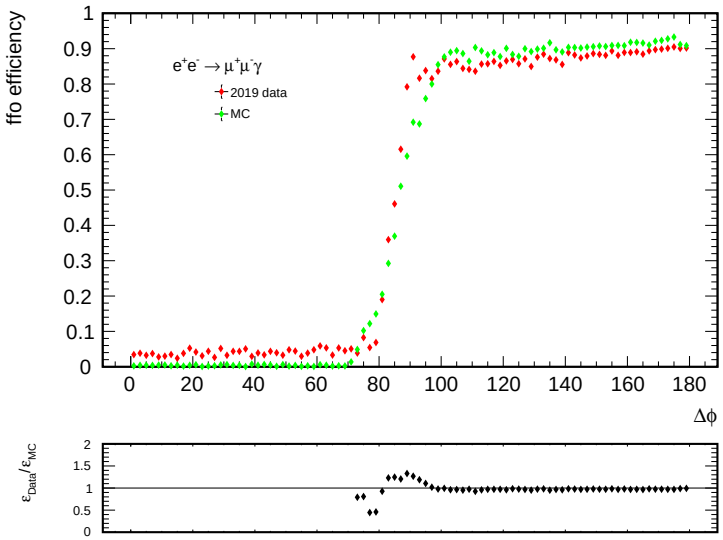

Figure 3.9.: Activation curve of ffo for selected $e^+e^- \to \mu^+\mu^-\gamma$ events in data and MC

3.4. TSIM

So far, the trigger performance has been studied with recorded data. As the efficiency values were computed to be less than 100% and multiple dependencies have been identified, one needs to account for these observations in physics analysis. In particular, one should be able to reproduce the trigger behaviour in MC samples: when computing expected sensitivities for example, a precise description of the detector becomes crucial. There are two different ways this can be achieved: one can either scale the MC samples according to the trigger efficiency value measured in data and assign the dependencies as systematic uncertainty or emulate the trigger behaviour during the generation of these samples. TSIM is the full simulation of the L1 hardware trigger at Belle II. It contains both the simulation of trigger algorithm and firmware. I want to evaluate its performance using the simulated data sets described in Section 3.2 and compare it to the results established in Section 3.3.1.

3.4.1. Activation curve

I start again by looking at the activation curve of the ffo trigger line w.r.t hie in Figure 3.9. Both curves are very close to each other and follow the same expected sigmoid-like shape. However, a few minor discrepancies can be spotted, as in MC the efficiency reaches an overall higher value after the activation at $\Delta\phi = 90°$ and goes all the way down to 0 before, which is not the case in data.

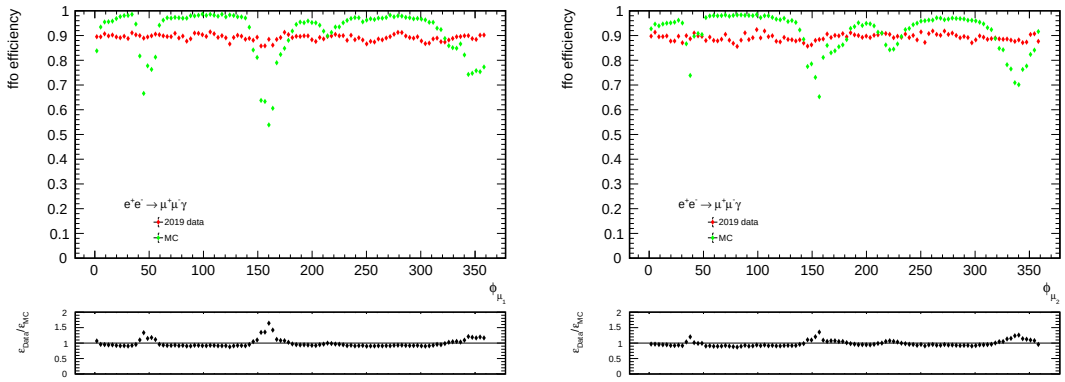

Figure 3.10.: ffo efficiency w.r.t ϕ_{μ_1} (left) and ϕ_{μ_2} (right) for selected $e^+e^- \to \mu^+\mu^-\gamma$ events in data and MC

3.4.2. Dependencies

The plateau efficiency ($\Delta\phi > 90°$) will be studied in bins of different kinematic variables and track parameters to understand how well the trigger behaviour is modelled in the simulation.

Azimuthal angle The plateau efficiency w.r.t the azimuthal angle of both tracks is shown in Figure 3.10. A major disagreement can be seen between data and MC which is mostly due to several large dips only present in the latter. Furthermore, the overall efficiency shows a discrepancy at the order of 5%. In fact these dips are caused by a not yet existing masking of CDC material in TSIM which will be implemented in the next software release.

Polar angle In Figure 3.11 the efficiency is shown w.r.t the polar angle of both tracks. We observe a similar behavior for data and MC with a near equal efficiency and dips at $\cos(\theta)$ values of -0.6 and 0.8. In data we see an additional dip at $\cos(\theta) = 0$ which is not present in MC. The possible reason causing this dip was already discussed in Section 3.3.1.2.

Transverse momentum Finally, the efficiency is shown w.r.t the minimal transverse momentum of the two muon tracks in Figure 3.12. Overall we observe a good agreement between data and MC with both curves showing similar features.

3.4.3. Overall efficiency

As an overall efficiency for ffo w.r.t hie in MC we compute:

- MC: $0.9127 \pm 0.0003 \pm 0.1912$

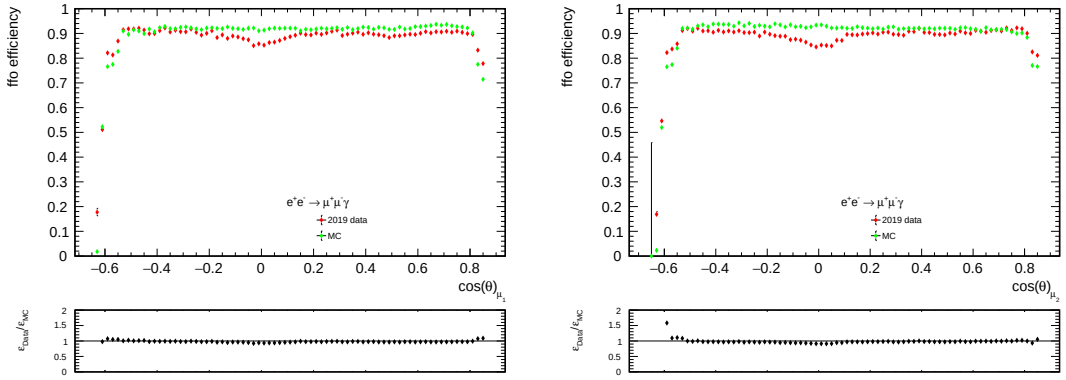

Figure 3.11.: ffo efficiency w.r.t $\cos(\theta_{\mu_1})$ (left) and $\cos(\theta_{\mu_2})$ (right) for selected $e^+e^- \rightarrow \mu^+\mu^-\gamma$ events in data and MC

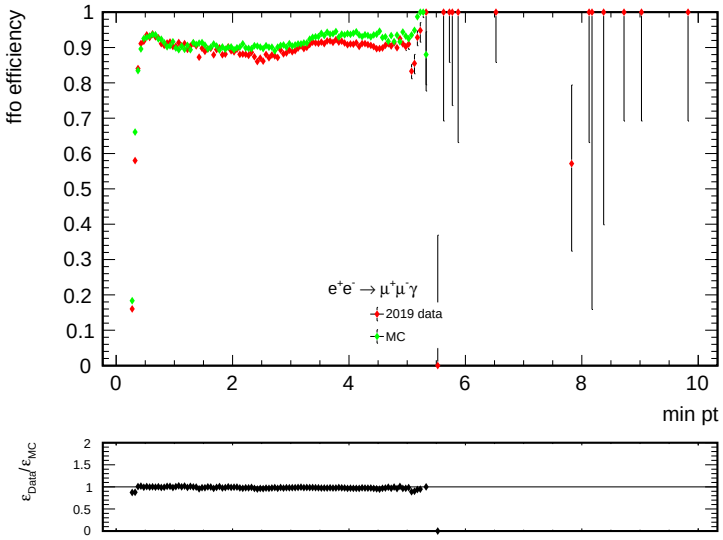

Figure 3.12.: ffo efficiency w.r.t minimal transverse momentum for selected $e^+e^- \rightarrow \mu^+\mu^-\gamma$ events in data and MC

where the errors indicated are statistical and systematic respectively. The latter has been computed w.r.t the same variables as was done in 3.3.1.3. As MC was simulated run-independently, there is no contribution to the overall systematic error by the run number and the resulting value may only be used for qualitative comparisons. In MC the ffo efficiency w.r.t hie is 2% higher than in data with a similar value for the systematic error. A detailed listing of the different contributions is given in Table 3.3. In conclusion, TSIM does not yet qualify for full usage in physics analysis. Several discrepancies and inconsistencies have been observed and the final efficiency value is different. Nevertheless, the algorithm is constantly maintained and future updates should fix the present bugs. Finally, it should be noted that instead of the run-independent MC samples used here, run-dependent samples are also produced by the Belle II collaboration. The "run-dependency" is related to the way these samples have been generated: every data taking run has been reproduced in simulation while taking into account the exact beam parameters and conditions of the Belle II detector of that same run. These samples should therefore offer a more accurate description of the run-by-run changes of experimental conditions and lead to comparable trigger results.

3.5. Dark Sector

In case of a dark sector analysis with low multiplicity final states, the trigger efficiency represents a major systematic contribution. It is therefore crucial to quantify the performance of the trigger line used in these kinds of analysis, as it is done here for the CDC trigger bit ffo. In addition, I want to study the impact of the different systematic contributions presented in the Section 3.3.1.3 while applying further selection criteria used in dark sector analysis such as the Higgsstrahlung measurement (see Section 4) and the Z' to invisible search (see Section 5).

In Section 3.3.1.2 a large drop in trigger efficiency w.r.t the polar angle of the two muon tracks was seen for values of $\cos(\theta)$ approaching the border of the ECL barrel. In order to avoid these regions of inefficiency I require the muon tracks to be contained in a reduced barrel region by selecting $-0.5 \leq \cos\theta_i \leq 0.8$ for every track candidate i and recompute the trigger efficiency in the 2019 data set. The results are shown in Table 3.4. The systematic contribution of the polar angle was reduced more than 80%.

Even though the "good" runs, as marked by the Belle II data production group, were used in this analysis, the ffo efficiency w.r.t the run number shown in Figure 3.2 highlighted a couple of "bad" runs with low efficiency. I want to exclude the affected runs by selecting only those with efficiency greater than 80% (later 85%). The results are given in Table 3.5.

Finally, I was not only able to reduce the systematic contribution of the run number by more than half but also increased the overall efficiency value for the ffo trigger bit.

The results are summarized in Table 3.6. While the overall systematic error is still evaluated to be 9%, the largest contribution arises from the minimum transverse momentum value to be 8%. This effect has been thoroughly studied and an additional cut on the transverse momentum of both tracks might decrease both this contribution and

consequently the overall systematic error value.

3.6. Additional tables

Source of systematics	Estimated effect in 2019 data	Estimated effect in 2020 data
Opening angle dependencies	0.0228	0.0218
Run number dependencies	0.0630	0.0486
$\theta_{LAB}(\mu^+)$ dependencies	0.0956	0.1040
$\theta_{LAB}(\mu^-)$ dependencies	0.0953	0.1058
Min p_T of the tracks	0.0869	0.0866
Total	**0.1740**	**0.1799**

Table 3.1.: Systematic contributions for ffo w.r.t hie in 2019 and 2020 data

Source of systematics	Estimated effect in Exp12
Opening angle dependencies	0.0171
Run number dependencies	0.0464
$\theta_{LAB}(\mu^+)$ dependencies	0.1029
$\theta_{LAB}(\mu^-)$ dependencies	0.1057
Min p_T of the tracks	0.0849
Total	**0.1772**

Table 3.2.: Systematic contributions for ffo30 w.r.t hie in 2020 data

Source of systematics	Estimated effect in MC
Opening angle dependencies	0.0517
Run number dependencies	0
$\theta_{LAB}(\mu^+)$ dependencies	0.1179
$\theta_{LAB}(\mu^-)$ dependencies	0.1171
Min p_T of the tracks	0.0793
Total	**0.1912**

Table 3.3.: Systematic contributions for ffo w.r.t hie in MC

Source of systematics	Estimated effect in $e^+e^- \to \mu^+\mu^-\gamma$
Opening angle dependencies	0.0232
Run number dependencies	0.0627
$\theta_{LAB}(\mu^+)$ dependencies	0.0164
$\theta_{LAB}(\mu^-)$ dependencies	0.0190
Min p_T of the tracks	0.0831
Total	**0.1095**

Table 3.4.: Systematic contributions in case of a requirement for the two muon tracks to be contained in a reduced ECL barrel.

Source of systematics	Estimated effect with $\epsilon_{\text{run}} \geq 80\%$	Estimated effect with $\epsilon_{\text{run}} \geq 85\%$
Opening angle dependencies	0.0223	0.0233
Run number dependencies	0.0355	0.0298
$\theta_{LAB}(\mu^+)$ dependencies	0.0164	0.0166
$\theta_{LAB}(\mu^-)$ dependencies	0.0179	0.0181
Min p_T of the tracks	0.0827	0.0819
Total	**0.0959**	**0.0934**

Table 3.5.: Systematic contributions in case of the requirement of a reduced barrel and selecting runs with efficiencies greater than or equal to 80% and 85%

Selection	Overall trigger efficiency
standard	$0.8920 \pm 0.0002 \pm 0.1740$
reduced barrel	$0.9001 \pm 0.0003 \pm 0.1095$
reduced barrel and $\epsilon_{\text{run}} > 80\%$	$0.9045 \pm 0.0003 \pm 0.0959$
reduced barrel and $\epsilon_{\text{run}} > 85\%$	$0.9083 \pm 0.0003 \pm 0.0934$

Table 3.6.: Overall ffo trigger efficiency including statistical and systematic contribution with different requirements on polar angle region and run number.

Part III.

Physics Analysis

4. Dark Higgsstrahlung

The following work was done in collaboration with two other PhD students Marcello Campajola [1] and Giacomo De Pietro [2]; guidance was provided by Gianluca Inguglia and Enrico Graziani [2]. The author provided major contributions to the results presented in Section 4.4.2, 4.5, 4.6 and 4.7.

4.1. Analysis overview

I present the measurement of the Dark Higgsstrahlung process, introduced in Section 1.2.1, which is carried out with data collected in 2019 at the Belle II experiment (see Section 2.2). In this work the search is limited to the case of a Dark Photon A' decaying into a pair of muons, and the Dark Higgs h' being lighter than the A', hence having a large lifetime and escaping detection, and therefore showing up as a missing energy signature. We thus perform this search in the range $2m_\mu < m_{A'} < 10.58\,\mathrm{GeV}/c^2$ with the additional constraint $m_{h'} < m_{A'}$.

The experimental signature is given by the presence, in events with two muons plus missing energy, of two peaks in the distribution of the dimuon mass and the invariant mass of the system recoiling against the two muons. Dimuon and recoil mass are kinematically related by:

$$M^2_{rec} = s + M^2_{\mu\mu} - 2\sqrt{s}E_{\mu\mu} \tag{4.1}$$

and experimentally by the fact that they are measured by the same pair of muons. Most of the results are presented in two-dimensional distributions as a function of both masses (see Figure 4.1), with the phase space having a triangular shape and being limited by $M_{rec} < M_{\mu\mu}$ on the left and $M_{rec} + M_{\mu\mu} < \sqrt{s}$ on the right.

Background events arise from SM processes that mimic the signal topology of two muons plus missing energy. The most dominant contribution come from $ee \to \mu\mu\gamma$, where one or more photons are lost due to inefficiency or acceptance, $ee \to \tau\tau$, with $\tau \to \mu$ or $\tau \to \pi$ (where a π is misidentified as a μ), $ee \to ee\mu\mu$, the two photon process with electrons and positrons outside of acceptance.

I start with the reconstruction of candidate events in Section 4.3, followed by the identification and application of appropriate selection criteria to reduce background contamination in Section 4.4. Events are then organized in two-dimensional mass windows with sizes of twice the mass resolution in both directions. Given that dimuon and recoil masses are correlated by the momentum measurement, tilted windows, with an angle of

[1]INFN, Sezione di Napoli, Napoli, Italy
[2]INFN, Sezione di Roma Tre, Roma, Italy

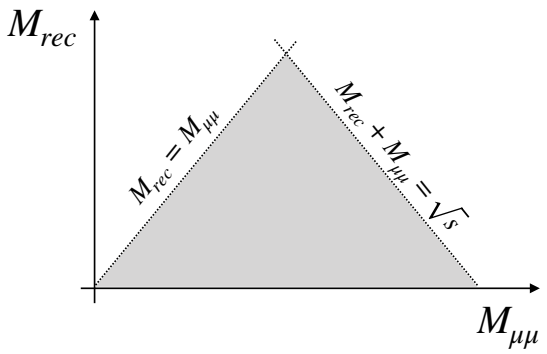

Figure 4.1.: Schematic of the triangular phase space in the two-dimensional distribution of the dimuon and recoil mass.

varying magnitude across the phase space, are used to maximize signal to background ratio (Section 4.4.2). Further improvement of the analysis sensitivity is achieved with a final background suppression, based solely on kinematic features (Section 4.4.3). Before "unblinding", i.e the ultimate measurement in the region of interest using data instead of Monte Carlo samples, we validate the analysis methods and estimate the background with an extensive use of control samples in Section 4.6, from which we infer correction factors and related systematic uncertainties (Section 4.7). We then compute 90% CL (confidence level) upper limits on the Dark Higgsstrahlung cross-section while counting number of observed events over expected background in two-dimensional mass windows (Section 4.8).

4.2. Data sets

The results presented in this work are based on the processed data which was collected in 2019 and amounts to an integrated luminosity of $\int \mathcal{L} dt = 8.339\,\mathrm{fb}^{-1}$.

For the signal simulation we use Monte Carlo (MC) samples produced with the MadGraph generator [37]. Different signal samples with and without initial state radiation (ISR) were produced, for specific use later on in the analysis (see Section 4.4.2 and 4.5).

We generated 9003 samples with 10000 events each, every sample corresponding to a distinct $M_{A'}$ and $M_{h'}$ mass hypothesis, with $M_{A'}$ ranging from the dimuon threshold up to $10.58\,\mathrm{GeV}/c^2$ and with $M_{h'} < M_{A'}$. Mass points are located on a two-dimensional grid with spacings corresponding to the mass resolutions in the two directions. The grid was carefully tuned (Section 4.4.2) in view of a scanning technique for a hypothetical signal search.

We use the MC samples listed in Table 4.1 for background studies.

Process	$\int \mathcal{L}dt$ [fb^{-1}]
$e^+e^- \to \mu^+\mu^-(\gamma)$	450
$e^+e^- \to \tau^+\tau^-(\gamma)$	1000
$e^+e^- \to e^+e^-\mu^+\mu^-$	100
$e^+e^- \to u\bar{u}$	100
$e^+e^- \to d\bar{d}$	100
$e^+e^- \to s\bar{s}$	100
$e^+e^- \to c\bar{c}$	100
$e^+e^- \to B^0\bar{B}^0$	100
$e^+e^- \to B^+B^-$	100
$e^+e^- \to \pi^+\pi^-(\gamma)$	65
$e^+e^- \to e^+e^-(\gamma)$	20
$e^+e^- \to e^+e^-e^+e^-$	300
$e^+e^- \to e^+e^-\pi^+\pi^-$	1000
$e^+e^- \to e^+e^-KK$	1000
$e^+e^- \to e^+e^-p\bar{p}$	1000
J/Ψ	164
$\Psi(2s)$	2500

Table 4.1.: List of MC samples used for background studies with the equivalent integrated luminosity $\int \mathcal{L}dt$.

4.3. Candidate reconstruction

We reconstruct candidate events by requiring two oppositely charged tracks emerging from a region close to the IP, satisfying the following criteria which we define as "cleaned tracks" (see Figure 2.2 for the coordinate system and note that $r = \sqrt{x^2 + y^2}$):

- $|dz| < 2\,\text{cm}$
- $|dr| < 0.5\,\text{cm}$
- the number of hits registered in the CDC per track shall be greater than 0, nCDCHits>0

The tracks are identified as muons by applying a selection on the muon identification probability [38], which is defined as

$$\text{muonID} = \frac{\mathcal{L}_\mu}{\mathcal{L}_e + \mathcal{L}_\mu + \mathcal{L}_\pi + \mathcal{L}_K + \mathcal{L}_p + \mathcal{L}_d} \tag{4.2}$$

where the individual likelihoods are computed using the information provided by all the sub-detectors, except for the SVD (At the time of writing the PDFs regarding dE/dx in SVD were not yet available for all the particle hypotheses.) We require muonID>0.5. The selected tracks are then combined to form a dimuon and therefore A' candidate and the event is accepted only if there are no more than 4 cleaned tracks.

Besides these candidate tracks we also reconstruct the rest of the event (ROE). As the ROE includes every track and cluster not associated to the signal dimuon pair, we need to clean it up from beam-induced energy depositions by applying a so-called ROE mask. The latter is a container of tracks and clusters which pass a set of given selection criteria. Regarding the clusters in the ROE we require:

- the polar angle should be contained in the angular acceptance of the CDC, $17° < \theta < 150°$;
- the cluster's timing uncertainty should be small as large values are an indication of a failed waveform fit, clusterErrorTiming $< 1 \times 10^6$ ns;
- a threshold on either the ratio of energies of the central crystal E1, and 3×3 crystals E9 around the central crystal clusterE1E9 > 0.4; or on the total energy of the cluster, E > 0.1 GeV

Furthermore, tracks in the ROE must have at least one hit in the CDC (nCDCHits>0). Finally, the recoil system against the dimuon candidate with respect to the centre of mass (CM) momentum is reconstructed, being the h' candidate for that event.

4.4. Event selection

4.4.1. Preselections

The suppression of background contamination is being achieved by applying a number of tighter selections, denoted as preselections in the following. Every candidate has to satisfy:

1. the number of cleaned tracks must be exactly 2 and the opening angle between the two muon tracks should exceed 90°, in order to emulate the functionality of the CDC trigger described in Section 3.3;
2. the polar angle of the muon tracks must be within a restricted ECL barrel region for a good cluster-matching efficiency and for a good control of the systematics ($37° < \theta_\mu < 120°$), see Section 3.5;
3. the recoil momentum must point to the ECL barrel acceptance region ($33° < \theta_{\text{recoil}} < 128°$), to exclude inefficient regions where photons can pass undetected and mimic the signal recoil;
4. we reject events where the closest reconstructed photon lies within a 15° cone from the recoil momentum;
5. no additional tracks are allowed in the ROE and the extra energy in the ECL is required to be less than 0.4 GeV;
6. the transverse momentum of the dimuon candidate in the CMS frame $p^T_{\mu\mu}$ should be greater than 0.1 GeV/c;

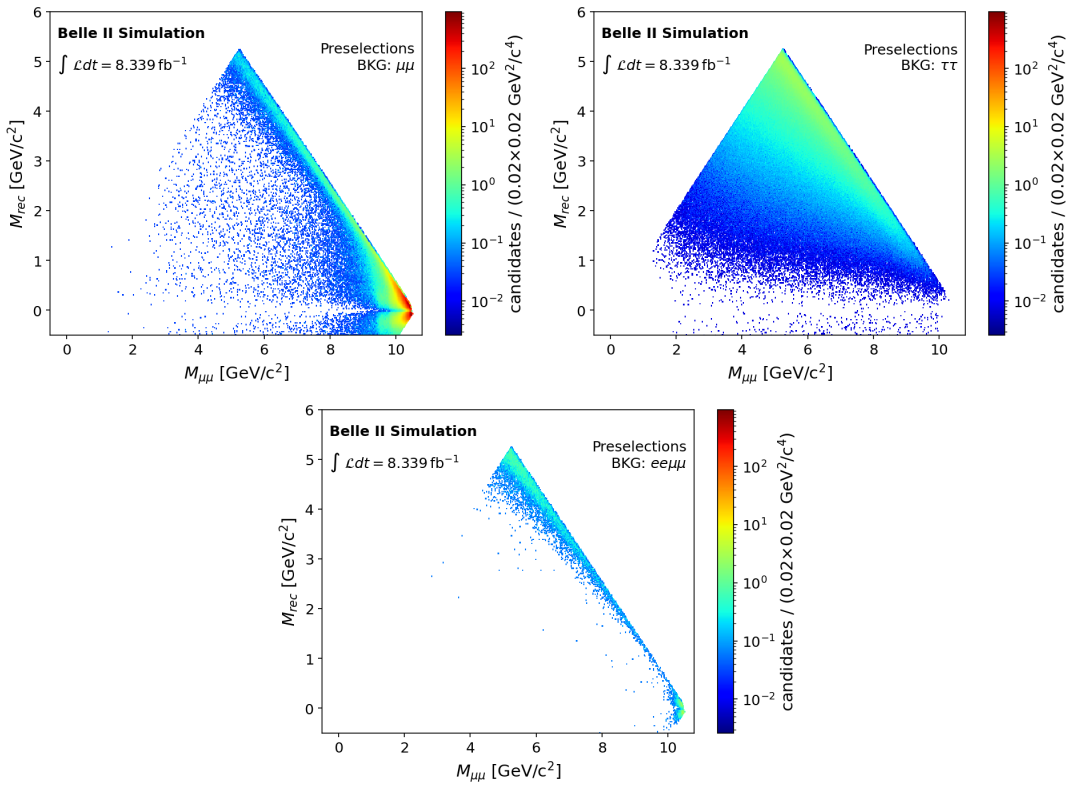

Figure 4.2.: Mass distributions of the three main background sources after the preselections, normalized to an integrated luminosity of $8.339\,\mathrm{fb}^{-1}$. Top left: $e^+e^- \to \mu^+\mu^-(\gamma)$; top right: $e^+e^- \to \tau^+\tau^-(\gamma)$; bottom: $e^+e^- \to e^+e^-\mu^+\mu^-$.

7. we setup a special veto to suppress the contribution of cosmic radiation, where reconstructed tracks were split into two artificially: events with the ratio of the two muon momenta in the LAB frame $0.98 < p_0/p_1 < 1.02$ and with the opening angle (LAB frame) in the transverse plane $\Delta\phi > 179.7°$ were rejected;

8. In case of the $\mu\mu\gamma$ process, final state radiation (FSR) can lead to an unresolved photon very close to one of the two muons, and therefore a large energy deposit in the ECL associated to the same muon, we suppress this background contribution by requiring the ECL cluster energy of the muons to be smaller than 1.5 GeV;

9. the recoil and dimuon masses are required to satisfy the constraint $M_{\mu\mu} - \sqrt{s} < M_{rec} < \sqrt{s} - M_{\mu\mu}$. Moreover, the recoil mass was required to be always larger than $-1\,\mathrm{GeV}/c^2$. Regions outside these constraints were only populated by background (see Section 4.4.4).

The distributions of the three main background sources after theses preselections are shown in Figure 4.2. They populate different regions of the available phase space.

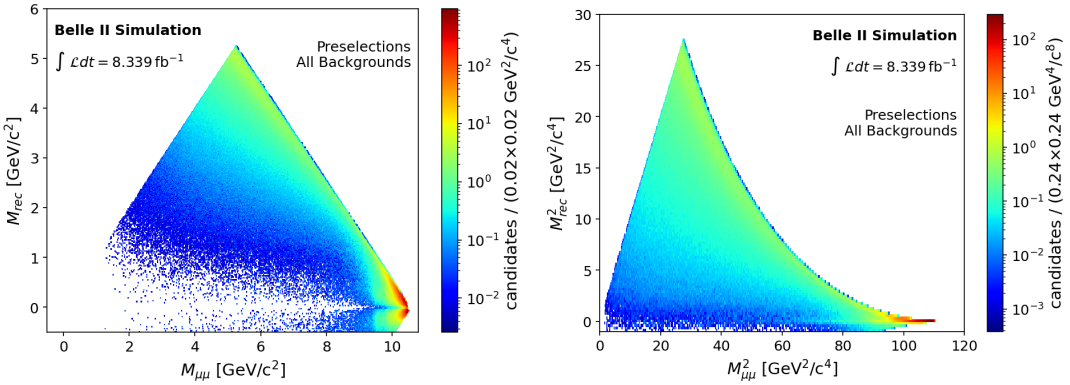

Figure 4.3.: Mass distributions (left) and squared mass distribution (right) of the total background after the preselections, normalized to an integrated luminosity of $8.339\,\mathrm{fb}^{-1}$.

One would naively expect events emerging from the $\mu\mu(\gamma)$ background source to populate the bottom region of the phase space, with recoil masses close to zero due to the presence of the ISR photon. However, the preselections defined above require no observed photons and the recoil momentum pointing to the (efficient) ECL barrel region. This condition cannot be met by a hard (high energy) ISR photon. In case of two ISR photons produced in opposite directions along the beam axis, they could go out of the detector acceptance and their total momentum would be pointing to the barrel region. This would lead to a high diphoton invariant mass and thus a high recoil mass. With these arguments we are able to understand why most of the events from $\mu\mu(\gamma)$ accumulate towards the right edge of the phase space triangle. The same mechanism holds for the $J/\psi\gamma(\gamma)$ and $\psi(2S)\gamma(\gamma)$ background, where most of the events accumulate outside the triangle, at high recoil masses. Another way for photons of $\mu\mu(\gamma)$ to go undetected is via the already mentioned FSR process in selection 8: Photons are emitted at very low angles with respect to the muon and lead to high energy cluster which is then associated with the muon. These events tend to populate the lower left region of the phase space triangle at low recoil masses, corresponding to the mass of the FSR photon.

The total background, normalized to the luminosity can be seen in Figure 4.3. A region of low signal efficiency can be seen for $M_{\mu\mu}$ below $4\,\mathrm{GeV}/c^2$. This is due to the ffo trigger which requires the opening angle of the two tracks to be greater than 90°. This inefficiency may be recovered with the usage of either the ff30 trigger line or KLM trigger bit introduced both in Section 3.1. These trigger lines were however not active during the 2019 data taking and may only be used at a later repetition of the measurement.

4.4.2. Mass windows

For the final signal extraction we define mass windows in which we count the number of observed events. We opted to use the squared masses, as this allows for a more direct

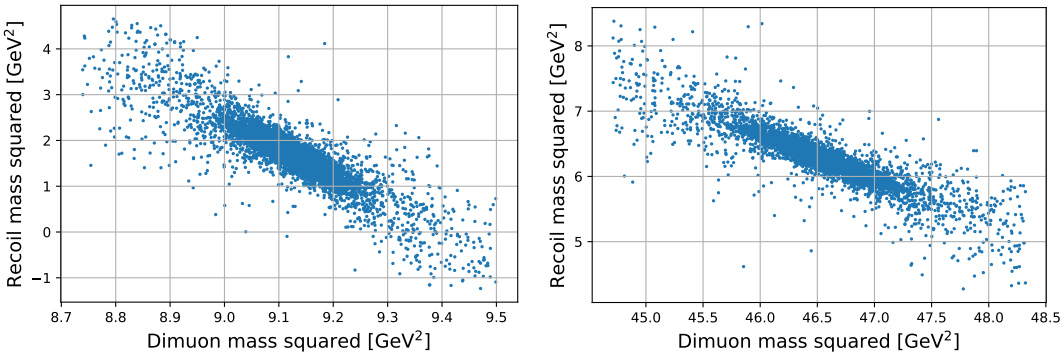

Figure 4.4.: Two examples of the correlation between the dimuon and recoil mass squared.

physics interpretation in the 2D mass plane. As expected from kinematic considerations and Equation 4.1, the dimuon and recoil mass squared are correlated. Two examples are shown in Figure 4.4. Whereas the correlation is observed to be always negative, its amount is varying across the mass plane. We therefore set up a decorrelation procedure. For each generated $A'h'$ pair, the linear slope is computed in the squared mass plane using the inertia momentum algorithm from rigid body classical mechanics. The magnitude of the resulting angle is shown in Figure 4.5 for every generated pair. We do not take into account the contribution from ISR for the generated pairs, as this introduces a tail in the recoil mass distribution (vertical direction) and would impact the accuracy of the fits. A successful cross-check was performed in order to see if the computed slopes of the samples without ISR reproduce those of the samples with ISR. We then perform local rotations for every generated $A'h'$ pair according to the compute slope and defined two new masses, $M^{2\prime}_{\mu\mu}$ and $M^{2\prime}_{rec}$, the projections on the new axes. The distributions of $M^{2\prime}_{\mu\mu}$ and $M^{2\prime}_{rec}$ are then fitted separately as 1D distributions for each generated $A'h'$ pair (see Section 4.5).

Mass windows are now defined as ellipses centred at the nominal mass values with semi-axes equal to multiples of the widths of the $M^{2\prime}_{\mu\mu}$ and $M^{2\prime}_{rec}$ distributions. For the majority of the mass plane, optimal values turned out to be widths of 2σ, while in regions delimited by $M_{\mu\mu} + M_{rec} > 9.5\,\text{GeV}/c^2$ or $M_{\mu\mu} > 8\,\text{GeV}/c^2$ the window size was reduced to 1.5σ (see Section 4.4.4). The number of observed events will then be counted in a total of 9003 elliptical squared mass windows, tilted according to the angle Figure 4.5. The distance in between the centres of the different ellipses corresponds to approximately the squared mass resolution. A schematic illustrating the mass windows is shown in Figure 4.6. The usage of tilted ellipses w.r.t to straight (unrotated) mass windows in the $M^2_{\mu\mu}$ and M^2_{rec} plane reduces the amount of background contribution by a factor of 3 to 5 depending on the mass point. 4.7

An additional set of enlarged mass windows was also defined for later usage in Section 4.4.3 and 4.6. They are identical to the previously defined ellipses in the $M^{2\prime}_{\mu\mu}$ and $M^{2\prime}_{rec}$ plane with the only difference being larger semi-axes with values of 6σ, thus covering a surface 9 times larger.

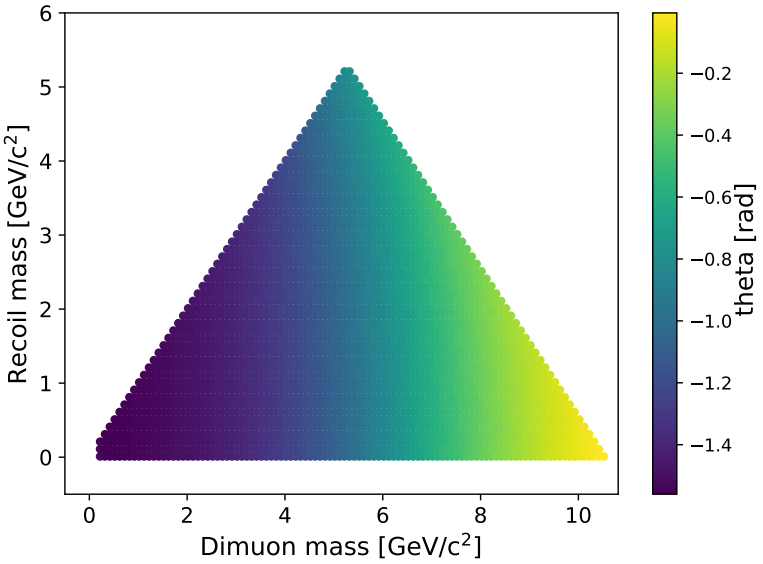

Figure 4.5.: Fitted correlation angles as a function of the dimuon and recoil mass.

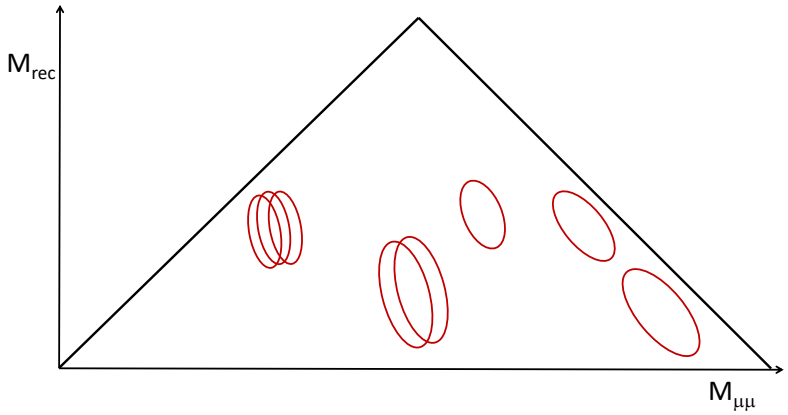

Figure 4.6.: Mass windows as they appear in the $M_{\mu\mu} - M_{rec}$ plane (not to scale).

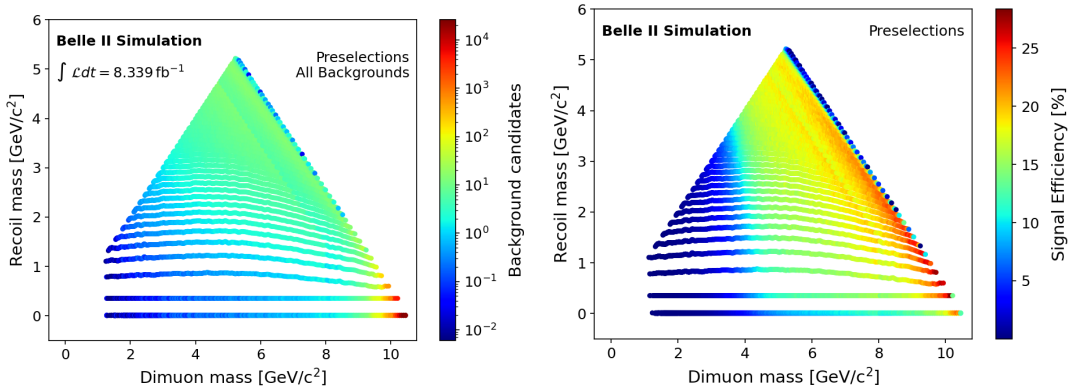

Figure 4.7.: Left: Mass distributions of the total background inside mass windows after the preselections, normalized to an integrated luminosity of $8.339\,\mathrm{fb}^{-1}$. Right: signal efficiency inside the mass windows after the preselections, as a function of the dimuon and recoil mass. In both cases the effect of reducing the mass window sizes in the regions close to the kinematical border is clearly visible.

4.4.3. Final background suppression

The remaining background contamination is being suppressed with a dedicated procedure, based solely on kinematic features of the selected events. We make use of the so-called helicity angle θ_{hel}, defined as the angle between the flight direction of the A' and the μ^- in the A' rest frame. The distribution of θ_{hel} is entirely determined by the general properties of a massive vector resonance decaying into two fermion particles. For an unpolarized A' the distribution of $\cos(\theta_{hel})$ is expected to be flat, a feature implied by the presence of the three polarization states (two transverse plus one longitudinal, as opposed to the case of the ordinary photon, where only the transverse degrees of freedom exist) , due to the massive nature of the particle. This is not the case for the background, where the helicity angle θ_{hel} can be defined as well, but with no direct physical meaning, as the muons do not originate from a common resonance, coming either from different and independent decays ($\tau\tau(\gamma)$) or from different physics processes ($\mu\mu(\gamma)$ and $ee\mu\mu$). We define our discriminating variable as

$$A_E = |cos(\theta_{hel})| \tag{4.3}$$

It can be shown that in the muon massless approximation, the following relation holds

$$A_E = \left| \frac{E_{\mu_0} - E_{\mu_1}}{(E_{\mu_0} - E_{\mu_1})^2 - M_{\mu\mu}^2} \right| \tag{4.4}$$

Example distributions of A_E for different combinations of $M_{A'}$ and $M_{h'}$ are shown in Figure 4.8. The discriminating power is observed to be overall high with background events taking values around 1 and signal events following a flat distribution. In order

to better understand why background events populate near 1 in the A_E distribution, we explore an alternative interpretation of the helicity angle variable. As already mentioned before, the dimuon and recoil mass are related by Equation 4.1, which may be rewritten as:

$$E_{\mu_0} + E_{\mu_1} = \frac{s + M_{\mu\mu}^2 - M_{rec}^2}{2\sqrt{s}} = E_0 \tag{4.5}$$

The quantity E_0 remains constant for both signal and background events within the mass windows which arises from the requirement of the squared recoil and dimuon mass to be within $\pm 2\sigma$ intervals (and in case of signal events from the on-shell condition). The relation $E_{\mu_0} + E_{\mu_1} = E_0$ defines a straight line in the E_{μ_0} vs. E_{μ_1} plane. A few example distributions are shown on the left in Figure 4.8 for different mass combinations. Events populate a segment of variable length along the line, which depends on the minimum and maximum value that E_{μ_0} and E_{μ_1} can assume.

The muon energy asymmetry, quantified by A_E, can be understood as a consequence of the different production mechanisms. Regarding the dominant background process $\tau\tau(\gamma)$, muons originate from two independent decays of τ leptons with characteristic momentum distributions. Only a certain amount of these momentum combinations will make it into a specific mass window given the kinematic restrictions imposed by the fixed dimuon and recoil mass. This does however not hold for signal events, resulting in a flat A_E distribution.

For every mass window we apply $A_E < A_E^{cut}$, where A_E^{cut} is the result of an optimization procedure. Enlarged mass windows were used for this purpose. This reduces the impact of statistical fluctuations and leads to smooth results across the mass plane. A Punzi Figure of Merit (FOM) [39], which is given by:

$$\mathrm{FOM}_{\mathrm{Punzi}} = \frac{\epsilon_{sig}}{a/2 + \sqrt{N_{bkg}}} \tag{4.6}$$

with the signal efficiency ϵ_{sig}, number of surviving background events N_{bkg} and the desired CL (in terms of number of sigmas a corresponding to one-sided Gaussian test at the given CL, $a = 1.6$ for CL=90%) was set up for every enlarged mass window and maximized as a function of A_E. The results are shown in Figure 4.9.

We obtain smooth values for A_E^{cut} across the plane, the only exception being a band located at the extreme right of the phase space, which is caused by the fact that A_E distributions show a significant overlap when the sum of dimuon and recoil mass approaches $\sqrt{s}$. The background and signal efficiencies are then computed after applying the previously obtained value for A_E^{cut}, see Figure 4.10 and 4.11.

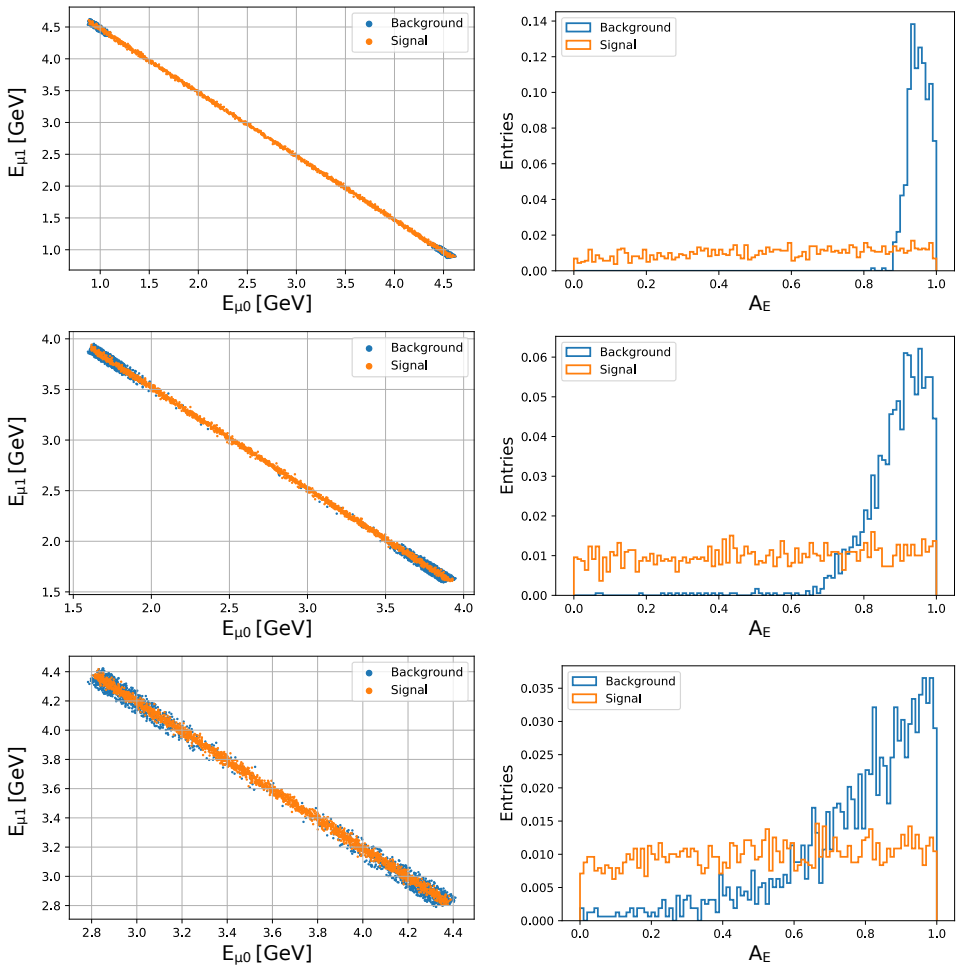

Figure 4.8.: E_{μ_0} vs E_{μ_1} relation (left) and A_E distribution (right) for three different mass combinations: $M_{A'} = 4.02\,\mathrm{GeV}/c^2$ and $M_{h'} = 3.51\,\mathrm{GeV}/c^2$ (top), $M_{A'} = 5.02\,\mathrm{GeV}/c^2$ and $M_{h'} = 4.51\,\mathrm{GeV}/c^2$ (centre), $M_{A'} = 7.02\,\mathrm{GeV}/c^2$ and $M_{h'} = 3.01\,\mathrm{GeV}/c^2$ (bottom).

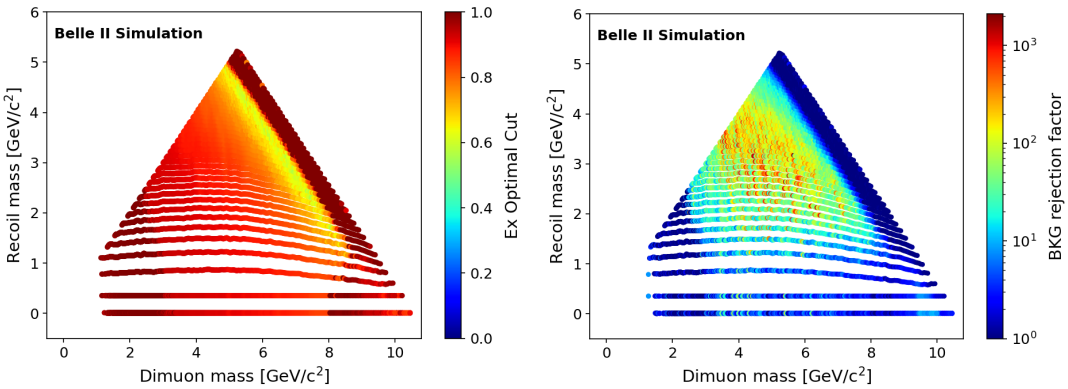

Figure 4.9.: The optimal A_E cut value in every mass window, resulting from the Punzi FOM procedure (left), background rejection factor when the A_E selection is applied (right)

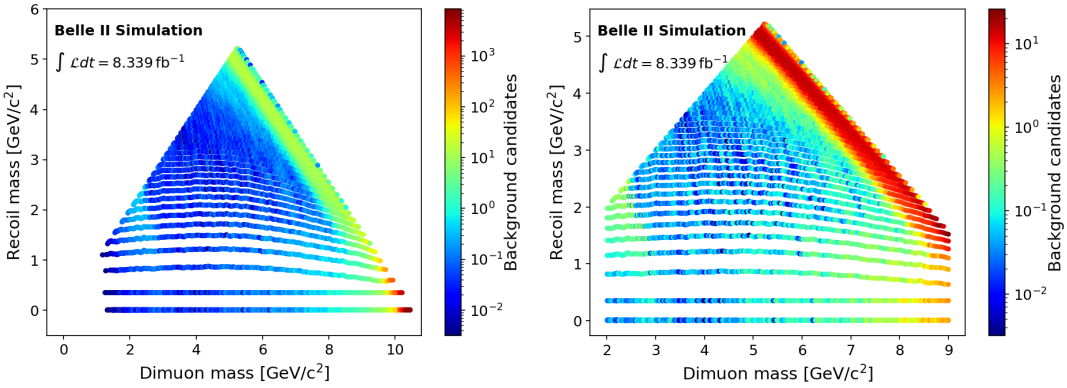

Figure 4.10.: The mass distributions of the total background inside the mass windows after the A_E selection, normalized to an integrated luminosity of $8.339\,\mathrm{fb}^{-1}$ (left), same distribution in a reduced dimuon mass interval in which the highest background region is not shown (right)

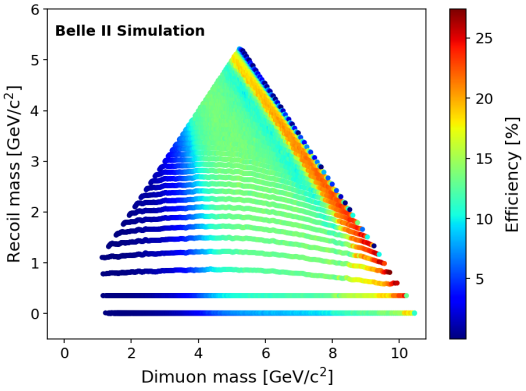

Figure 4.11.: The signal efficiency inside the mass windows after the A_E selection

4.4.4. Selection optimization

Some of the selection criteria presented in SECT. 4.4.1 are indeed the result of several optimization procedures, which have been performed after applying the suppression variable A_E at the end of the analysis chain. This concerns most notably the muonID, dimuon transverse momentum, extra energy and the mass window width. The studies presented here are performed while building Punzi FOM for each of these variables as a function of dimuon and recoil mass and comparing them to the FOM results obtained with the values in Section 4.4.1 , and finally by taking the ratios: a ratio of FOM larger than 1 indicates that the revised selection is performing better, i.e. leading to a higher sensitivity.

Two additional cut values have been investigated for the muonID selection, namely muonID>0.9 and muonID>0.95. The results showed that the average Punzi FOM value was slightly higher for the reference selection of muonID>0.5. This can be understood by looking at the pion contamination level (mostly coming from $\tau \to \pi$), which only slowly decreases with the muonID cut value: 16.1%, 13.7%, 13.1% for muonID cuts of 0.5, 0.9, 0.95, respectively. There are two different reasons causing this effect: 1) two out of three background sources produce real muons and 2) a non-negligible fraction of the pion contamination level in τ decays arises from low momentum pions, where the muonID is not driven by the KLM. It is thus the signal efficiency, decreasing with the muonID cut value, that is ruling the sensitivity rather than the background level. We therefore keep the muonID>0.5 selection.

Regarding the dimuon transverse momentum $p^T_{\mu\mu}$, the distributions for both signal and background were found to be very similar after the preselections, with minimum values starting at approximately 2 GeV/c. The initial cut value above 0.5 GeV/c would therefore have a purely cosmetic effect. The only exception to this pattern is the region close to the kinematical limit, on the right edge of the mass triangle. In this area of the phase space, the Dark Photon and the Dark Higgs (dimuon pairs and recoil system for the background) are produced at rest, which is equivalent to the muons being back-to-back

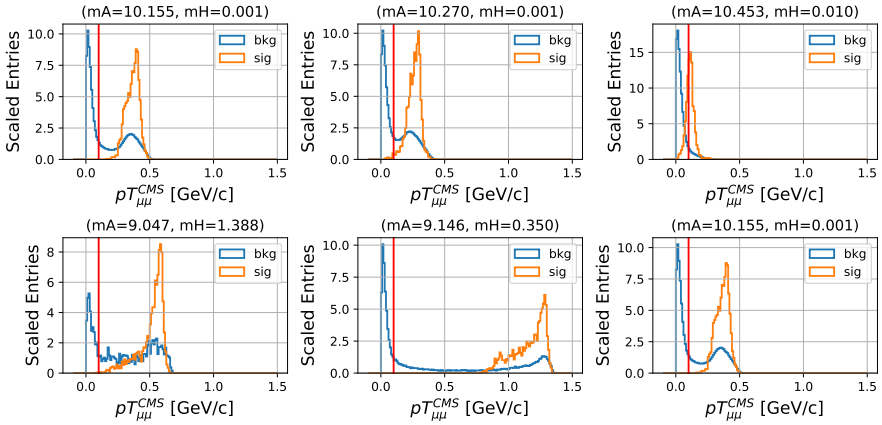

Figure 4.12.: Signal and background distribution of $p^T_{\mu\mu}$ for mass windows close to the kinematical limit $M_{\mu\mu} = \sqrt{s}$. The vertical red line indicates the cut value at $p^T_{\mu\mu} = 0.1\,\text{GeV}/c$.

and $p^T_{\mu\mu} \simeq 0$ in consequence. The resulting $p^T_{\mu\mu}$ distributions are shown in Figure 4.12 and can be understood with the following arguments. The most dominant background contribution is given by the $\mu\mu(\gamma)$ process: the peak at $p^T_{\mu\mu} \simeq 0$ corresponds to the events in which an ISR photon is emitted at low polar angles and carrying away no transverse momentum, in opposite to the second peak where the photon produced at a larger angle has similar kinematics to the Dark Higgs, so that both peaks coincide. We therefore aim to reject the collinear $\mu\mu(\gamma)$ background while simultaneously preserving the signal efficiency, which can all be achieved with $p^T_{\mu\mu} > 0.1\,\text{GeV}/c$. This is indicated in Figure 4.12 with are red line and was applied throughout the entire mass plane.

We investigated a possible further reduction of the ECL extra energy cut with reference value 0.4 GeV. The distributions of extraE for signal and background are shown in Figure 4.13, where different features can be noted: the $ee\mu\mu$ background was generated without ISR contribution, so that this distribution is not representative; the discontinuity at 0.1 GeV is due to the initial selection of the photon energy of $E_\gamma > 0.1\,\text{GeV}$ (see Section 4.4.1); entries in between 0 and 0.1 GeV correspond to particles not meeting the cleaned tracks criteria (see Section 4.3) and associated with an ECL cluster. The peak at 0.2 GeV in the $\mu\mu(\gamma)$ contribution is related to the presence of two photons with minimum energy of $E_\gamma = 0.1\,\text{GeV}$ which have been produced according to the mechanism already introduced in Section 4.4.1. In order to suppress this background source of two radiated photons, we studied the impact of requiring extraE$<$0.18 GeV in the region preferentially populated by $\mu\mu(\gamma)$ (see top left of Figure 4.2). As the gain in sensitivity turned out to be negligible, we stick to the reference value of 0.4 GeV.

The region of high background in the lower right of the phase space (see Figure 4.3), dominated by the $\mu\mu(\gamma)$ contribution, was closely inspected. Figure 4.14 shows the total background (left) and a detail of the signals at various masses in the region around

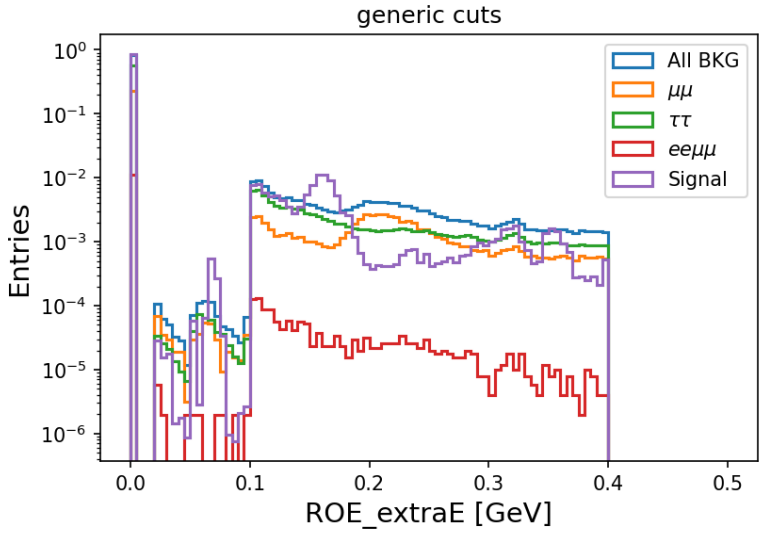

Figure 4.13.: The extra energy distribution for the signal and the different background sources

$M_{\mu\mu} = \sqrt{s}$ (right). To avoid confusion due to overlaps, only a set of signals generated on a downsampled grid and their corresponding mass windows are shown. Black lines indicate the border of the region accepted by the selection in point 9 of Section 4.4.1. It can be seen that signals are almost entirely included, but a consistent part of the background is rejected. Part of the validation procedures described in Section 4.6 are not based on event counting inside mass windows and benefit of this selection.

Different options for the mass window size, in particular 1, 1.5, 2.5 and 3.5σ have been explored and evaluated w.r.t the reference size of 2σ. As before, Punzi FOM ratios are computed in every case. Whereas sizes of 2σ and 2.5σ lead to very similar sensitivities, the options of 1σ and 3σ are not competitive. In regions identified by the condition $M_{\mu\mu} + M_{rec} > 9.5\,\text{GeV}/c^2$ or $M_{\mu\mu} > 8\,\text{GeV}/c^2$, which in general contain a high background level, mass windows of smaller size give better sensitivity with the optimal being 1.5σ, so that we choose to adopt it there.

4.5. Signal resolution studies

In order to estimate the width of the $M^{2\prime}_{\mu\mu}$ and $M^{2\prime}_{rec}$ distributions (see Section 4.4.2), we perform an unbinned maximum likelihood fit (using RooFit v3.6 [40]) of their one-dimensional projections for each generated $A'h'$ pair with no ISR contribution. We use the sum of two Gaussian functions to describe both the dimuon and recoil squared mass distributions. The resulting PDF consists of three parameters, as we fix the mean of both Gaussians to either the A' or h' squared mass value: $\sigma_{\text{Gauss},1}$ and $\sigma_{\text{Gauss},2}$, being the width of the first and second Gaussian respectively; and *frac*, the fraction of each

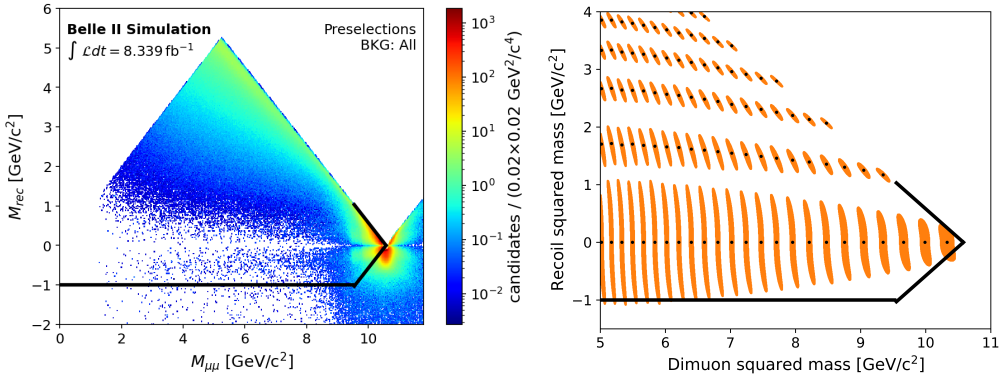

Figure 4.14.: Left: Total background contribution after preselections 1-8. Right: Signals on a downsampled mass window grid in a restricted mass region. Black lines indicate the border of the region accepted by the cut in point 9 of the preselections (see Section 4.4.1).

function with respect to the normalized sum of both. The rotated dimuon and recoil squared mass distribution for a given mass point as well as the corresponding fitted PDF model distribution can be seen in Figure 4.15.

We need to calculate the width of every rotated dimuon and recoil squared mass distribution while taking into account the different contributions of the two Gaussians. In order to do that we use Equation 4.7 with the fit results. The resulting weighted widths for every generated A' and h' mass point are shown in Figure 4.16.

$$\sigma_w = \sqrt{frac \times \sigma^2_{\text{Gauss},1} + (1 - frac) \times \sigma^2_{\text{Gauss},2}} \tag{4.7}$$

In addition we check the impact of the decorrelation procedure described in Section 4.4.2 by repeating the fit on the dimuon and recoil mass distributions $M^2_{\mu\mu}$ and M^2_{rec} before applying the local rotations. We compute the area of the mass windows before and after the rotation by multiplying dimuon and recoil weighted widths for every h' mass point associated to a fixed A' mass point. The resulting graph can be seen in Figure 4.17.

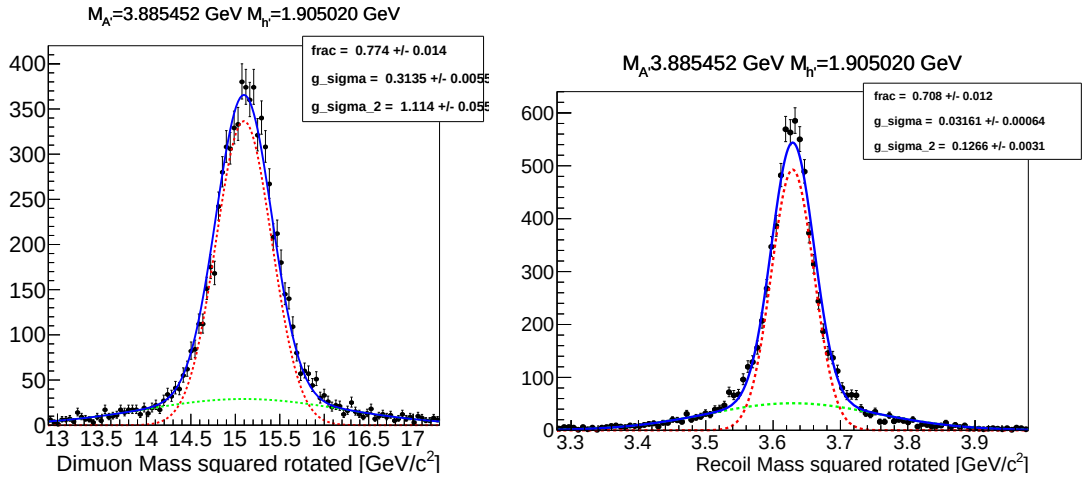

Figure 4.15.: Rotated dimuon (left) and recoil (right) squared mass distributions for $M_{A'} = 3.885\,452\,\mathrm{GeV}/c^2$ and $M_{h'} = 1.905\,020\,\mathrm{GeV}/c^2$ with the fitted PDF model overlayed (blue). The contribution of the two Gaussian functions are shown with a red and green dotted line respectively. The resulting fit parameters are shown in the top right corner of every graph.

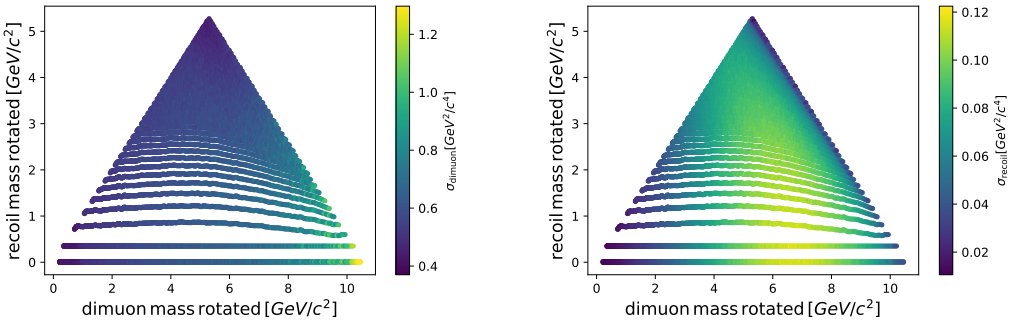

Figure 4.16.: Weighted widths for the rotated dimuon (left) and recoil (right) squared mass distribution of every generated A' and h' mass point.

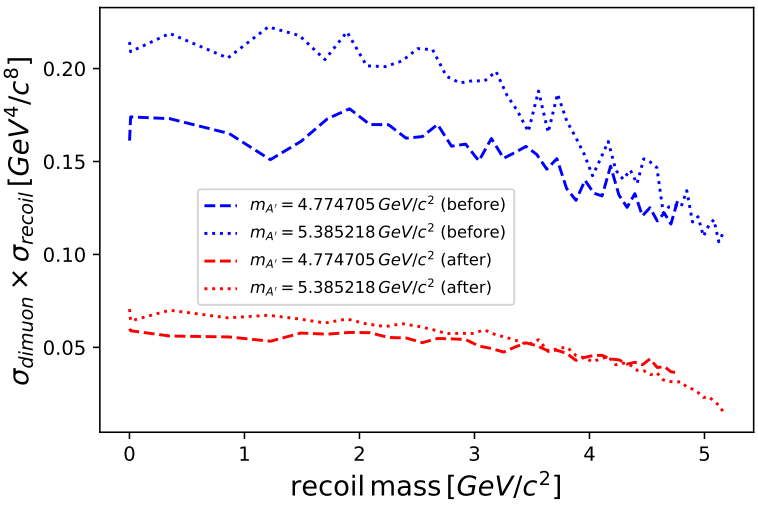

Figure 4.17.: Area of the mass window before (blue) and after (red) local rotation for every h' mass point associated to $M_{A'} = 4.774\,705\,\mathrm{GeV}/c^2$ and $M_{A'} = 5.385\,218\,\mathrm{GeV}/c^2$.

4.6. Data validation

The selection procedures that have been presented so far are now being validated with the usage of control samples. This is the first time we look at data events in addition to the MC samples (see Table 4.1) used up until now. In order to avoid an accidental unblinding, we need to select a different topology than the one introduced in Section 4.4.1, but with similar kinematic properties.

- $e^+e^- \to \mu^+\mu^-\gamma$ ($\mu\mu\gamma$ control sample): This topology is selected with slightly modified requirements than the one introduced in Section 4.4.1. We require the presence of a photon in the ECL barrel region with an energy of $E_\gamma > 1\,\mathrm{GeV}$. The requirement 4, regarding the rejection of photons within a 15° cone is being dropped. As what concerns requirement 5 and the cut on the extra energy in the ECL, we change it to be $extraE - E_\gamma < 0.4\,\mathrm{GeV}$. The resulting sample is dominated by contributions from the $\mu\mu(\gamma)$ MC sample. Only minor contributions are given by the $\tau\tau(\gamma)$ MC sample, where both τ leptons decay to muons and partly to pions with $\pi \to \mu$ misidentification. The $ee\mu\mu$ sample may be neglected for this control sample, as its contribution is underestimated given the missing ISR in the generation. The two-dimensional distribution of the expected background for this control sample is shown in Figure 4.18.

- $e^+e^- \to e\mu$ ($e\mu$ control sample): We apply the same selections as in Section 4.4.1 with one exception regarding the particle identification criteria: one track should be identified as an electron candidate with $electronID > 0.5$. The largest contribution to the resulting sample arises from the $\tau\tau(\gamma)$ MC sample with one τ decaying into

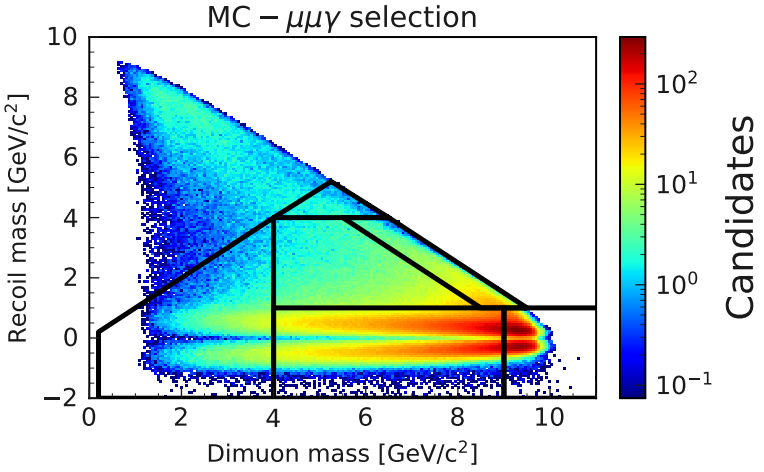

Figure 4.18.: 2d background distribution for the $\mu\mu\gamma$ control sample. Overlaid black lines show the macro regions.

an electron and the other into a muon (or pion, with misidentification). Other contributions involving particle misidentification include the Bhabha, $\mu\mu(\gamma)$, $ee\mu\mu$ and $eeee$ samples. The resulting two-dimensional background distribution is shown in Figure 4.19.

As opposed to these two control samples, there is the sample that is being used for the Dark Higgsstrahlung measurement, the "$\mu\mu$ measurement sample". The validation procedure is now performed by comparing the number of events in data and MC in the two control samples. We make use of the fact that they populate different regions of the mass triangle. In order to take into account the background distribution of the $\mu\mu$ measurement sample and to disentangle possible local effects, we split the two-dimensional phase space into 6+1 macro regions. This is shown in Figure 4.20, where the different regions approximately represent the zones populated by individual background sources: $\mu\mu(\gamma)$ contributes mostly in regions 2, 3 and 7, $\tau\tau(\gamma)$ in 1, 3, 4 and 5 and finally $ee\mu\mu$ only in macro region 5. The macro region 3 is therefore shared between the two control samples, the higher statistics given however by $\tau\tau(\gamma)$. As what concerns macro region 6, this is considered as a sideband outside the mass triangle and is mostly populated by $\tau\tau(\gamma)$ and to a lesser extent by $ee\mu\mu$. The results obtained in this section are thus most interesting in regions 2, 3 and 7 for the $\mu\mu\gamma$ control sample and in regions 1, 3, 4, and 5 for the $e\mu$ control sample. We perform the checks concerning data/MC agreement at three different levels:

1. We start with the background normalization after the preselections by computing the data/MC ratios. This is carried out in every macro region for each control sample.

2. This study is being repeated for the background shapes in the enlarged mass win-

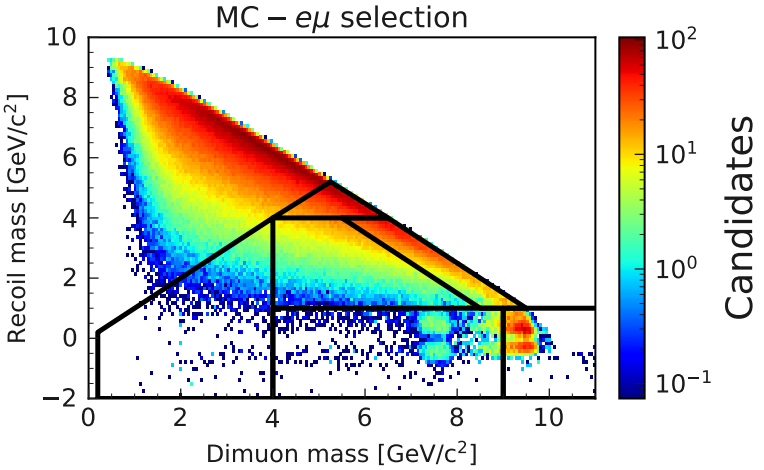

Figure 4.19.: 2d background distribution for the $e\mu$ control sample. Overlaid black lines show the macro regions.

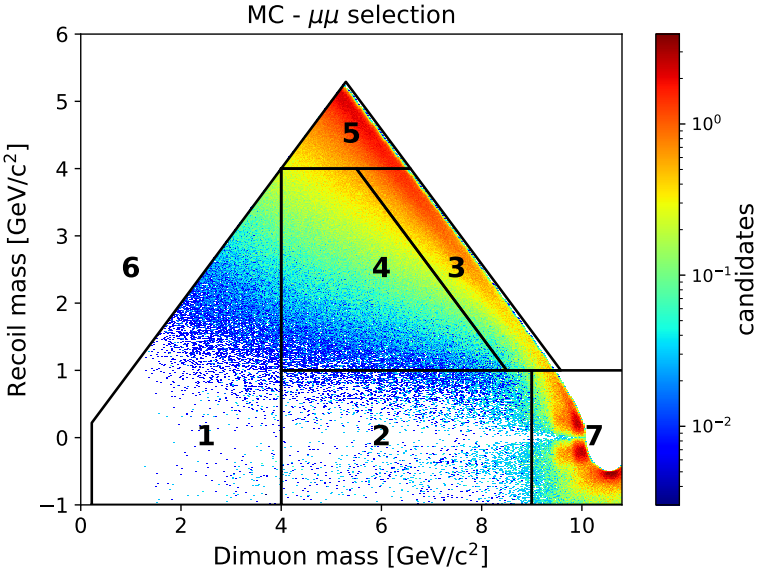

Figure 4.20.: 2d background distribution for the $\mu\mu$ measurement final state. Overlaid black lines show the macro regions and numbering.

Macro region	$\mu\mu\gamma$ data/MC	$e\mu$ data/MC
1	0.851 ± 0.013	0.918 ± 0.039
2	0.980 ± 0.004	1.071 ± 0.061
3	1.026 ± 0.013	0.969 ± 0.012
4	1.050 ± 0.010	0.974 ± 0.014
5	1.070 ± 0.046	1.004 ± 0.011
6	0.885 ± 0.022	0.981 ± 0.007
7	0.989 ± 0.006	1.127 ± 0.100
total	0.986 ± 0.003	0.984 ± 0.007

Table 4.2.: Data/MC ratios in macro regions for the $\mu\mu\gamma$ and $e\mu$ control samples. The indicated errors are statistical only. MC normalized to an integrated luminosity of $8.339\,\mathrm{fb}^{-1}$, with a trigger efficiency of 90%

dows.

3. We finally validate the final suppression variable A_E in enlarged mass windows by studying both the shape of the A_E distributions (before the cut) as well as the impact of the cut itself in every macro region.

4.6.1. Data validation in macro regions

Data/MC ratios after the preselections for the two control samples in each of the macro regions are shown in Table 4.2. There is a general good agreement, with numbers close to 1 and leaving the possibility of applying small corrections to the analysis. Averages in macro regions which are relevant for the two control samples are summarized in Table 4.3. The entire procedure is being repeated on the measurement $\mu\mu$ sample after the unblinding.

Macro region(s)	control sample	data/MC
1,4,5,6	$e\mu$	0.979 ± 0.005
3	$e\mu$	0.948 ± 0.012
3	$\mu\mu\gamma$	1.020 ± 0.014
2,7	$\mu\mu\gamma$	0.979 ± 0.003

Table 4.3.: Data/MC ratios in macro regions or group of macro regions most relevant for the $\mu\mu\gamma$ and $e\mu$ control samples. The indicated errors are statistical only. MC normalized to an integrated luminosity of $8.339\,\mathrm{fb}^{-1}$, with a trigger efficiency of 90%

Example distributions of relevant analysis variables for the two control samples are shown in Figure 4.21 and Figure 4.22, both for selected macro regions and for the full phase space. The data/MC agreement is always satisfactory, with the exception of the

Macro region	control sample	data/MC	Pull mean	Pull std
1	$e\mu$	0.90 ± 0.04	0.24	1.35
2	$\mu\mu\gamma$	0.982 ± 0.004	0.27	1.48
3	$\mu\mu\gamma$	1.05 ± 0.01	0.30	1.41
3	$e\mu$	0.97 ± 0.01	-0.16	1.12
4	$e\mu$	0.97 ± 0.01	0.13	1.10
5	$e\mu$	1.01 ± 0.01	-0.02	0.89
7	$\mu\mu\gamma$	0.98 ± 0.01	0.83	2.19

Table 4.4.: Data/MC ratios in macro regions most relevant for the $\mu\mu\gamma$ and $e\mu$ control samples (see Section 4.6). Pulls (mean values and std) of data/MC ratios in enlarged mass windows with respect to the macro region. MC normalized to an integrated luminosity of $8.339\,\mathrm{fb}^{-1}$, with a trigger efficiency of 90%

nCDCHits variable, which is anyway not a recommended choice for characterization of the track quality and known to be mismodeled in MC.

4.6.2. Data validation of background shapes after preselections

So far we have only validated the background normalization, both globally and in macro regions. We now focus on the background shapes. For this purpose the $\mu\mu\gamma$ and $e\mu$ control samples are being used at the enlarged mass window level in order to guarantee a reasonable number of events (see Section 4.4.2). As these enlarged windows overlap significantly, their contents are largely correlated. To mitigate this effect, we select a subset of 300 out of the total 9003 mass windows, which are placed on a sub-grid of 6σ spacing (to be compared to the standard 1σ step). This subset is being reused in the following section.

Data/MC ratios are computed in these enlarged windows for both control samples and expressed in terms of pulls, where the latter has been taken w.r.t 1 or the value computed in the macro region to which the mass windows belongs to. The obtained results are presented in Table 4.4 only for the macro regions most relevant for the different control samples. We expect the mean values of the pulls to be compatible with 0 and their standard deviation (std) to be close to 1. This holds for the $e\mu$ control sample but larger deviations are observed for the $\mu\mu\gamma$ control sample.

In order to further investigate these results, we study the position of the mass windows with pull values exceeding 2. We expect 5% of the windows (2σ effect) to be affected and the concerned windows to be randomly spread across the plane. In case we observe several contiguous windows to be affected, this would point us to the anomaly observed in Table 4.4. The distributions of pulls exceeding 2 is shown in Figure 4.23. While for the $e\mu$ sample, everything matches our expectations, local effects can be spotted for the $\mu\mu\gamma$ sample. This should be related to the presence of the photon which causes a strong perturbation in the two-dimensional mass plane in comparison to the $\mu\mu$ sample. Even if a more detailed study of these effects could be worthwhile, their presence is

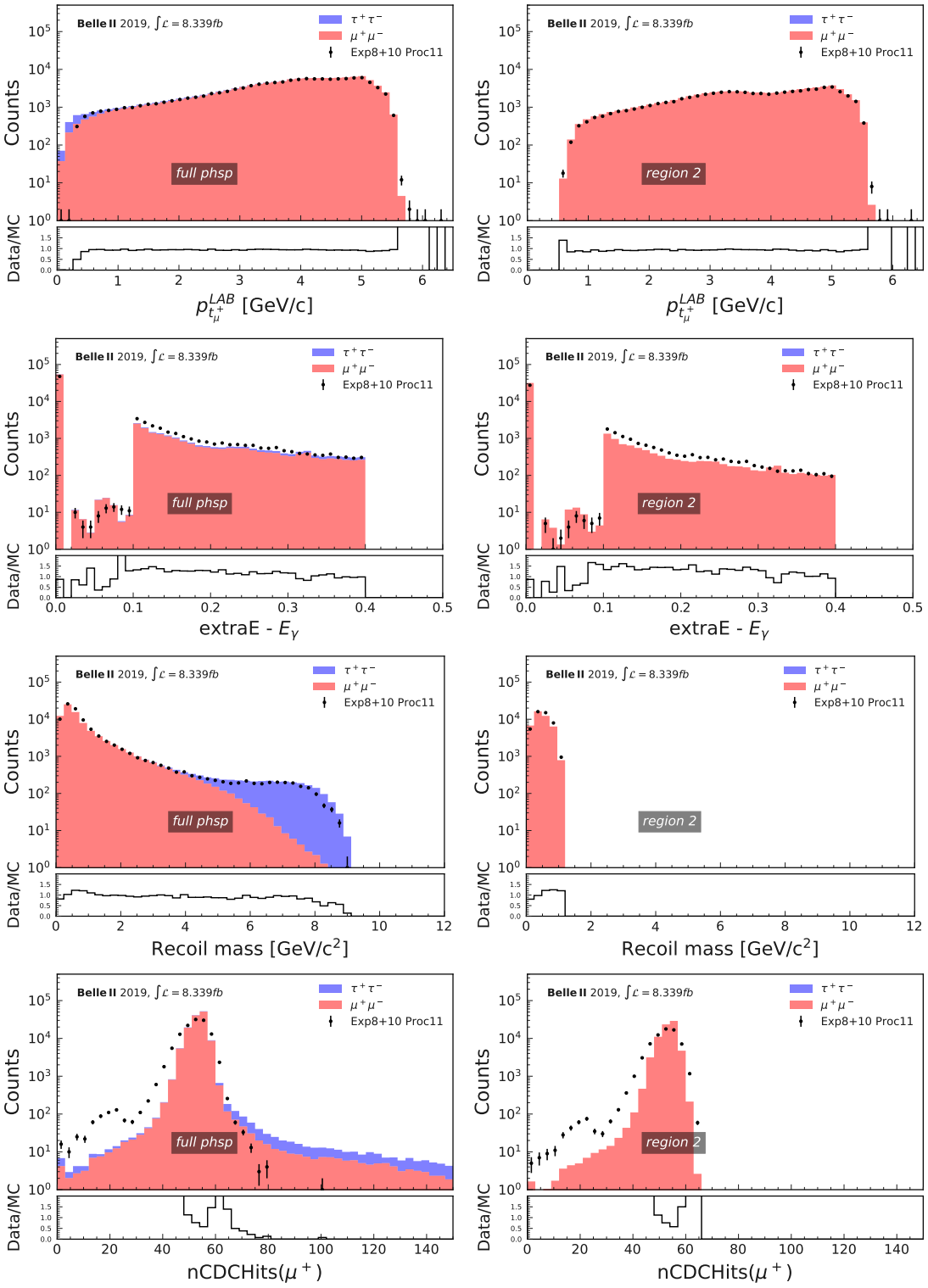

Figure 4.21.: 1d distribution of transverse momentum of the μ^+ candidate, $extraE - E_\gamma$, recoil mass and nCDCHits of the μ^+ candidate for $\mu\mu\gamma$ control sample in case of selecting events from the full phase space (left) or macro region 2 (right)

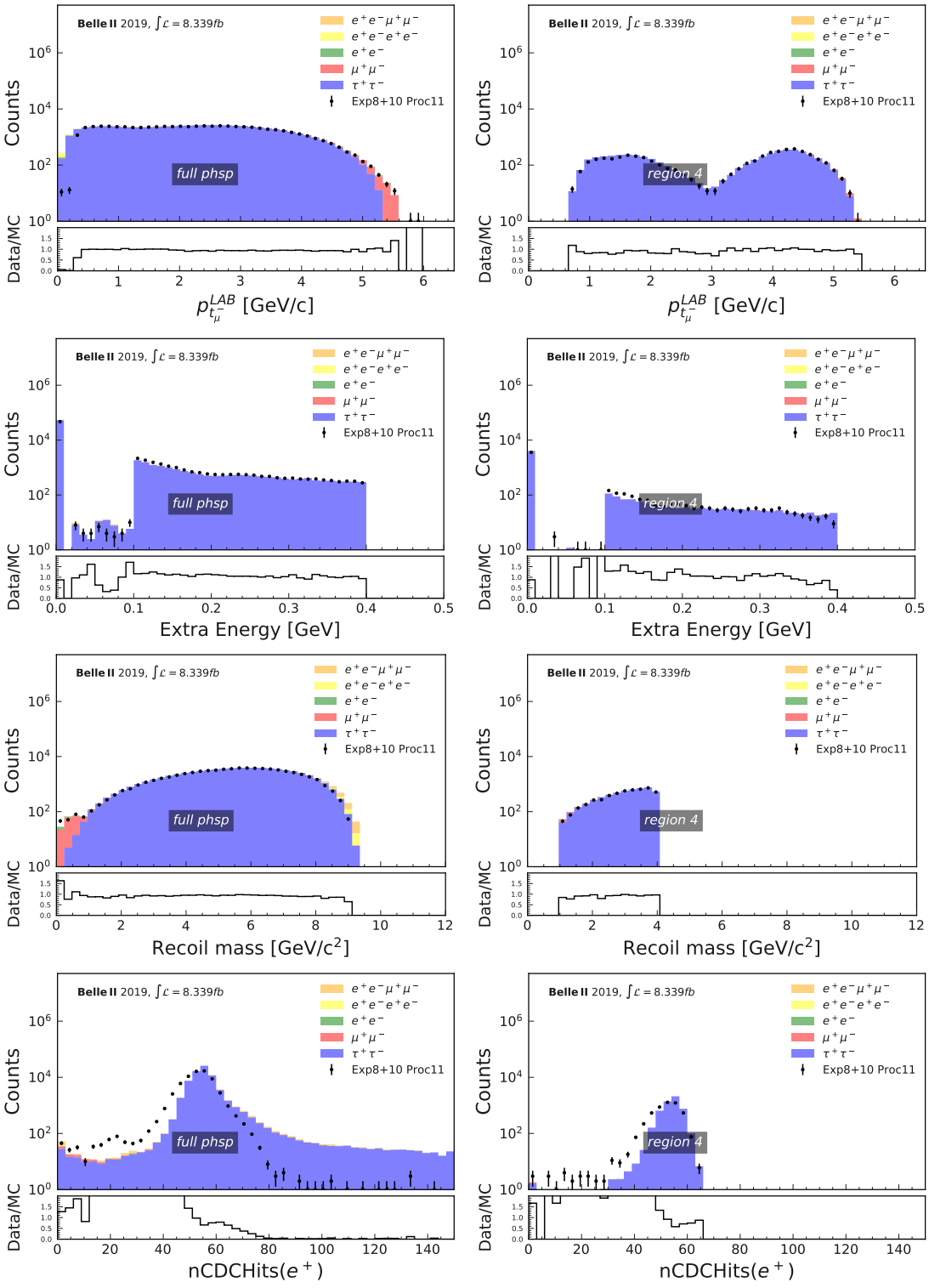

Figure 4.22.: 1d distribution of transverse momentum of the μ^- candidate, $extraE$, recoil mass and nCDCHits of the e^+ candidate for $e\mu$ control sample in case of selecting events from the full phase space (left) or macro region 4 (right)

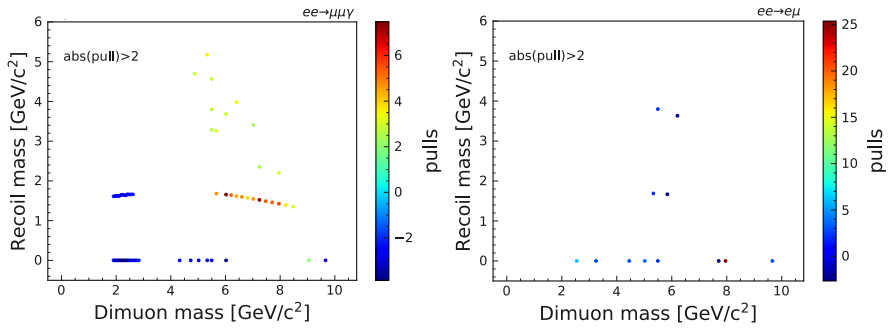

Figure 4.23.: Two-dimensional distributions of pulls exceeding 2 in absolute value for the two control samples, $\mu\mu\gamma$ (left) and $e\mu$(right)

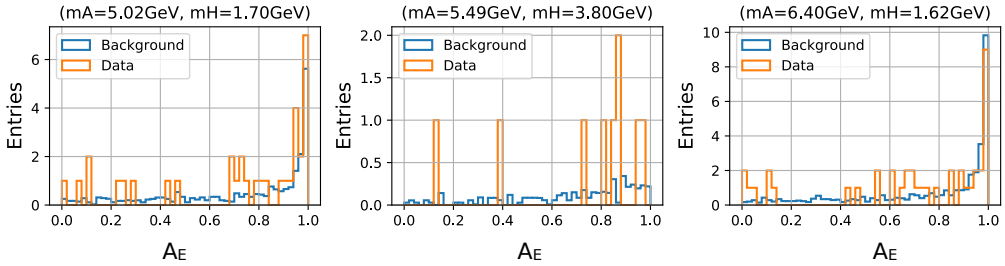

Figure 4.24.: Example of A_E distribution in data and MC for $\mu\mu\gamma$ control sample

not guaranteed in the final sample, so that further conclusions can only be drawn after unblinding.

4.6.3. Data validation of the A_E selection

I devote this section to the validation of A_E, which has been introduced in Section 4.4.3 and plays a crucial role in the final background suppression. We make use again of the two control samples and validate A_E in a twofold way: we start by evaluating the agreement of the shape of the A_E distribution in data and MC after the preselections, to be followed by a measurement of the data/MC ratios in enlarged mass windows after the selection $A_E < A_E^{cut}$ has been applied.

In what concerns the initial shape comparison, it should be noted once more that, while the $e\mu$ control sample will produce very similar A_E distributions in comparison to what is expected for the measurement $\mu\mu$ sample, this cannot be said for the $\mu\mu\gamma$ due to the presence of the photon. The data/MC values provided below for the latter sample shall therefore be meant as a check of the validity of the methodology, rather than a quantitative measure of the effect.

A few example distributions of A_E showing the different shapes in data and MC for both control samples are given in Figure 4.24 and 4.25. In order to quantify possible

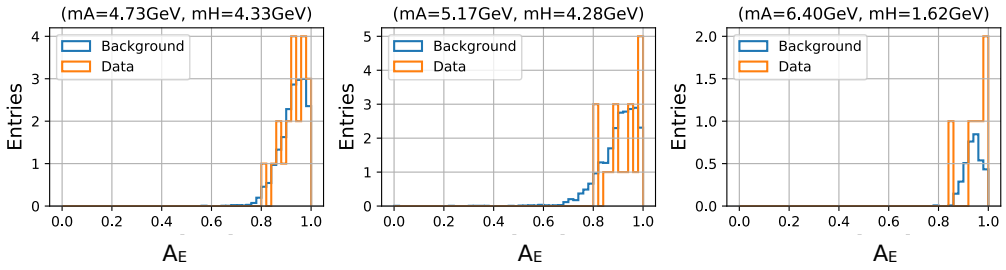

Figure 4.25.: Example of A_E distribution in data and MC for $e\mu$ control sample

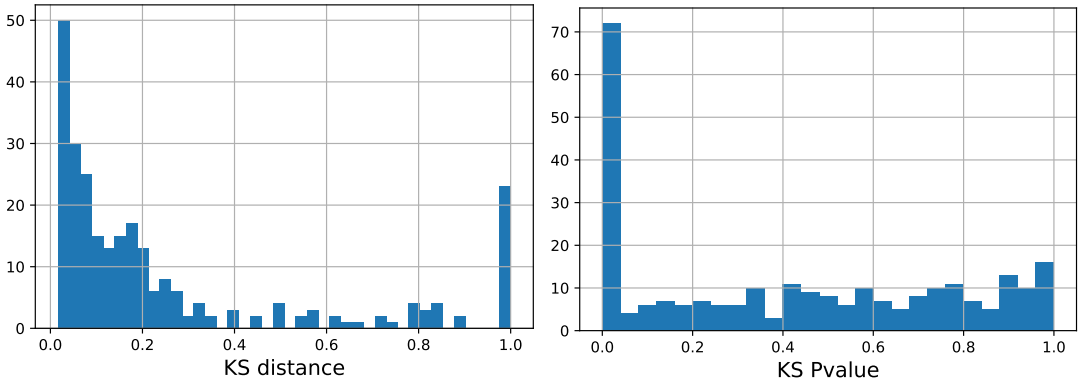

Figure 4.26.: Kolmogorov test statistic and associated p-values for $\mu\mu\gamma$ control sample

discrepancies between the respective data and MC distributions, we apply a Kolmogorov-Smirnov (KS) test. This allows for a comparison between the two samples at hand by computing the maximum distance between their cumulative distribution functions. The latter defines the KS test statistic, which is calculated under the null hypothesis that the two samples are drawn from the same distribution. A toy study is set up with 1000 pseudo-experiments generated according to MC shapes and with number of events expected from data. The associated p-value is defined as the fraction of cases in which the toy experiment returns a test statistic value larger than the observed one. The respective results for KS test statistic and p-value are shown in Figure 4.26 and 4.27. We obtain flat distributions for the p-value, which matches the expectation of agreeing shapes and minor discrepancies resulting from statistical fluctuations only. The peak at zero marks an exception and is in fact due to enlarged mass windows with 0 entries, leading to KS test statisitics of 1 and thus p-values of 0. Once these cases are removed from the first bin of the p-value histogram, the peak vanishes in case of the $e\mu$ distribution, while a small excess remains for the $\mu\mu\gamma$ one. The reason behind was closely inspected and turned out to be due to cases in which the data and MC are densely populated, so that the severity of the test and the imperfect toy generation cause small p-values. We conclude that a good agreement between data and MC was found.

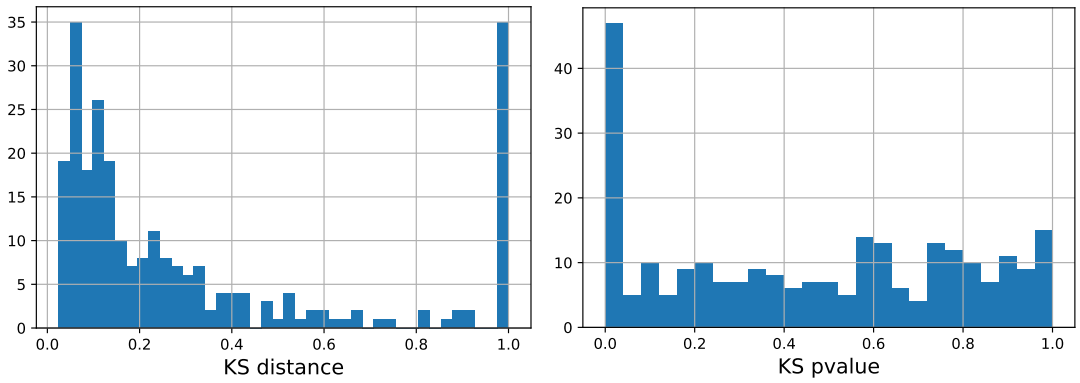

Figure 4.27.: Kolmogorov test statistic and associated p-values for $e\mu$ control sample

Macro region	control sample	data/MC presel.	data/MC A_E cut
1	$e\mu$	0.90 ± 0.04	0.43 ± 0.15
2	$\mu\mu\gamma$	0.982 ± 0.004	0.99 ± 0.01
3	$\mu\mu\gamma$	1.05 ± 0.01	1.07 ± 0.02
3	$e\mu$	0.97 ± 0.01	0.96 ± 0.02
4	$e\mu$	0.97 ± 0.01	1.04 ± 0.17
5	$e\mu$	1.01 ± 0.01	1.01 ± 0.02
7	$\mu\mu\gamma$	0.98 ± 0.01	1.08 ± 0.07

Table 4.5.: Data/MC ratios in macro regions most relevant for the $\mu\mu\gamma$ and $e\mu$ control samples. Data/MC ratios in macro regions most relevant for the $\mu\mu\gamma$ and $e\mu$ control samples at enlarged mass window level (see Section 4.4.2 after $A_E < A_E^{cut}$ selection. MC normalized to an integrated luminosity of 8.339 fb^{-1}, with a trigger efficiency of 90%

Finally, the data/MC ratios are computed in the enlarged mass windows after the $A_E < A_E^{cut}$. This selection being very effective on the majority of the mass plane, it must be considered as a check on the tail of the A_E distribution. Events in mass windows belonging to the same macro region were summed up in data and MC. Correlations are negligible because of the 6σ step spacing. The results are presented in Table 4.5. We find values close to 1, except for macro region 1, which is a low statistics region.

4.7. Systematic uncertainties

Different systematic uncertainties need to be considered for the Dark Higgsstrahlung measurement. Both the detector and the software algorithms, as well as the analysis methods presented so far give rise to sizeable effects that are evaluated in this section. Amongst others, we identified the following sources to be the most dominant: trigger and tracking efficiency, uncertainty from the luminosity measurement, muonID, effects of analysis preselections, effects of the A_E selection, mass/momentum resolution, dependence of signal efficiency on A' and h' masses, theoretical uncertainties on the model. The Higgsstrahlung being a statistically dominated measurement with very few background candidates, systematic uncertainties on the signal efficiency will have a larger impact on the final result than those on the background.

The work shown here is closely linked to the previous studies using control samples in Section 4.6. We differentiate between uncertainties affecting either signal or background and follow along the remarks below:

- uncertainties affecting the background
  - effects due to trigger, luminosity, tracking efficiency, muonID and effects of analysis preselections are collectively evaluated by the control sample study in different macro regions in Section 4.6.1. We repeat these studies on the final $\mu\mu$ sample;
  - effects due to the A_E selection have been evaluated before in Section 4.6.3 and are repeated on the final sample;
- uncertainties affecting the signal
  - effects due to trigger, luminosity tracking efficiency, muonID and effects of analysis preselections are evaluated as above with the control sample study. Strictly speaking, they are explicitly targeted at the background, but given the signal topology being very similar to those of the control sample, they impose a strong constraint on the signal too. To be repeated on the final sample;
  - effects due to muonID and analysis preselections are investigated, but will not be taken into account, the sole purpose being to exclude potential anomalies.
  - effects due to the A_E selection have been evaluated and found to be negligible, this can be understood by the underlying assumptions when constructing this

variable in Section 4.4.3, being based on the decay of a vector particle (A') into two fermions, this results in the variable showing a flat distribution, with trivial implications on the signal efficiency. In opposite to the background case, where A_E is very selective, it has a high efficiency on the signal, typically larger than 50%.

- effects due to the mass resolution are investigated below. Studies on the control samples are not sensitive to this effect, as the background distributions are integrated over areas larger than the resolution. For this same reason, this effect is considered to be null for the background;
- effects due to the dependence of signal efficiency on A' and h' masses inside the windows are given below;
- theoretical uncertainties on the model enter the branching ratio estimate of A' and affect the sensitivity and limits expressed only in terms of $\epsilon^2 \times \alpha_D$, not those on the cross-section.

The previously mentioned uncertainties related to trigger, tracking, muonID and preselections have been derived from the control sample study from Table 4.2 in Section 4.6.1. The measurement of data/MC in the macro regions does not allow for an disentanglement of individual effects but rather takes them into account globally. We therefore assume the spread of these values as an estimate of the systematic effect: a contribution of $\pm 3\%$ is assigned. Following the reasoning above the same value was assumed to the signal efficiency.

Similarly, we evaluate the effect due to the A_E selection with the results of Section 4.6.3 in Table 4.5. With the exception of region 1, all the numbers are compatible with 1, so that they may be combined and the overall effect to be estimated at $\pm 5\%$.

The dependence of the efficiency on A' and h' masses inside the mass windows are presented in more detail in Section 4.8.1 and are summarized below. In the statistical interpretation, the final deliverables such as Bayes Factors are computed using the signal efficiency value for A' and h' generated at the centre of the mass window. However, given the adopted scanning procedure, only an effective area of the mass window is relevant, outside of which the significance is higher in a nearby window. A toy study, developed for the estimation of the Look-Elsewhere-Effect, evaluates the signal efficiency for signal events inside this effective area. The rms of the distributions is shown in Figure 4.28. We assume the effect to be at the order of 5% for regions on the right-hand border of the mass plane (right tail in the plot), and a value of 2% everywhere else.

4.7.1. Mass resolution

Systematic effects may arise from the data/MC disagreement in terms of dimuon and recoil mass resolution and may affect the estimate of the signal efficiency. We evaluate them with two different approaches: first by a direct measurement of the mass resolution for a known resonance (J/ψ), followed by a measurement of the momentum resolution.

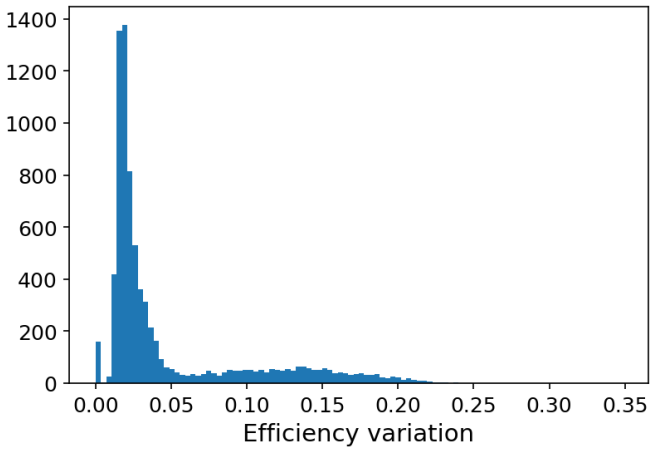

Figure 4.28.: Signal efficiency variation due to the dependence on A' and h' masses inside the mass windows.

4.7.1.1. Mass resolution from J/ψ

We start by comparing the dimuon and recoil mass resolution in data and MC. At the stage of pre-unblinding we may use $J/\psi\,\gamma_{\mathrm{ISR}}$ final states, with the J/ψ peak in the dimuon spectrum and the associated photon peak resulting from the γ_{ISR} in the recoil spectrum, for which the expectation is zero. We apply only a few of the selections introduced in Section 4.4.1, namely selection 7 regarding the cosmic veto and selection 2 requiring the polar angle of both muon tracks to be contained within a reduced ECL barrel region. In case of the dimuon mass fit we require in addition the presence of a photon with $E_\gamma > 1\,\mathrm{GeV}$ and the hie trigger bit fired in data. When performing the fit on the recoil mass spectrum we require $2.9 < M_{\mu\mu} < 3.3\,\mathrm{GeV}/c^2$, $E_{\mu,1} + E_{\mu,2} + E_\gamma > 10.5\,\mathrm{GeV}$ to limit the presence of additional photons which would spoil the expectation of a zero recoil mass, and, as before, the hie trigger bit fired in data.

For what concerns the fit PDF, we choose the sum of a Gaussian and a polynomial of first order to fit the J/ψ peak and the sum of a Crystal Ball and a Gaussian for the photon peak at zero recoil mass. We estimate the width of the peaks with the resulting fit values of the sigma σ of the Gaussian (dimuon) and the weighted sigma of the Crystal Ball and the Gaussian according to Equation 4.7 (recoil). We focus on the differences between data and the J/ψ+non-resonant $\mu\mu(\gamma)+\tau\tau$ MC sample. The results of the dimuon and recoil mass fit are shown in Figure 4.29 and 4.30 respectively. We observe discrepancies of the order of 11% (dimuon) and 15% (recoil) between the different values of the widths. In order to investigate the reason behind these discrepancies, we look at the two-dimensional momentum distribution of the two muons, shown in Figure 4.31. The distributions for data and J/ψ+non-resonant $\mu\mu(\gamma)+\tau\tau$ MC are quite different with respect to those of the signal, reflecting the nature of the involved processes (see Section 4.4.3): we therefore use a reweighting technique, to perform a comparison that better matches the signal kinematics. This procedure defines event-by-event weights, then applied when fitting

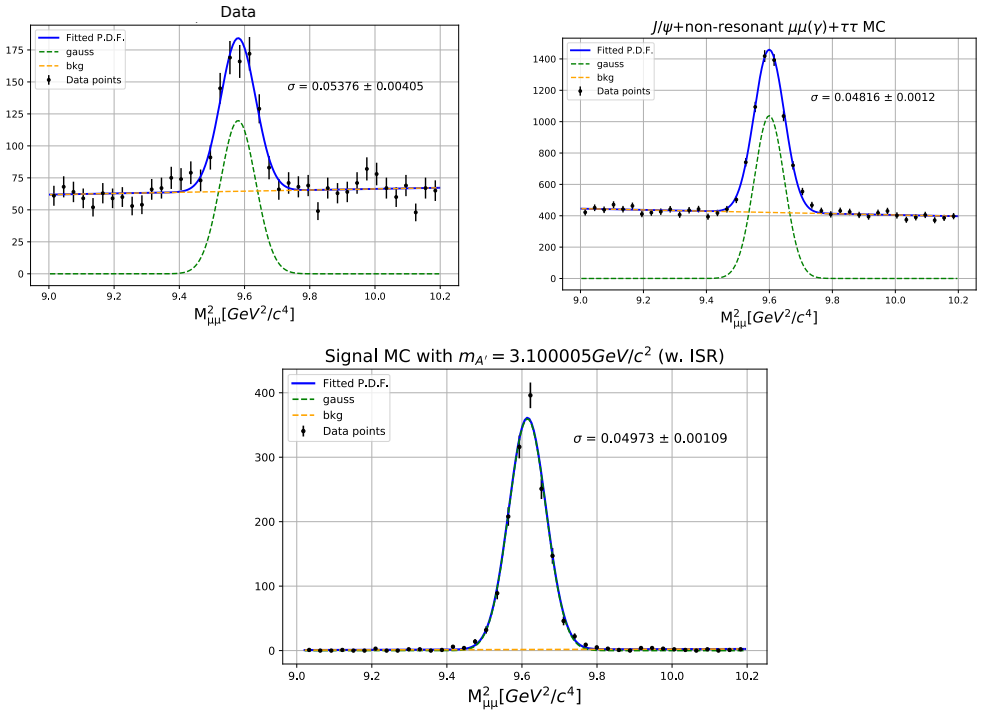

Figure 4.29.: Fitted dimuon mass distributions for data (top left), J/ψ+non-resonant $\mu\mu(\gamma)+\tau\tau$ MC (top right) and signal MC with $m_{A'} = 3.1\,\mathrm{GeV}/c^2$. The different contributions from the Gaussian and the polynomial are shown in green and yellow respectively. The indicated σ represents the width of the Gaussian.

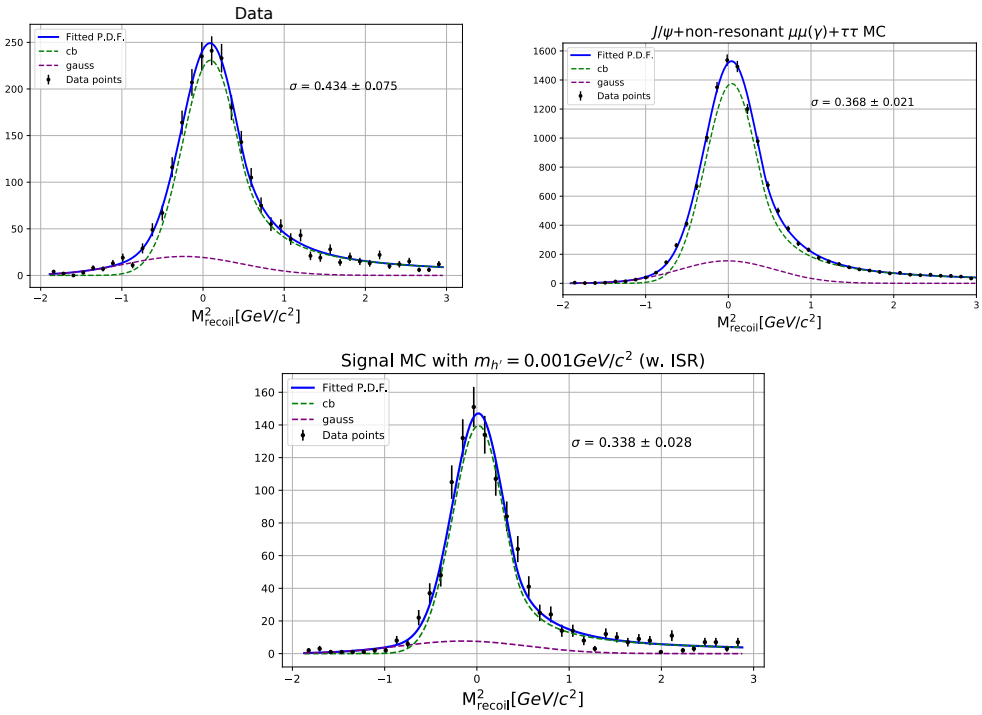

Figure 4.30.: Fitted recoil mass distributions for data (top left), J/ψ+non-resonant $\mu\mu(\gamma)$+$\tau\tau$ MC (top right) and signal MC with $m_{A'} = 3.1\,\mathrm{GeV}/c^2$. The different contributions from the Gaussian and the polynomial are shown in green and violet respectively. The indicated σ represents the weighted width of the Crystal Ball and the Gaussian according to Equation 4.7.

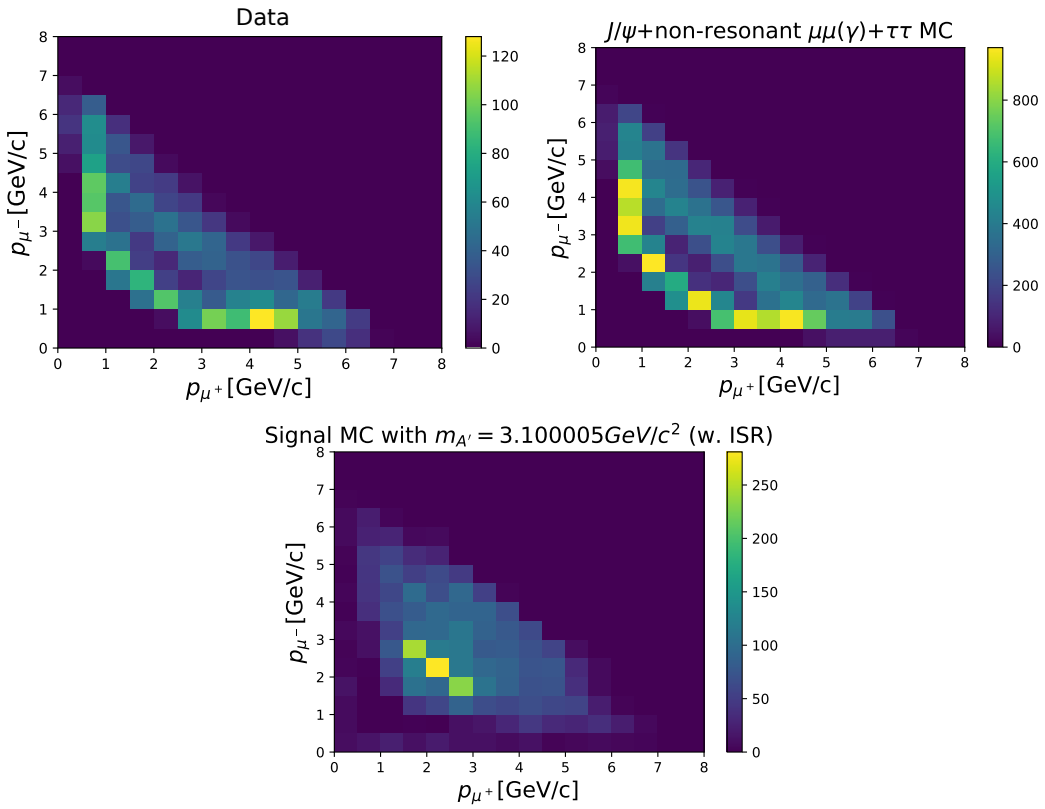

Figure 4.31.: Two-dimensional momentum distributions of the two muons for data (top left), J/ψ+non-resonant $\mu\mu(\gamma)+\tau\tau$ MC (top right) and signal MC with $m_{A'} = 3.1\,\mathrm{GeV}/c^2$. The chosen bin size is $0.1\,\mathrm{GeV}/c \times 0.1\,\mathrm{GeV}/c$.

the dimuon and recoil mass distributions. The fitted distributions after the reweighting technique are shown in Figure 4.32 and 4.33. The observed discrepancies are reduced to $1 \pm 5\%$ (dimuon) and $6 \pm 7\%$ (recoil), respectively. We keep the largest among the measured discrepancies and their errors: 5% for the dimuon mass and 7% for the recoil.

These preliminary results need to be extended from the local J/ψ region to the full mass plane. We first estimate the contributions σ_X that, added in quadrature to the MC width, reproduce the fitted values in data. Under the assumption that σ_X applies over the full mass plane, we convolve both the dimuon and recoil mass distributions with a Gaussian of width σ_X. We effectively spread the mass points according to extractions from a Gaussian of width σ_X. This is done along the correlation axes. After the application of the preselections, the variation of efficiency in the mass window is estimated. Results are shown in Figure 4.34. After data unblinding, we will apply this same technique for masses close to the $\Upsilon(4S)$ region, making use of the beam constraint.

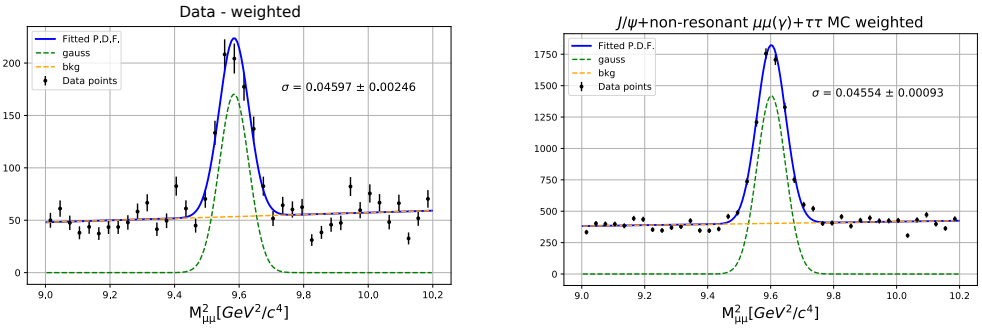

Figure 4.32.: Fitted dimuon mass distributions for data (left) and J/ψ+non-resonant $\mu\mu(\gamma)+\tau\tau$ MC (right) with momentum weights applied. The different contributions from the Gaussian and the polynomial are shown in green and yellow respectively. The indicated σ represents the width of the Gaussian.

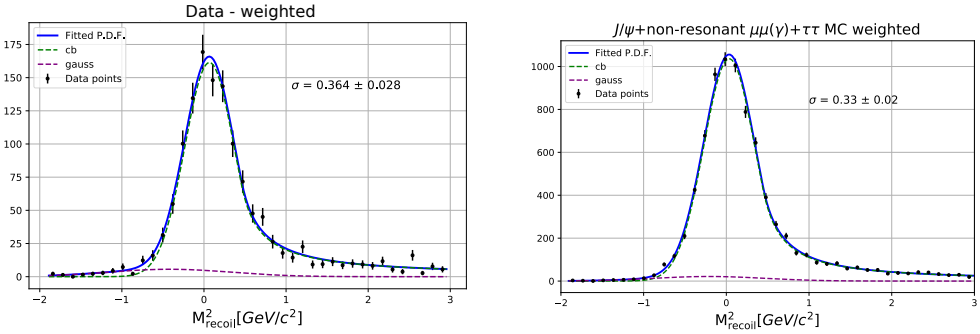

Figure 4.33.: Fitted recoil mass distributions for data (left) and J/ψ+non-resonant $\mu\mu(\gamma)+\tau\tau$ MC (right) with momentum weights applied. The different contributions from the Gaussian and the polynomial are shown in green and violet respectively. The indicated σ represents the weighted width of the Crystal Ball and the Gaussian according to Equation 4.7.

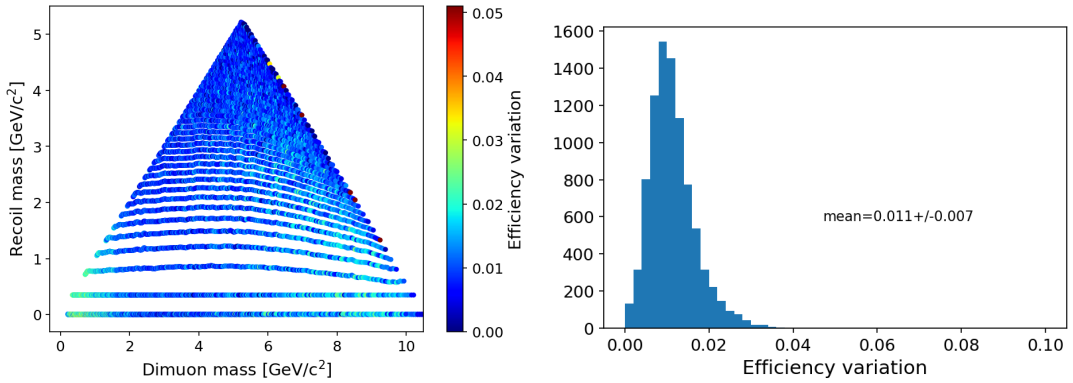

Figure 4.34.: Signal efficiency variation due to mass resolution difference in data and MC, measured at the level of the J/ψ resonance and propagated across the full mass plane. Left: as a function of the dimuon and recoil mass. Right: one-dimensional histogram.

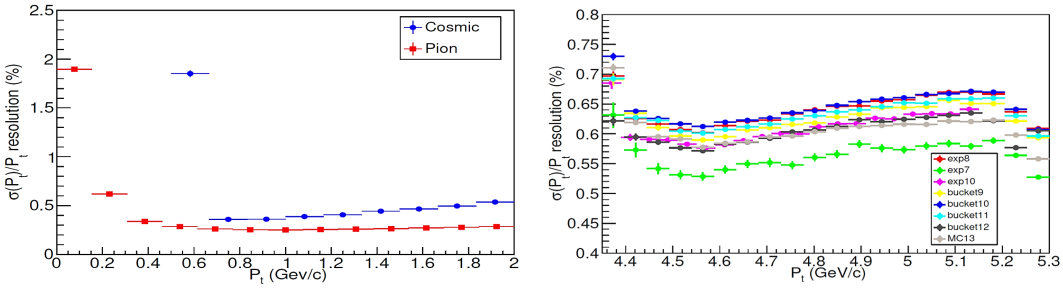

Figure 4.35.: Left: $\sigma(p_t)/p_t$ resolution in bins of p_t for slow pions (MC) and cosmics. Right: $\sigma(p_t^*)/p_t^*$ resolution in bins of p_t^* for a dimuon sample, for MC and data.

4.7.1.2. Mass resolution from momentum resolution

The previously obtained results suffer from their limitation to the J/ψ region, so that they might not provide an adequate description of the complete situation. A complimentary approach is therefore investigated, in which we exploit the fact that mass resolution is mostly due to momentum resolution with other effects being negligible. The momentum resolution has been estimated in two different intervals in a separate Belle II study and we present the most relevant results in Figure 4.35. As before we compute the contribution σ_p that needs to be added in quadrature to the MC curve in order to match the resolution in data: these are 0.31% and 0.19% for $p_t < 2\,\text{GeV}/c$ and $4.4 < p_t < 5.3\,\text{GeV}/c$, respectively. For intermediate values in between $2 < p_t < 4.4\,\text{GeV}/c$, a linear interpolation between 0.31% and 0.19% is used. In a similar procedure than before we spread the momentum distribution by convolving it with Gaussian of width σ_p. The analysis selections are then applied and the variation of the efficiency is computed. Results are shown in Figure 4.36.

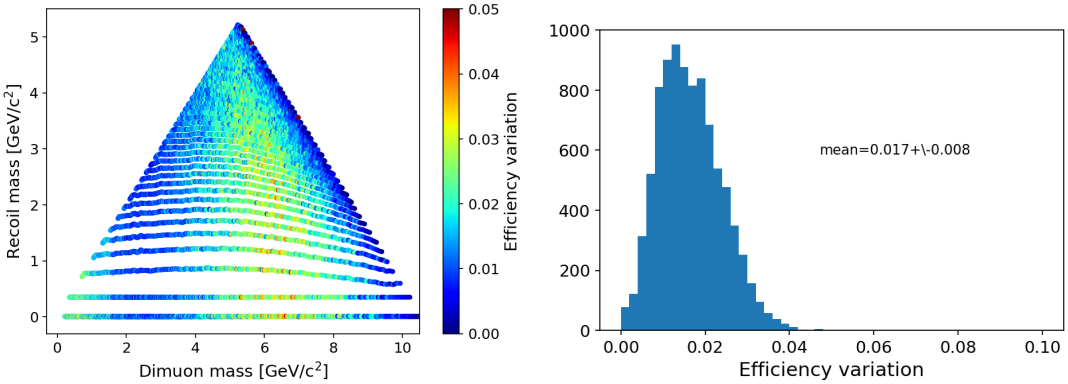

Figure 4.36.: Signal efficiency variation due to the momentum resolution difference in data and MC. Left: as a function of the dimuon and recoil mass. Right: one-dimensional histo.

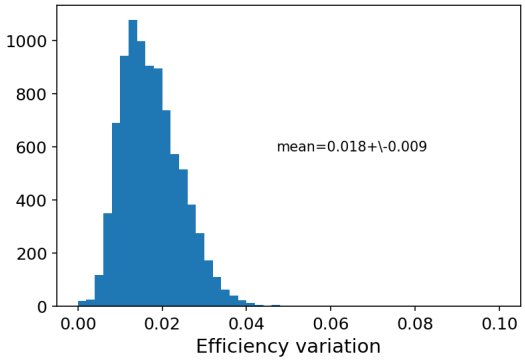

Figure 4.37.: The worst of signal efficiency variations due to the momentum resolution or mass resolution difference between data and Monte Carlo.

We finally combine the results from both approaches by assigning for every mass window the worst of the two cases. The resulting distribution is shown in Figure 4.37. A value of $\pm 3\%$ is assumed all across the mass plane.

4.7.2. muonID effects

Studies described in this section are performed as a check, and results not used in the total systematic uncertainty evaluation, as they are already included in the macro region studies (see Section 4.6.1). The systematic effects arising from muonID may be estimated by assigning an uncertainty of 2% (0.5%) for tracks with momentum value below (above) 1.5 GeV/c. For every event contained in a given macro region we then compute $u = \sqrt{u_{\mu,1}^2 + u_{\mu,2}^2}$, where $u_{\mu,i}^2$ is either 2% or 0.5% as previously described. The mean value of u in all the macro regions is given in Table 4.6. We evaluate this effect to be of the

Macro region	$\bar{u}$
1	1.98%
2	0.83%
3	0.71%
4	0.95%
5	1.02%
6	1.82%
7	0.71%
full mass plane	0.85%

Table 4.6.: Mean values of $u = \sqrt{u_{\mu,1}^2 + u_{\mu,2}^2}$ in different macro regions.

order of 2%.

4.7.3. Preselection effects

Studies described in this section are performed as a check, and results not used in the total systematic uncertainty evaluation, as they are already included in the macro region studies (see Section 4.6.1). We study the effects on the data/MC agreement possibly induced by the analysis preselections using the two control samples $\mu\mu\gamma$ and $e\mu$ introduced in Section 4.6. The exact same selections are applied, with the exception of four cuts whose individual impact on the data/MC agreement we want to check. The remaining set of selections applied during these checks is referred to as "baseline selection". The four cuts of interest are given below:

- $\mu\mu\gamma$ control sample
  - θ_γ: The polar angle of the photon is required to be in the ECL barrel region.
  - E_γ+ROE: The photon energy is required to be larger than 1 GeV and $extraE - E_\gamma < 0.4\,\text{GeV}$.
  - θ_{recoil}: The recoil momentum should be pointing to the ECL barrel region.
  - $p_{\mu\mu}^T$: The transverse dimuon momentum should be larger than 0.1 GeV/c.
- $e\mu$ control sample
  - no close γ: Events with a photon within a 15° cone are rejected.
  - ROE: Low activity is required in the ROE with $extraE < 0.4\,\text{GeV}$.
  - θ_{recoil}: The recoil momentum should be pointing to the ECL barrel region.
  - $p_{e\mu}^T$: The transverse electron-muon momentum should be larger than 0.1 GeV/c.

For each of these cuts we compute in every macro region the data/MC agreement first by excluding the same cut and applying every other selection (baseline+remaining 3 cuts)

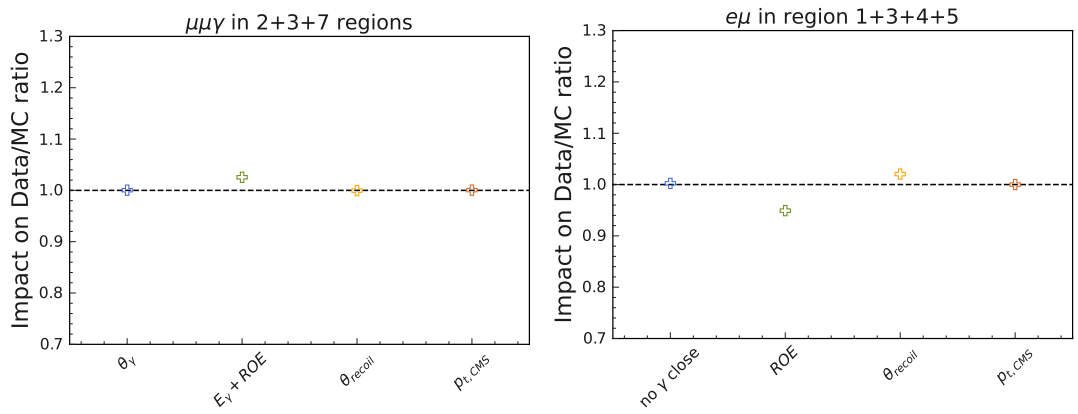

Figure 4.38.: Impact of individual cuts on data/MC agreement as defined in Equation 4.8 for both control samples $\mu\mu\gamma$ and $e\mu$ in the most relevant macro regions.

and then again with this cut applied on top. This will allow us to compute the ratio of data/MC agreement before and after, so that we can effectively estimate its impact with:

$$\text{impact} = \frac{\text{data/MC}_{\text{after}}}{\text{data/MC}_{\text{before}}} \tag{4.8}$$

The resulting impact values for every cut are shown in Figure 4.38 for both control samples in the most relevant macro regions. Most of the values are close to 1 with the biggest discrepancy arising from the ROE cut in the $e\mu$ control sample. We therefore estimate a value of 5% for this systematic effect.

4.7.4. Results

An overview of the systematic uncertainties that have been presented in this section is given in Table 4.7. They represent the best effort for estimating the different effects before unblinding and are therefore subject to minor changes once the unblinding is done. In order to compare the systematic and statistical contribution to the overall error, the relative statistical error on the expected background is shown in addition in Figure 4.39. For the majority of the phase space the latter dominates over the systematic one.

Source	estimated effect	target
trigger, lumi, tracking, muonID, presel	3%	background
A_E cut	5%	background
total background	5.8%	
trigger, lumi, tracking, muonID, presel	3%	signal
mass resolution	3%	signal
ϵ_{sig} inside mass window	2%	signal
theory (BR A')	4%	signal
total signal	6.2%	

Table 4.7.: Systematic uncertainty sources, estimate of the effect on signal and background.

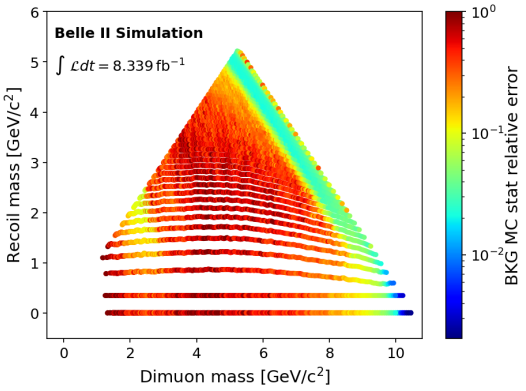

Figure 4.39.: Statistical relative error for the expected background.

4.8. Statistical interpretation

We opt for a Bayesian approach for the statistical evaluation of this measurement. Due to the small number of background events remaining after the preselections, we decide to set up a counting procedure instead of a fitting technique. We therefore compare the number of observed events with the expected background in the mass windows.

The exclusion upper limits are computed with the Bayesian Analysis ToolKit (BAT, [41]) For each mass window the following equation holds:

$$N = \sigma_{DH} \times \mathcal{L} \times \epsilon_{\text{sig}} \times \epsilon_{\text{trigger}} + b \tag{4.9}$$

where N is the number of observed events, ϵ_{sig} is the signal efficiency, b is the expected MC background and σ_{DH} is the cross-section of $e^+e^- \to A'h'$; $A' \to \mu^+\mu^-$, $h' \to$ invisible process.

The choice of the individual prior distributions is based on the following assumptions:

- the likelihood distribution for the model, given the observed number of events, was assumed to be Poissonian;

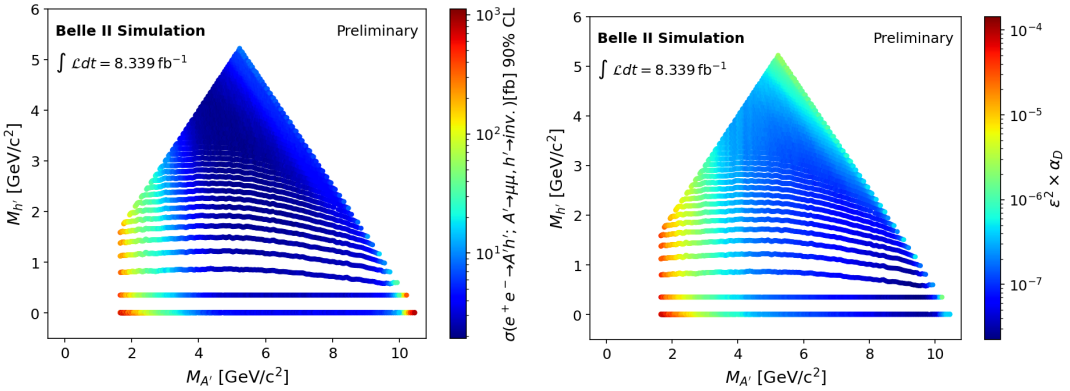

Figure 4.40.: Sensitivities after the final background suppression (A_E selection) estimated with a Bayesian approach. Left: 90% CL upper limits on the cross-section σ_{DH}. Right: 90% CL upper limits on $\epsilon^2 \times \alpha_D$.

- the prior distribution for the cross-section σ_{DH} was assumed to be flat between 0 and $100 \times \sqrt{b}/(\mathcal{L} \times \epsilon_{\mathrm{sig}})$fb (with the luminosity expressed in fb^{-1});
- all the prior distributions related to systematic uncertainties were assumed to be Gaussian, with a width equal to the estimated size of the effect;
- the expected number of events in (Monte Carlo) background was assumed to be Poissonian.

Regarding the systematic effects, we refer to the values provided in Table 4.7. All the listed sources are treated as uncorrelated and summed in quadrature for signal and background, except for the results related to the macro region validation study (accounting for trigger, tracking, luminosity, muonID and preselection cuts), which is assumed to be fully correlated between signal and background. Under these assumptions, the BAT toolkit can be used to estimate a 90% CL upper limit on σ_{DH} with Equation 4.9. At the stage of pre-unblinding, we can only compute our sensitivity on σ_{DH}, defined as the average upper limit obtained by an ensemble of pseudo-experiments with the expected background b and no signal.

Preliminary results for the sensitivity on σ_{DH} are shown in Figure 4.40 on the left as a function of the dimuon and recoil mass. These results can then be translated into upper limits in terms of the coupling constant times kinetic mixing parameter $\epsilon^2 \times \alpha_D$ with Equation 1.14, shown in Figure 4.40.

4.8.1. Look-Elsewhere-Effect

The Higgsstrahlung measurement is subject to a sizeable Look-Elsewhere-Effect (LEE) given the high number, 9003 in total, of mass windows. For example, the probability for a background-only fluctuation to produce a 3σ effect is 0.135%, resulting in 12.2 affected mass windows, so that the observation of such a significance is almost guaranteed.

Following on from the previous section, we choose the Bayesian approach to account for this effect.

Bayesian analysis is known to account (semi)automatically for the LEE, often addressed as "Ockham's razor": choosing too complicated hypotheses leads to suppression factors [42]. The latter arise as the ratio of the posterior to prior "mass", a broad prior distribution which ends up in a narrow posterior distribution will naturally produce a high suppression factor, which can be interpreted as the price to be pay in case of a large initial search space.

Hypothesis testing in the Bayesian approach is formalized through the usage of Bayes factors, which compare two different hypotheses, H_0 being the background only case and H_1 being signal +background. The signal s can be written as $s = \epsilon_{\text{sig}} \times \mathcal{L} \times \sigma_{DH}$, where as before ϵ_{sig}, $\mathcal{L}$ and σ_{DH} refer to signal efficiency, integrated luminosity and cross-section.

In a given mass windows W, the Poissonian likelihood for N observed events and predicted background b in the signal+background case is:

$$P(N/s+b)\frac{(s+b)^N e^{-(s+b)}}{N!} \tag{4.10}$$

leading to a Bayes factor of H_1 to H_0 of:

$$B_{10}(W) = \frac{E_1}{E_0} = \frac{\int_0^\infty (s+b)^N e^{-(s+b)} \pi_1(b,s) ds}{b^N e^{-b}} \quad ; s = \epsilon \times L \times \sigma_{DH} \tag{4.11}$$

where $\pi_1(b,s)$ is the prior probability for a signal given the background b. These expressions hold for an exactly known background b. In our case, each time b appears, a marginalization is implied, to take into account systematic uncertainties and Monte Carlo statistics. The B_{10} thereby quantifies how much stronger the H_1 hypothesis is w.r.t. H_0.

As what concerns the choice of the prior, we opt for a so-called intrinsic prior based on [43]:

$$\pi_1(s) = \frac{b}{(s+b)^2} \tag{4.12}$$

We make use again of BAT for the numerical calculation of $B_{10}(W)$. As for the upper limit estimation of the previous section, the systematic uncertainties are taken into account both uncorrelated and correlated for signal and background. The next crucial step towards global hypothesis testing, with full evaluation of the LEE, is the introduction of the true signal mass dependencies. This is achieved by adding the dark photon mass $M_{A'}$ and the dark Higgs mass $M_{h'}$ as nuisance parameters, with a related prior probability distribution $\pi(M)$:

$$\pi(M) = \frac{1}{A_T} \qquad \text{and} \qquad M = (M_{A'}, M_{h'}) \tag{4.13}$$

where the triangle area of the phase space is given by $A_T = 27.98\,\text{GeV}^2$. We finally obtain after a few more steps, which shall be omitted here:

$$B_{10}^{GLOBAL}(W) = B_{10}(W)\frac{1}{A_T}\int_{\epsilon_W(M)>0} dM^2 \frac{1}{2\sqrt{M_{A'}^2}}\frac{1}{2\sqrt{M_{h'}^2}} \tag{4.14}$$

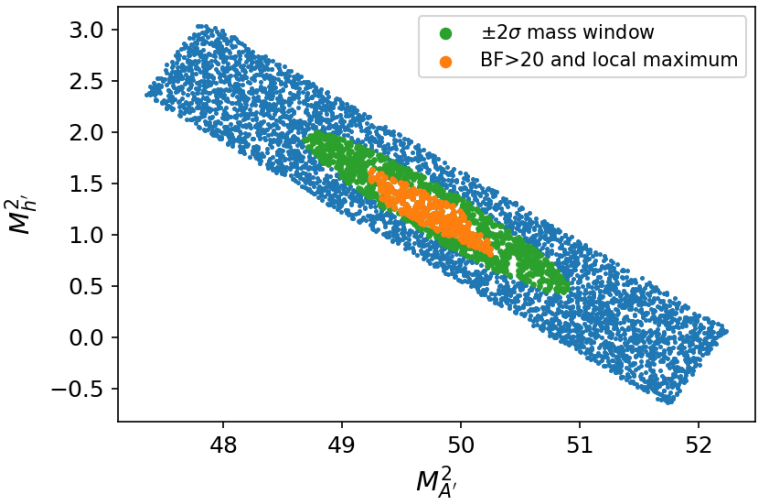

Figure 4.41.: Example of the toy Monte Carlo procedure applied on a central mass window. In blue, the rectangular region in which the A_M condition is checked. In green, the mass window. In orange, the region in which the A_M condition is fulfilled.

A few remarks shall be added here:

- as the mass windows live in the squared mass space, the prior $\pi(M)$ needs to be translated into $\pi(M^2)$, resulting in the last two factors in the above equation
- the integration space in dM^2 receives only contributions where ϵ_W (the efficiency in the mass window W for a signal of true mass M after all the selections) is non-zero
- the integration over ds does not depend on $\epsilon_W > 0$, so that $B_{10}(W)$ may be taken out of the integral

This result will allow to establish a direct connection between local and global Bayes factors. The suppression factors

$$\frac{1}{A_T}\int_{\epsilon_W(M)>0} dM^2 \frac{1}{2\sqrt{M^2_{A'}}}\frac{1}{2\sqrt{M^2_{h'}}} \tag{4.15}$$

can be numerically computed through integration prior to data unblinding. We will now further adapt the results obtained so far to the situation emerging after unblinding. At that moment, we limit ourselves to mass windows with local Bayes factors being the local maxima among neighbouring windows and with values above a pre-defined threshold. This effectively acts a constraint A_M on the integration region in Equation 4.14, so that $\epsilon_W(M) > 0 \cap A_M$, with $A_M \equiv \quad M : \; B_{10} > B^T_{10} \cap B_{10}\; max$ and B^T_{10} being the custom threshold.

Due to the window overlap, the condition $\epsilon_W(M) > 0 \cap A_M$ is expected to be fulfilled by regions smaller than the mass windows: a signal contained in one mass window can give rise to a higher Bayes factor in a nearby window where the same signal is located in a more central position. We therefore need to restrict the integration to portions of the mass window in which a signal would give the maximum local Bayes factor over threshold. In order to find these regions, a Monte Carlo simulation is set up and the results are presented in Figure 4.41 for one mass window. Background events are extracted from a Poissonian distribution with expected values according to Figure 4.10, while signal events are injected within a set of predefined values (0.1,1,3,10,30,100). For a total of 1000 generated mass points inside a rectangular region the condition A_M is evaluated, by identifying the cases in which the Bayes factor of the central mass window is the largest and over the threshold. They define an effective area of size $2\sigma \times 2\sigma$, which is smaller than the central window ($4\sigma \times 4\sigma$). The procedure was further validated with a number of trial runs for the different signal levels in order to confirm the asymptotic convergence of the size of the area in which A_M is fulfilled. We will apply this exact procedure after unblinding with the only difference being a continuous signal injection based on the posterior distribution after N_{obs} have been observed.

Before unblinding, we set up a different procedure to estimate the global suppression factors at a more coarse level. Under the assumption of a low and smoothly varying background, the local significance and therefore the Bayes factor is driven by the signal efficiency. The previous A_M condition may therefore be reduced to the signal efficiency having a local maximum:

$$B_{10}^{GLOBAL}(W) = B_{10}(W)\frac{1}{A_T}\int_{\epsilon_W(M)>0 \cap \epsilon_W(M)\ max} dM^2 \frac{1}{2\sqrt{M_{A'}^2}}\frac{1}{2\sqrt{M_{h'}^2}} \tag{4.16}$$

With a Monte Carlo procedure very similar to the one described above (background can be omitted with the signal efficiency being the only relevant parameter, and no computation of Bayes factor), we find the portions of mass window in which this condition holds. Results are shown in Figure 4.42 for one mass window. An effective area inside the central mass window is found, where the signal efficiency of the central window for signals with masses belonging to this region is the largest among all the neighbours.The resulting suppression factors are computed and shown in 4.43. The values are at the order of 10^{-4}, which is compatible with the expectation of the inverse of the number of mass windows. This method can be used in addition to estimate the variation of signal efficiency inside the effective area. This is reported in Section 4.7.

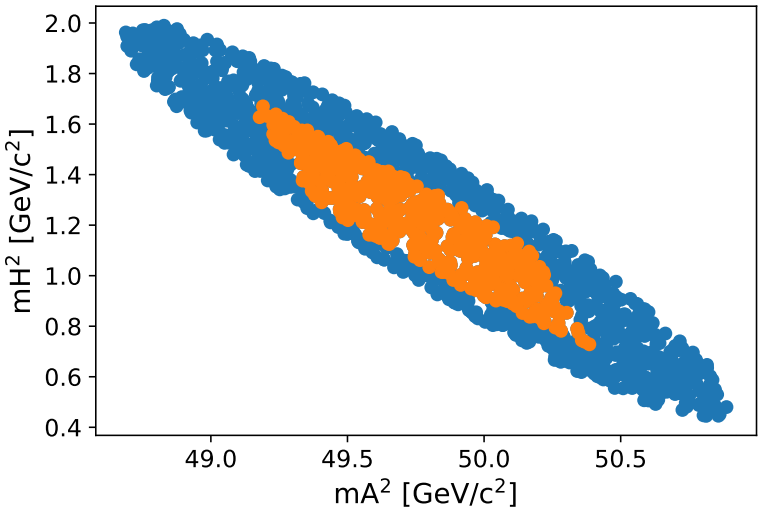

Figure 4.42.: Example of a central mass window. In orange, the region in which the signal efficiency of the central window for signals with masses belonging to this region is the largest among all the neighbours.

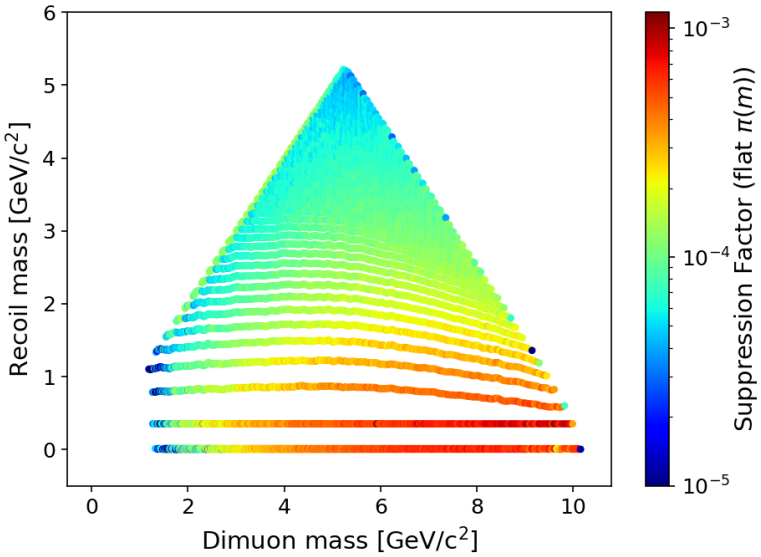

Figure 4.43.: Suppression factors relating local to global Bayes factors under the flat prior mass hypothesis.

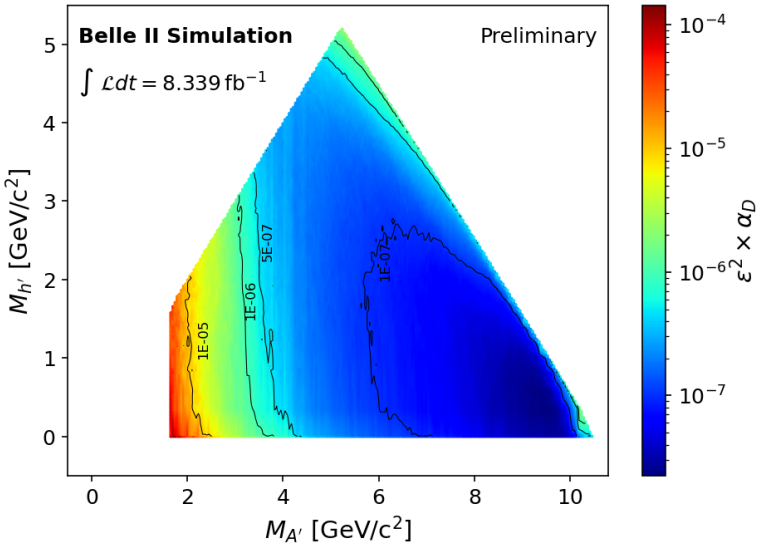

Figure 4.44.: Smoothed sensitivities in $\epsilon^2 \times \alpha_D$ after the final background suppression (A_E selection) estimated with a Bayesian approach. Contour lines corresponding to $\epsilon^2 \times \alpha_D$ of 10^{-7}, 5×10^{-7}, 10^{-6} and 10^{-5} are shown.

4.9. Results and Outlook

The unblinding procedure of the measurement only started at the time of writing, so that the final results cannot be shown within the context of this thesis. I therefore show another version of the sensitivity estimate in $\epsilon^2 \times \alpha_D$ of Figure 4.40 in Figure 4.44, where a smoothened representation of the values was chosen for better readability. It should be noted again, that the only previous result of the Dark Higgsstrahlung was obtained by the KLOE experiment. Given the much lower centre-of-mass energy of the latter ($\sqrt{s} \sim 1\,\mathrm{GeV}$), Belle II will be able to probe unconstrained regions of the phase space. Moreover, in Figure 4.44, it can be seen that limits in terms of $\epsilon^2 \times \alpha_D$ will be at the order of 5×10^{-7} for the majority of the phase space: under the assumption of $\alpha_D = 1$, this can be read as $\epsilon \sim 7 \times 10^{-4}$, and qualitatively compared with the results shown in Figure 1.3. Belle II will therefore also probe non-trivial regions of kinematic mixing parameter.

As of right now, no limits can be set in the region of low dark photon and dark Higgs mass values (an arbitrary cut-off value of $M_{A'} < 1.65\,\mathrm{GeV}/c^2$ was chosen). This is related to the usage of the ffo trigger line and the implied requirement of the opening angle of the two tracks to be greater than 90°, which can hardly be met by muons from a low-mass dark photon decay (and therefore highly boosted), leading to negligible sensitivities. When this measurement will be repeated with the much larger data sets collected by Belle II, it will be beneficial to switch to different trigger lines, such as ff30 (see Section 3.1), with which it will be possible to recover these regions.

5. Z' to invisible

The following work was done in collaboration with four other PhD students Marcello Campajola [1], Laura Zani [2], Giacomo De Pietro [3]and Alberto Martini [3]; guidance and additional work was provided by Gianluca Inguglia, Enrico Graziani [3] and Ilya Komarov [4]. The author provided major contributions to the results presented in Section 5.5, 5.6 and 5.9.

5.1. Analysis overview

Following on from the previous section, I now consider the invisible decays of a light Z' boson in two different models: a Z' belonging to a $L_\mu - L_\tau$ symmetry, as introduced in Section 1.2.2 and a Z' coupling to all leptons, being also sensitive to lepton flavour violation (LFV) effects. In particular, we perform a search for the following two processes:

1. $e^+e^- \to \mu^+\mu^- Z', \qquad Z' \to \text{invisible}$
2. $e^+e^- \to e^\pm\mu^\mp Z', \qquad Z' \to \text{invisible}$

where we refer to the former as "standard Z'", and the latter as "LFV Z'". For both searches we use the data collected during the commissioning phase of the Belle II detector (Phase 2, see Section 2.1). With the same definition for the squared mass recoiling against the $\mu\mu$ and $e\mu$ system respectively (see Equation 4.1), the experimental signature is given by a bump in the recoil mass distribution. As to what concerns the expected background contamination, the same processes as in the Dark Higgsstrahlung measurement contribute, namely $\mu\mu(\gamma)$, $\tau\tau(\gamma)$ and $ee\mu\mu$ (see Section 4.1).

The reconstruction of candidate events is presented in Section 5.3, followed by a more rigorous selection of events in Section 5.4. As we observe the biggest background contribution to be arising from $\tau\tau(\gamma)$ events, we apply a dedicated suppression procedure in Section 5.4.2. As all of these steps are performed with Monte Carlo samples (see Section 5.2), a separate data validation with control samples is required in Section 5.7. This not only allows for the check of the background estimate, but also for the derivation of correction factors and systematic uncertainties for background and signal efficiency. We finally compute 90% CL upper limits for the cross section and coupling constant g' for the standard Z' process in Section 5.9 with the statistical methods of Section 5.8. As at

[1]INFN, Sezione di Napoli, Napoli, Italy
[2]INFN, Sezione di Pisa, Pisa, Italy
[3]INFN, Sezione di Roma Tre, Roma, Italy
[4]Deutsches Elektronen-Synchrotron (DESY), Hamburg, Germany

Process	$\int \mathcal{L}dt$ [fb^{-1}]
$e^+e^- \to \mu^+\mu^-(\gamma)$	56.621
$e^+e^- \to \tau^+\tau^-(\gamma)$	40.044
$e^+e^- \to e^+e^-\mu^+\mu^-$	7.406
$e^+e^- \to \pi^+\pi^-(\gamma)$	1372.539
$e^+e^- \to e^+e^-(\gamma)$	0.198
$e^+e^- \to e^+e^-e^+e^-$	6.562

Table 5.1.: List of MC samples used for background studies with the equivalent integrated luminosity $\int \mathcal{L}dt$.

the time of writing no Monte Carlo generator model is available for the LFV Z', we may only infer upper limits in terms of signal efficiency times cross section.

5.2. Data sets

For this work we use the reprocessed data collected in 2018 with an integrated luminosity of $\int \mathcal{L}dt = 479.8\,\text{pb}^{-1}$. Due to the L1 trigger configuration during the commissioning run and the resulting data quality selections applied later in Section 5.4, the effective luminosity available for this measurement is reduced to $276\,\text{pb}^{-1}$.

With the Madgraph generator [37], we produce MC samples for studies related to the $e^+e^- \to \mu^+\mu^- Z'$, $Z' \to$ invisible process. A total of 16 samples with 20000 events each are generated for Z' mass hypotheses from $0.5\,\text{GeV}/c^2$ up to $8\,\text{GeV}/c^2$, with a step size of $0.5\,\text{GeV}/c^2$.

The MC samples listed in Table 5.1 are used for background studies.

5.3. Candidate reconstruction

5.3.1. Standard Z' to invisible

A candidate event is reconstructed with two cleaned tracks (see Section 4.3), where the latter are identified as muons by applying a selection based on the energy deposited in the ECL calorimeter:

- the total energy of the cluster, clusterE $< 0.75\,\text{GeV}$, this allows for an effective electron-muon separation as electrons deposit all of their energy in the ECL ($\sim 1 - 3\,\text{GeV}$)
- the total energy of the cluster divided by the momentum value, clusterE/p < 0.5, this also allows separating muons from electrons which take values in between 0.7 and 1.3.

The two tracks are then combined to form a dimuon candidate and the event is only accepted if there are no more than four cleaned tracks. As in Section 4.3 the ROE is

reconstructed and exactly the same mask is applied to remove contamination from beam background photons.

Finally, the recoil system against the dimuon candidate with respect to the center of mass momentum is reconstructed, being the Z' candidate for the event.

5.3.2. LFV Z' to invisible

The candidate reconstruction remains the same in what concerns the cleaned track selection. One track is identified as a muon with the criteria given above, while a second one is identified as an electron by requiring:

- the total energy of the cluster, clusterE $> 1\,\text{GeV}$
- the total energy of the cluster divided by the momentum value, $0.7 <$ clusterE/p < 1.3

The oppositely charged muon and electron tracks are then combined, followed by the reconstruction of the ROE and the recoil system as above.

5.4. Event selection

5.4.1. Standard Z'

Further selection criteria are applied to suppress the background contribution. The following requirements are closely related to the ones used in Section 4.4.1:

1. there must be exactly two cleaned tracks and their opening angle in the transverse plane must exceed 90° in order to emulate the CDC trigger logic, which is not simulated in MC. In addition, that same opening angle is required to be less than 172° as described in Section 5.6.1.

2. the polar angle of the muon tracks should be contained within a restricted ECL barrel region for a good control of systematic effects ($37° < \theta_\mu < 120°$), see Section 3.5.

3. the recoil momentum must point to the ECL barrel acceptance region ($33° < \theta_{\text{recoil}} < 128°$), to exclude inefficient regions where photons can pass undetected and mimic the signal recoil, this selection is only applied for recoil masses below $3\,\text{GeV}/c^2$, as for larger masses the photon hypothesis is unlikely;

4. a tighter ECL-based muon selection with $0.15 <$ clusterE $< 0.4\,\text{GeV}$ and clusterE/p < 0.4;

5. we reject events where the closest reconstructed photon lies within a 15° cone from the recoil momentum;

6. a) no additional tracks in the ROE,

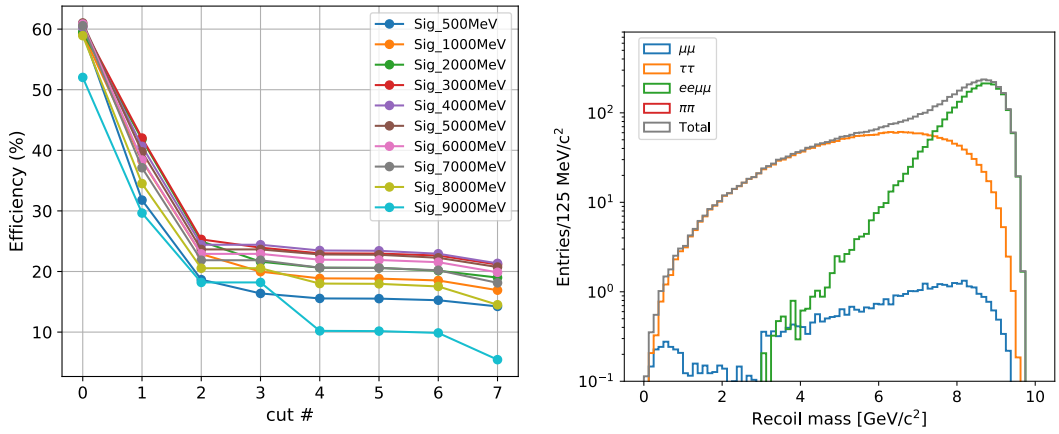

Figure 5.1.: Signal efficiencies for different Z' masses as a function of the cut number (left), remaining background candidates in recoil mass spectrum (right)

b) the dominant background contribution arises from τ pair production and as π^0 are among the most common decay products, a special π^0 was set up, where photons in the ROE are used to reconstruct $\pi^0 \to \gamma\gamma$ and the event being discarded if the diphoton invariant mass is in the range $125 < M_{\pi^0} < 145\,\text{MeV}/c^2$ and the energy in the ROE exceeds 0.2 GeV,

c) the extra energy in the ECL is required to be less than 0.4 GeV;

7. the transverse momentum of the dimuon candidate in the LAB frame satisfies $p^T_{\mu\mu} > p^T_{cut}$, where p^T_{cut} is a linearly decreasing function with the recoil mass, and its value is 1.03 GeV/c at a recoil mass of 0.5 GeV/c^2 and 0.43 GeV/c at 9 GeV/c^2.

The remaining number of background events in the recoil mass spectrum are shown on the left in Figure 5.1. For the available phase space, the main contribution is given by $\tau\tau$ events, while radiative dimuon events $\mu\mu(\gamma)$ dominate at low recoil masses and four lepton final state events $ee\mu\mu$ above 4 GeV/c^2. Other background sources have been investigated and are found to be negligible. The signal efficiencies are given on the right in Figure 5.1.

5.4.2. Mass windows and tau suppression

Recoil mass windows are defined for every generated Z' mass, centred at the nominal mass value and with a width corresponding to twice the recoil mass resolution, i.e. 2σ. The individual values for the mass resolution are obtained from the dedicated study in Section 5.5 and in particular Figure 5.8.

The guiding principle of the tau suppression algorithm is based on the different production mechanism of signal and background: whereas the Z' is radiated of a muon (similar to FSR), the invisible momentum in τ pair events, mimicking the presence of a Z', comes from neutrinos of two separate τ decays.

The following variables have been computed in the CM frame and are considered for discriminating signal and background: longitudinal and transverse missing momentum (which coincides with the Z' momentum in the signal case) w.r.t. the maximum and minimum momentum directions ($p_{rec}^{l,lmax}$, $p_{rec}^{T,lmax}$, $p_{rec}^{l,lmin}$ and $p_{rec}^{T,lmin}$), opening angles between the missing momentum and the maximum and minimum momentum muon directions, longitudinal and transverse components of the momenta the two muon candidates w.r.t. the missing momentum direction, asymmetry of the moduli of the momenta of the two muons, modulus of the sum of the two muon momenta, sum of the moduli of the two muon momenta and transverse momentum of the dimuon candidate $p_{\mu\mu}^T$.

A multivariate analysis (MVA) package (scikit-learn [44]) was used to rank all of these variables in terms of discriminating power and the final choice fell on $p_{rec}^{T,lmax}$, $p_{rec}^{T,lmin}$ and $p_{\mu\mu}^T$. An optimal separating line in the $p_{rec}^{T,lmax} - p_{rec}^{T,lmin}$ plane and an optimal cut on $p_{\mu\mu}^T$ are searched for simultaneously by looking for maximal values of a Punzi FOM (see Equation 4.6) that is set up for every mass point. The results are shown in Figure 5.2 for three different mass points 2, 5 and 7 GeV/c^2, where the optimized selection line has been superimposed. In order to obtain values for the two line parameters and the $p_{\mu\mu}^T$ cut value for a generic point in the recoil mass spectrum, a linear spline function is used to fit the distribution of the three parameters independently. The interpolated values are shown in Figure 5.3.

The number of remaining background candidates as well as the signal efficiency after the tau suppression are shown in Figure 5.4. The sharp increase in signal efficiency for $M_{rec} > 7\,\text{GeV}/c^2$ is due to the fact that signal and background distributions overlap significantly in the $p_{rec}^{T,lmax} - p_{rec}^{T,lmin}$ plane, so that the suppression algorithm fails to find an effective separating line.

The initial bin choice used so far is based on the pattern of generated Z' samples. As it doesn't cover the full recoil mass spectrum, it is not suited for the final measurement on data. A new choice of contiguous mass intervals is thus made, which is used from now on.

5.4.3. LFV Z'

The selections presented in Section 5.4.1 are applied with minor changes to selection 1 and 4:

1. the number of cleaned tracks must be equal to 2 and the cluster energy associated with the electron is required to be greater than 1.5 GeV, to emulate the functionality of the hie trigger (see Section 3.1).

4. a tighter ECL-based selection for the muon candidate with 0.15 < clusterE < 0.4 GeV and clusterE/p < 0.4 and for the electron candidate with $0.8 < clusterE/p < 1.2$.

As for the standard Z', the dominant source of background contribution arises from τ-pair events for the majority of the spectrum.

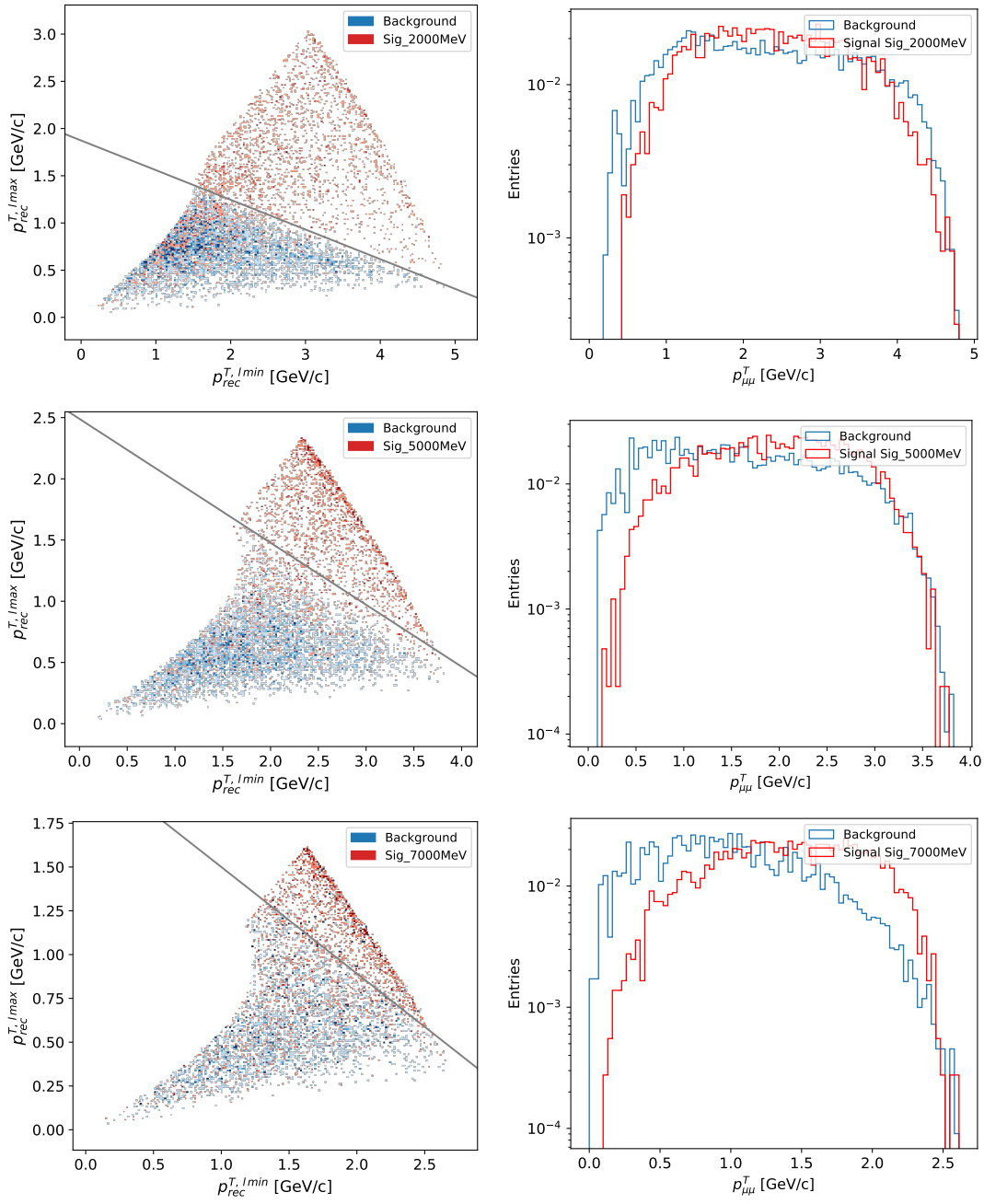

Figure 5.2.: $p_{rec}^{T,lmax}$ vs. $p_{rec}^{T,lmin}$ (left) and $p_{\mu\mu}^{T}$ (right) distributions for $M_{Z'}$ =2, 5 and 7 GeV/c^2. The optimal separation line is superimposed.

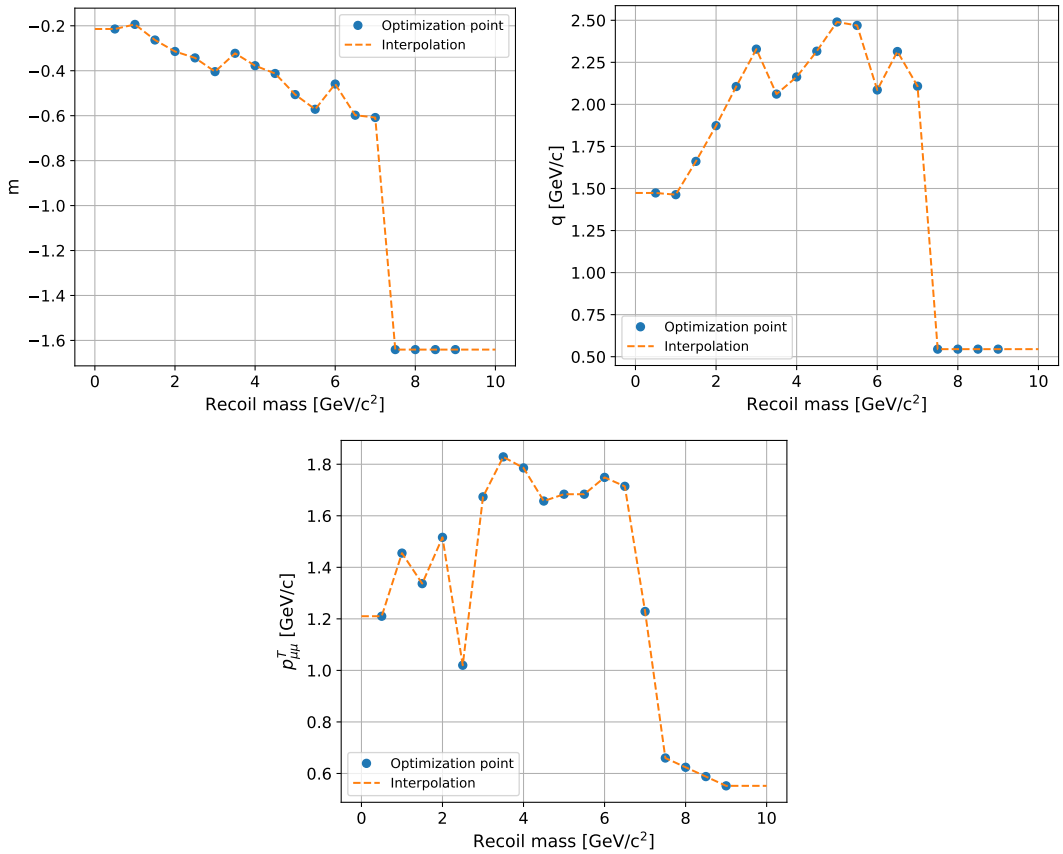

Figure 5.3.: Optimal line parameters (left:slope, middle:intercept) and $p^T_{\mu\mu}$ (right) values as function of the recoil mass. The interpolated values (linear spline) are also shown.

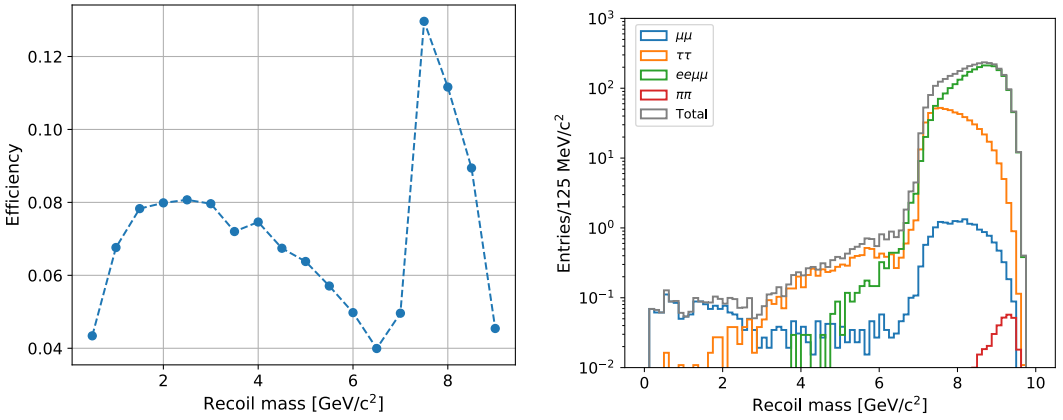

Figure 5.4.: Signal efficiency (left) and number of remaining background events (right) after all the analysis selections and the τ suppression for the standard Z'.

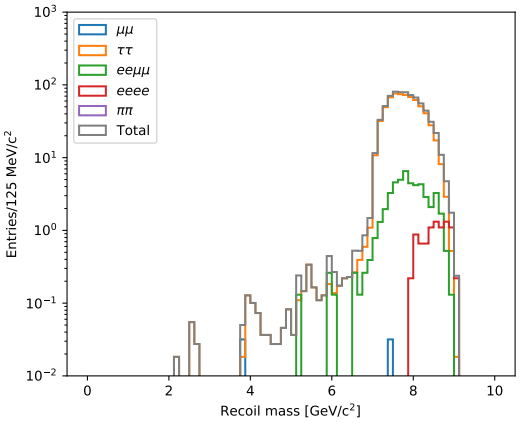

Figure 5.5.: Number of remaining background events after all the analysis selections and the τ suppression for the LFV Z' analysis.

As there was no reliable signal simulation available for the LFV Z' at the time of writing, no signal efficiency can be quoted. This also affects the tau suppression, which cannot be optimized for this channel. We therefore apply the exact same values for the selection line in the $p_{rec}^{T,lmax} - p_{rec}^{T,lmin}$ plane and optimal cut on $p_{e\mu}^{T}$ obtained in the previous section. The distribution of the surviving background events is shown in Figure 5.5. We also adopt a contiguous set of bins for the further analysis.

5.5. Signal resolution studies

We put upper limits on the Z' production cross section by using a counting technique: The number of observed events in bins of recoil mass are compared with expectations from background (see Section 5.8). The bin width is chosen to be four times the width of the signal peak ($\pm 2\sigma$), which depends on the mass of the Z'. We perform an unbinned maximum likelihood fit (using RooFit v3.6 [40]) of the recoil mass distributions to determine the width for every generated Z' signal sample. A Crystal Ball (C.B.) function is used to describe the rightmost tail of the recoil mass distribution, which is due to initial state radiation. Moreover, a Gaussian is added in order to fully describe the remaining part of the distribution. The resulting PDF consists of five parameters, as we fix the mean of both C.B. and Gaussian to the Z' mass value: $\sigma_{\text{C.B.}}$ and σ_{Gauss}, being the width of the C.B. and the Gaussian respectively; $\alpha_{\text{C.B.}}$ and $n_{\text{C.B.}}$, the remaining C.B. parameters; *frac*, the fraction of each function with respect to the normalized sum of both. The recoil mass distribution for every generated signal sample as well as the corresponding fitted PDF model distribution can be seen in Figure 5.6. As we did observe negative values for the recoil mass in case of a mass hypothesis $M_{Z'} = 0.5\,\text{GeV}/c^2$, we perform the fit algorithm on the squared recoil mass distribution. In general, we observe good fit results, concluding that the chosen PDF model is able to describe the recoil mass well.

In order to validate the fit, we perform a toy study with 1000 samples of 10000 events each. The events in every toy samples were generated according to the resulting PDF model parameters of the fit. We then look at the parameter distributions of the toy samples. In particular the mean, error and pull distribution of $\sigma_{\text{C.B.}}$ and σ_{Gauss} for $M_{Z'} = 5\,\text{GeV}/c^2$ are shown in Figure 5.7, where the respective pull distributions have been fitted with a Gaussian. As expected in case of an appropriate fit model, the resulting mean and sigma agree with 0 and 1 respectively. This is repeated for every fit parameter and every Z' mass point. Similar results are observed throughout, so that we successfully completed the validation of the fit model. Finally, the width of every recoil mass distribution is computed with Equation 4.7 and the fit results for $\sigma_{\text{C.B.}}$ and σ_{Gauss}. The weighted widths are shown in Figure 5.8 as a function of $M_{Z'}$.

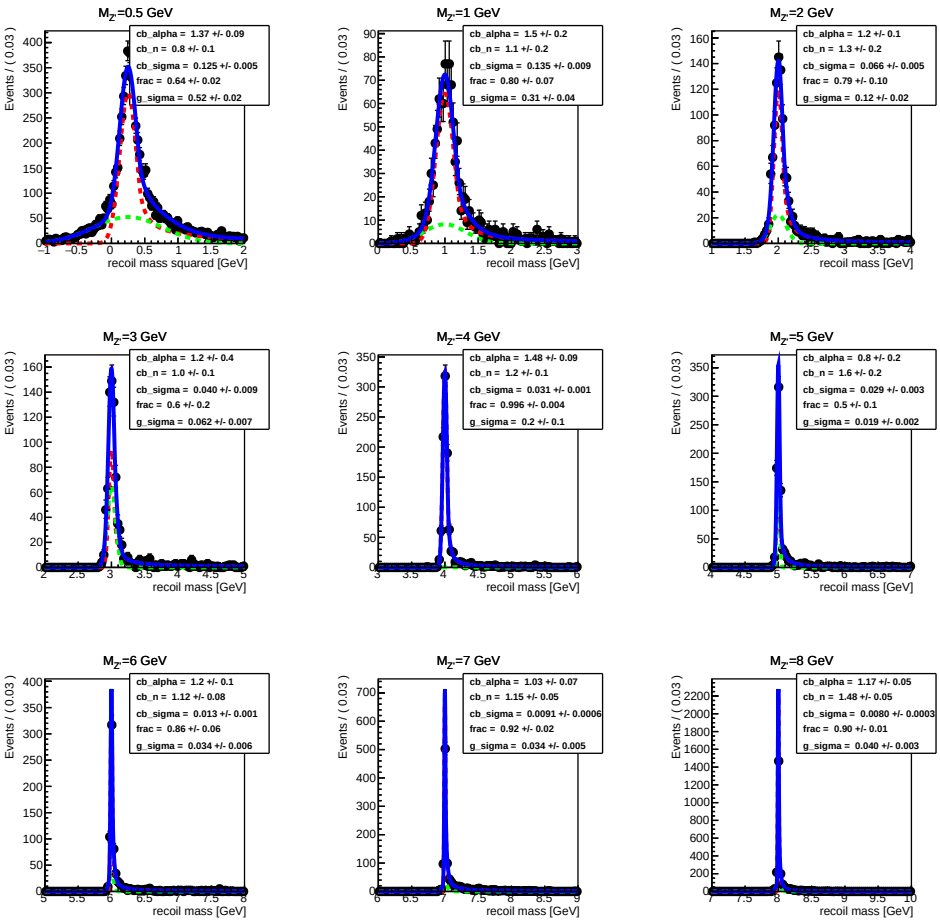

Figure 5.6.: Recoil mass and fitted PDF model distribution (blue line) for every generated signal sample. The contribution of the C.B and the Gaussian function are shown with a red and green dotted line respectively. The resulting fit parameters are shown in the top right corner of each graph.

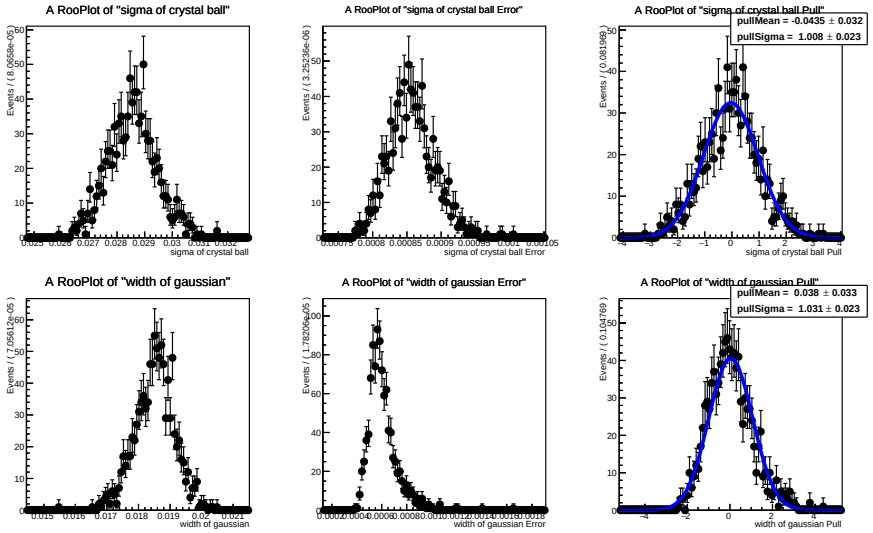

Figure 5.7.: Validation plots of $\sigma_{\text{C.B.}}$ and σ_{Gauss} for $M_{Z'} = 5\,\text{GeV}/c^2$. The pull distribution for every parameter is fitted with a Gaussian (blue line). The fit results are shown in the top right corner of the graph.

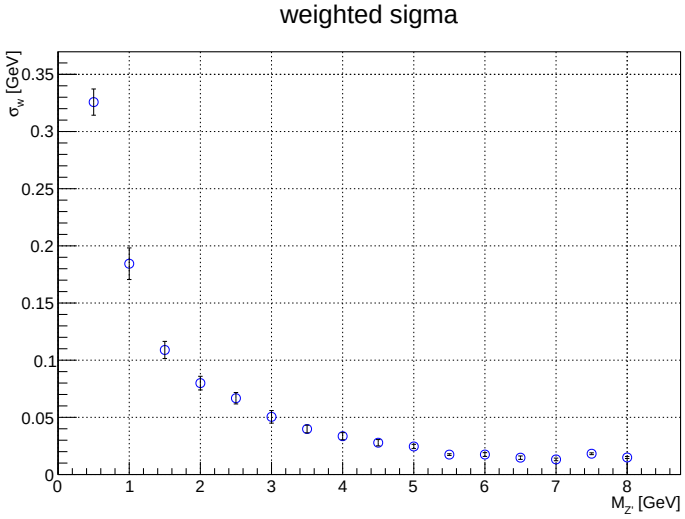

Figure 5.8.: Weighted σ_w according to Equation 4.7 vs Z' mass.

5.6. Detector effects and systematic uncertainties

The detector effects and related systematic uncertainties described in this section refer to the standard Z' case only, unless LFV Z' is explicitly mentioned.

5.6.1. Trigger selection

This analysis is performed on data events selected by the ffo trigger bit, which was introduced in Section 3.1. As we do not use the trigger simulation in the MC samples, we added the requirements of this trigger bit in the event selection, see Section 5.4.1. A dedicated study for the performance of ffo (similar to the one in Section 3.3) was done with Phase 2 data. The efficiency was found to be $(79.0 \pm 0.1)\%$ for a total integrated luminosity of $276\,\mathrm{pb}^{-1}$. However, this value only holds for events where the opening angle of the two muon tracks in the transverse plane is less than 172°. A sharp decrease of the trigger efficiency was observed for opening angle values larger than 172°, so that we adopted this additional cut in Section 5.4.1.

As what concerns the LFV Z', this search is carried out with data events selected by the hie trigger bit (Section 3.1), which requires the presence of an ECL cluster with energy $E > 1\,\mathrm{GeV}$. This is already met by our selections in Section 5.3.2, so that we do not need any further requirements to emulate the trigger bit behaviour in MC samples. The trigger efficiency of the hie bit was evaluated to be $(96 \pm 1)\%$ for the same integrated luminosity of $276\,\mathrm{pb}^{-1}$.

5.6.2. Tracking efficiency

The tracking efficiency is overestimated in MC simulation w.r.t data and depends on the track position. From dedicated studies, we expect discrepancies at the order of 5% for the tracks used in this analysis. A value of 2% is assigned as systematic uncertainty due to the tracking inefficiency not modelled in MC.

5.6.3. Particle ID selection

The performance of ECL-based variables used for particle identification (see Section 5.4.1) has been evaluated with data and MC samples. In the ECL barrel region the overall agreement was found to be at the level of 2%, so that we take this number as a systematic uncertainty.

5.6.4. Recoil mass resolution

In order to compare the recoil mass resolution in data and MC we select a sample of $e^+e^- \to \mu^+\mu^-\gamma$ events with selections 1,2,3,4 and 6 of Section 5.4.1, and reversing selection 5 to require the presence of a photon within a 0.2 rad cone of the recoil momentum direction. In addition, we required that the sum of the energies of the two muons and the photon lies in between 10 and 12 GeV and that there are no additional photons with energy larger than 100 MeV in the event.

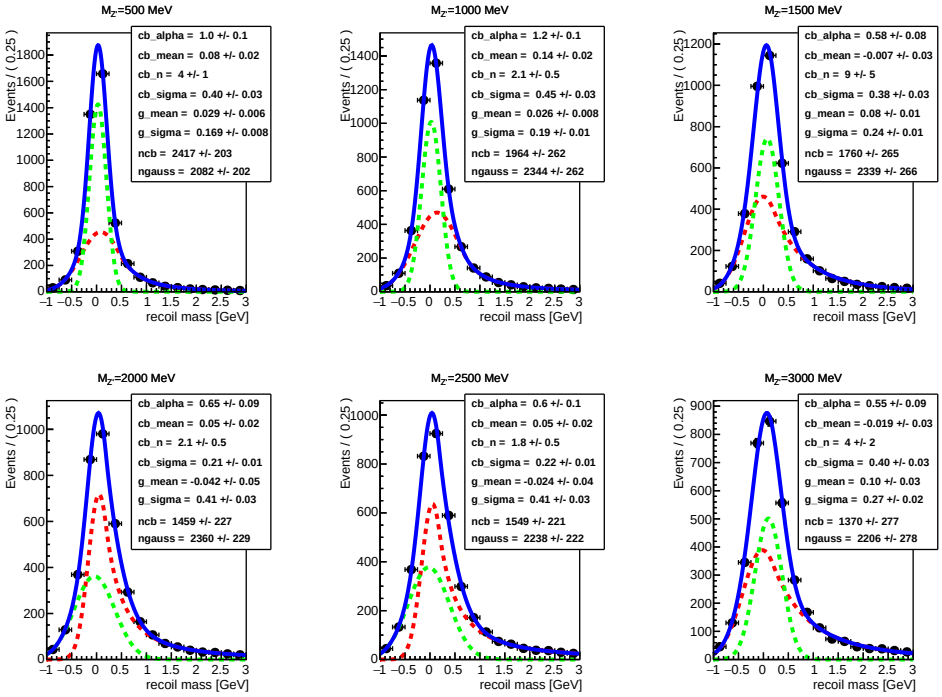

Figure 5.9.: Weighted MC recoil mass and fitted PDF model distribution (blue line) for different Z' mass point hypothesis. The contribution of the C.B and the Gaussian function are shown with a red and green dotted line respectively. The resulting fit parameters are shown in the top right corner of each graph.

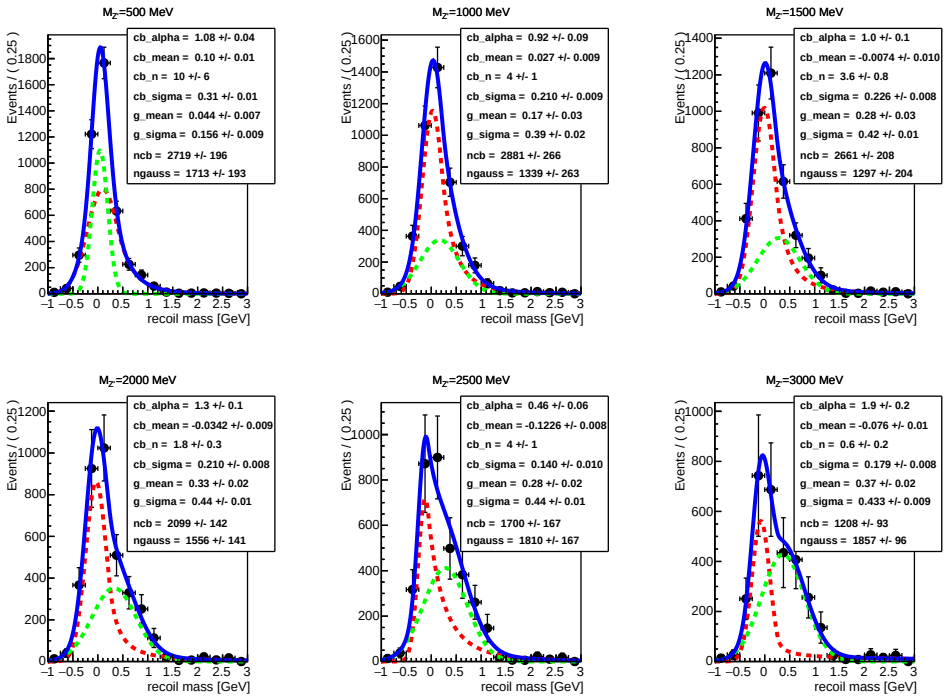

Figure 5.10.: Weighted data recoil mass and fitted PDF model distribution (blue line) for different Z' mass point hypothesis. The contribution of the C.B and the Gaussian function are shown with a red and green dotted line respectively. The resulting fit parameters are shown in the top right corner of each graph.

$M_{Z'}$ [GeV/c^2]	$\sigma_{\text{weighted,data}}$ [GeV/c^2]	$\sigma_{\text{weighted,MC}}$ [GeV/c^2]	$\frac{\sigma_{\text{weighted,data}}}{\sigma_{\text{weighted,MC}}}$	$N_{\text{events,data}}$	$N_{\text{events,MC}}$	$\frac{N_{\text{events,data}}}{N_{\text{events,MC}}}$
0.5	0.263 ± 0.012	0.298 ± 0.021	0.883 ± 0.074	4432 ± 275	4498 ± 287	0.985 ± 0.088
1	0.282 ± 0.020	0.355 ± 0.028	0.794 ± 0.084	4220 ± 374	4309 ± 371	0.979 ± 0.121
1.5	0.305 ± 0.018	0.325 ± 0.022	0.938 ± 0.084	3958 ± 291	4099 ± 375	0.966 ± 0.113
2	0.329 ± 0.018	0.302 ± 0.024	1.089 ± 0.105	3655 ± 200	3819 ± 323	0.957 ± 0.096
2.5	0.329 ± 0.013	0.314 ± 0.023	1.048 ± 0.087	3510 ± 236	3787 ± 313	0.927 ± 0.099
3	0.355 ± 0.010	0.356 ± 0.027	0.997 ± 0.081	3065 ± 134	3575 ± 392	0.857 ± 0.101

Table 5.2.: An overview of the values of the weighted width including the number of events for the fitted data and MC recoil mass distributions is given. The ratio of both values is calculated in order to determine the correction factor for detector resolution.

The general idea consists in weighting the two-dimensional muon momentum distribution according to the analogous distributions for $e^+e^- \to \mu^+\mu^- Z'$ events at different Z' masses in bins of $0.5\,\text{GeV}/c \times 0.5\,\text{GeV}/c$ size. We compute event-by-event weights which are then applied on data and MC $\mu^+\mu^-\gamma$ samples and used to produce recoil mass distributions. However, this procedure works only well for low Z' masses, as for increasing Z' masses, it becomes harder to match the two-dimensional distributions with $\mu^+\mu^-\gamma$ ones due to kinematic reasons. The weighted recoil mass distributions are expected to be centred at zero: the difference in width between data and MC can be used as a correction factor to the resolution. As was done in Section 5.5, we use the sum of a C.B. and Gaussian to fit the distributions. The results are shown in Figure 5.9 and 5.10. Correction factors, defined as the ratio of the values of the weighted widths (Equation 4.7) for data and MC recoil mass distributions from the fit are shown in Table 5.2. As they are smaller or compatible with 1, we conclude that the effect of detector resolution is in fact well described in simulations, and we may neglect the differences.

5.7. Data validation

We now compare the number of expected background events in MC simulation to the ones obtained in data samples. This allows us to check the effect of the individual analysis selections that have been introduced in Section 5.4, where we are particularly interested in the behaviour of the tau suppression procedure of Section 5.4.2. In order to avoid an accidental unblinding, we make use of control samples with similar kinematic properties than our signal signature but yet different topology:

- ee sample: Beside the contribution from Bhabha and eeee processes, this sample is dominated by $\tau\tau(\gamma)$ events, with both taus decaying to electrons and the resulting kinematics being almost identical to the major Z' analysis background ($\tau\tau(\gamma)$ with $\tau \to \mu$). All the analysis selections, except for criteria related to particle identification, and the tau suppression algorithm can thus be checked.

- $\mu\mu\gamma$ (and $e\mu\gamma$, $ee\gamma$) sample: This is particularly useful for checking the low recoil

mass region, where the $\mu\mu\gamma$ process dominates, see Figure 5.1. The two complementary $e\mu\gamma$ and $ee\gamma$ samples are used for cross-checks.

- $\mu\mu$ (and $e\mu$): where the tau suppression procedure is applied in reverse so that potential signal events are rejected, leaving an unbiased sample with only background contribution.

For every one of these samples we compare the distributions of relevant analysis variables in data and MC and compute the overall agreement in terms of data/MC ratios. This is not only done over the full mass range, but also in three recoil mass regions, each of them being dominated by different background processes: $-2 < M_{rec} < 3\,\mathrm{GeV}/c^2$ ($\mu\mu\gamma$), $3 < M_{rec} < 6\,\mathrm{GeV}/c^2$ ($\tau\tau\gamma$) and $6 < M_{rec} < 11\,\mathrm{GeV}/c^2$ ($ee\mu\mu$). While data events are selected with the requirement of the ffo trigger bit to be fired, MC expectations are scaled according to previously mentioned efficiency of ffo, i.e. 0.79 (Section 5.6.1). Samples including an electron and/or photon can alternatively be fired by the hie trigger bit, enabling further checks.

5.7.1. ee sample

Candidate events for the ee sample are reconstructed according to the criteria given in Section 5.4.1, where the ones requiring a loose ECL based muon selection are replaced with clusterE/p < 0.75. We then proceed along the description in Section 5.4.1, except for selection 4 which we change to $0.8 <$ clusterE/p < 1.2.

We find an overall good agreement with a data/MC ratio equal to 0.97 ± 0.01 in the full recoil mass spectrum. After applying the tau suppression, there are 20 events remaining in the first two recoil mass windows, while 18.4 are expected in MC. These numbers can be interpreted as a validation of the tau suppression procedure with a statistical precision of $\sim 22\%$. We assign this value as a systematic uncertainty on the background level knowledge to be used later in the upper limit computation in Section 5.8.

5.7.2. $\mu\mu\gamma$ sample

We apply the selection presented in Section 5.4.1 and require in addition the presence of a photon with a reconstructed energy of $\mathrm{E}_\gamma > 1\,\mathrm{GeV}$. Furthermore, selection 5 regarding the rejection of photons within a 15° is dropped, and selection 6, related to the extra energy requirement in the ROE is replaced by extraEnergy $- \mathrm{E}_\gamma < 0.4\,\mathrm{GeV}$. The main contributing processes to this sample are the same as the background sources in the standard Z' analysis. We then compare the recoil mass distribution in data and MC after applying all the selections (without the τ suppression procedure) in Figure 5.11 for the three different intervals. Discrepancies at the order of 30% are visible, with data being consistently below MC expectations. This is particularly evident for the first interval, largely dominated by radiative $\mu\mu\gamma$ background. The distributions of relevant analysis variables are shown in Figure 5.12. No clear evidence, which could hint at the discrepancy is observed. An overall good agreement can be seen, the only exception being the data/MC distribution of the azimuthal track angle. This is related to hardware issues

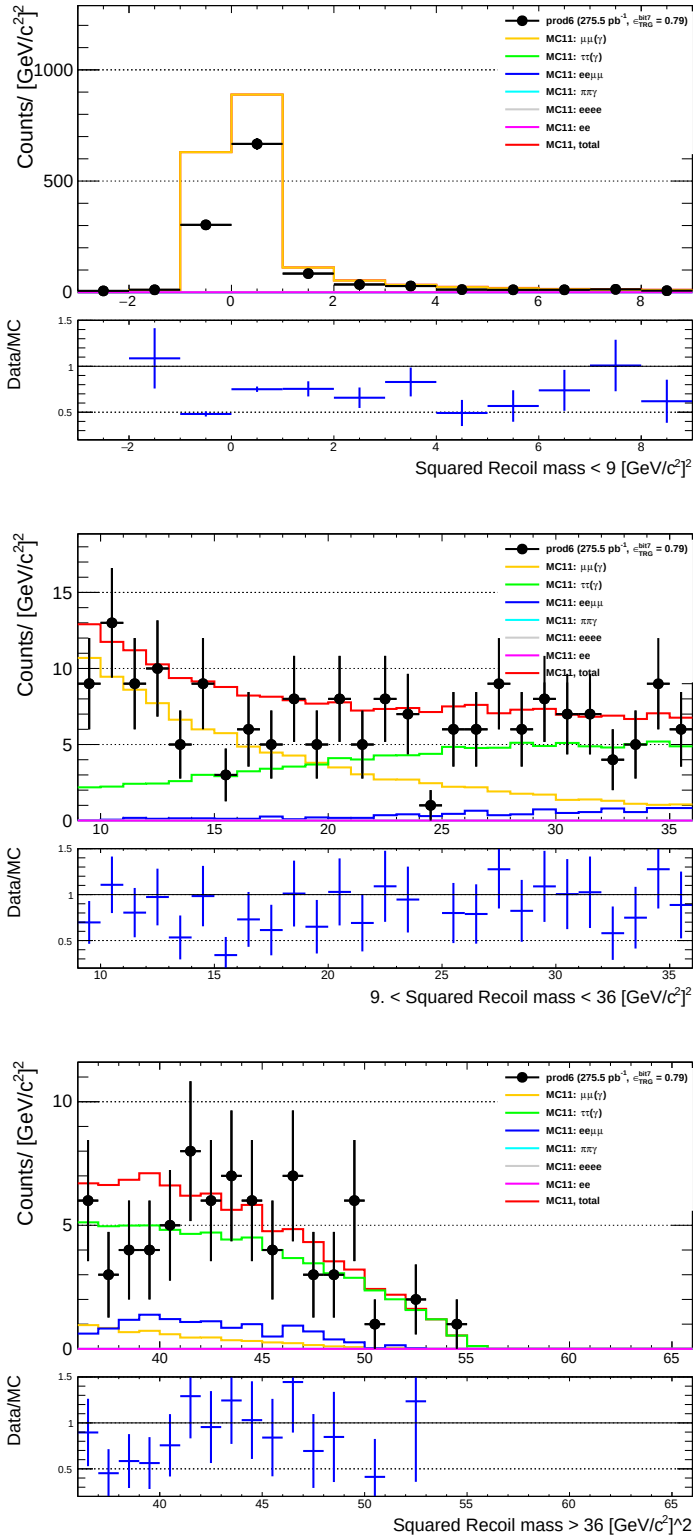

Figure 5.11.: Squared recoil mass distributions for the $\mu\mu\gamma$ validation sample.

of the CDC trigger ffo in Phase 2 which was known to produce strong ϕ dependencies. With the presence of a photon with energy above 1 GeV, we can repeat the same checks by requiring the ECL trigger bit hie to be fired instead of ffo. The results are shown in Table 5.3. We observe similar values for the data/MC agreement than in case of using ffo. We then proceed to check the $e\mu\gamma$ and $ee\gamma$ samples and present the results in Table 5.3. A much better agreement can be seen than in case of the $\mu\mu\gamma$ sample, thus suggesting that the observed discrepancy is related to muons.

5.7.3. Reversed tau suppression sample

With a partially reversed tau suppression procedure we obtain a sample which is very similar to the background sample of the standard Z' analysis. Instead of selecting events situated above the optimal separation line in the $p_{rec}^{T,lmax} - p_{rec}^{T,lmin}$ plane (see Figure 5.2), we only choose those underneath and ignore in addition the cut on $p_{\mu\mu}^{T}$. Any hypothetical Z' signal is thus strongly suppressed. The distortion in the background shape induced by this procedure was studied on the ee sample and found to be negligible. We apply this partially reversed tau suppression on the $\mu\mu$ and $e\mu$ sample before the analysis selections. Results are shown in Figure 5.13 and the associated data/MC values are given in Table 5.3. They confirm the previously observed discrepancies.

5.7.4. Data validation summary

All the results reported in the previous sections are summarized in Table 5.3. The data/MC ratios point to a discrepancy of 35% for $\mu\mu$ events and 10% for $e\mu$ events. The latter may be explained by the tracking inefficiency reported in Section 5.6.2, which was confirmed with an independent check. The remaining 25% in the two muon events could not be further clarified and needs to be taken into account in the systematic uncertainty evaluation.

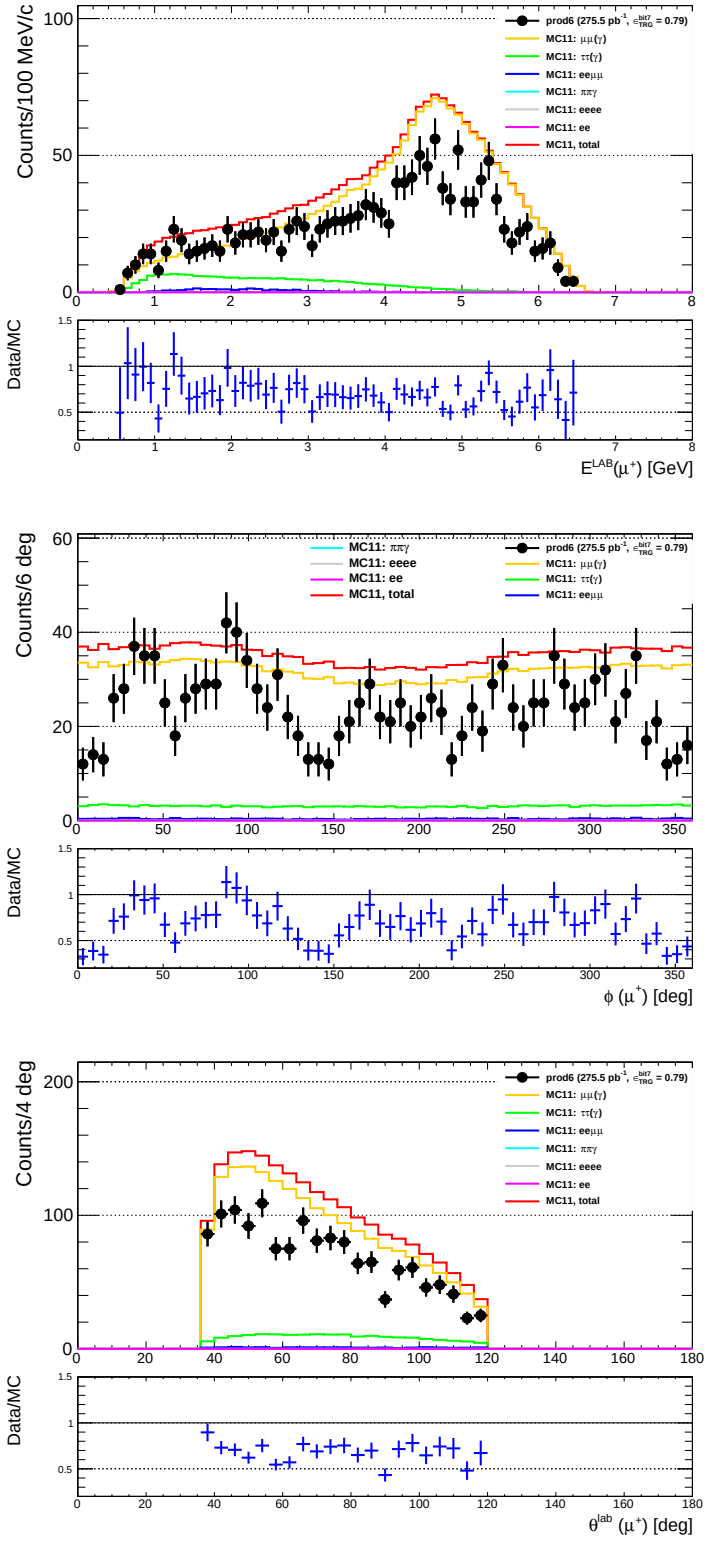

Figure 5.12.: Energy, azimuthal angle ϕ and polar angle θ distributions for the positive muon track in $\mu\mu\gamma$ validation sample.

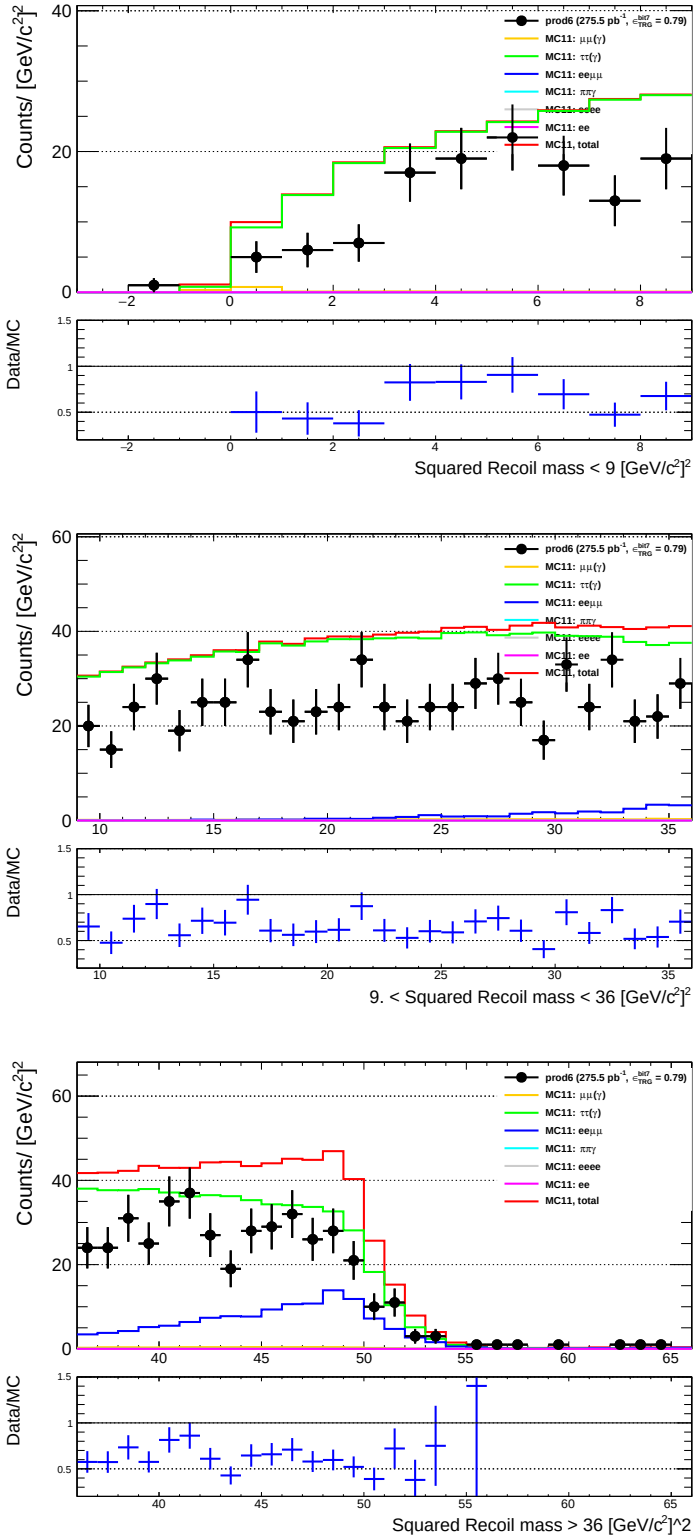

Figure 5.13.: Squared recoil mass distributions for the $\mu\mu$ validation sample with a partially reversed τ suppression procedure.

Mass window [GeV/c^2]	$\mu\mu\gamma$	$\mu\mu\gamma$	$e\mu\gamma$	$e\mu\gamma$	$ee\gamma$	$ee\gamma$	$\mu\mu$+anti τ	$e\mu$+ anti τ
-	ffo	hie	ffo	hie	ffo	hie	ffo	ffo
-2 $\div$ 3	0.65±0.02	0.67±0.02	0.8±0.3	1.3±0.3	0.88±0.01	0.99±0.01	0.66±0.06	0.94±0.07
3 $\div$ 6	0.84±0.07	0.76±0.07	0.9±0.1	0.95±0.13	1.10±0.10	1.14±0.01	0.65±0.02	0.89±0.03
6 $\div$ 11	0.9±0.1	0.72±0.13	0.9±0.2	0.93±0.15	2.13±0.12	1.3±0.1	0.63±0.03	0.89±0.03
Overall	0.68±0.02	0.68±0.02	0.92±0.09	0.96±0.10	0.90±0.01	0.99±0.01	0.64±0.02	0.90±0.02

Table 5.3.: Summary of the validation checks for the data/Monte Carlo ratio on the various samples. The second row shows the trigger line used in the check. Data/MC ratios are shown for three different recoil mass intervals and for the total spectrum.

Source	Error
Trigger efficiency	4%
Tracking efficiency	4%
PID	4%
luminosity	1.5%
τ suppression (background)	22%
discrepancy in muon yields (background)	2%
discrepancy in muon yields (signal efficiency)	12.5%

Table 5.4.: List of systematic uncertainties.

5.8. Statistical interpretation

The statistical interpretation of both the standard and LFV Z' search is achieved with a Bayesian approach.

The systematic uncertainties related to trigger and tracking efficiency, and particle identification selection are considered to affect signal efficiency and background expectation in a correlated way. The same holds for the uncertainty of a luminosity measurement, that was carried out by the Belle II collaboration. Due to the effect of the tau suppression procedure (see Section 5.7.1), we assign a value of 22% for this systematic uncertainty to the background only. The data validation in Section 5.7 showed a discrepancy of 35% with MC simulation, where only 10% could be accounted for by tracking efficiency. The background level and the signal efficiency are thus scaled down by 35% w.r.t the MC expectations. Different systematic uncertainties were assigned due to this effect. We assume that the validation with a reversed τ suppression in Section 5.7.3 gives a reliable estimate of the background, and we therefore assign the statistical uncertainty of this measurement, $\pm 2\%$ (see Table 5.3) as a systematic error. Finally, we assign half of the size of the remaining discrepancy, 12.5%, to the signal efficiency as a systematic uncertainty from an unknown source. All the values are given in Table 5.4

We make use of the Bayesian Analysis Toolkit (BAT) [41] and make the following assumptions for the priors and distributions involved:

- the likelihood of the observed number of events is assumed to be Poissonian;
- the prior distribution for the Z' cross section was assumed to be flat between 0 and 1×10^5 fb;
- all the distributions related to systematic uncertainties are modelled with Gaussian functions, with a width equal to the estimated size of the effect;
- the expected number of background events is assumed to be Poissonian.

In case of the standard Z' analysis, the following equation holds:

$$N_{obs} = \sigma_{Z'} \times \mathcal{L} \times \epsilon_{sig} + B_{exp} \tag{5.1}$$

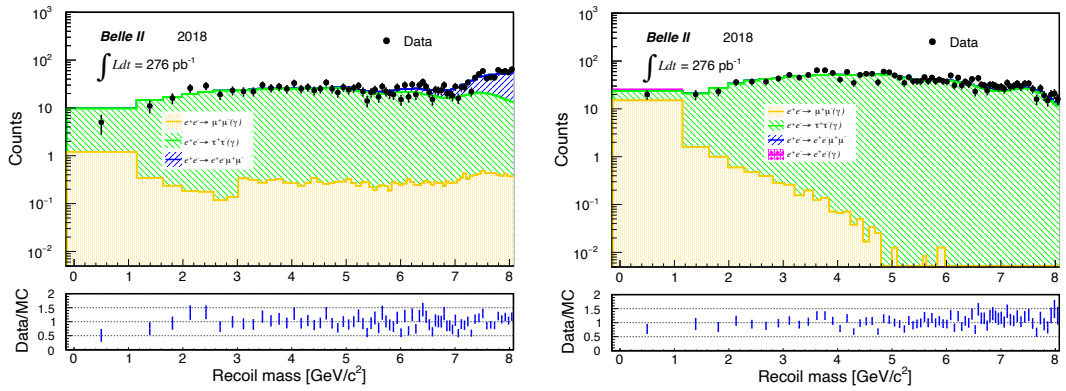

Figure 5.14.: Recoil mass spectrum for the $\mu\mu$ (left) and $e\mu$ (right) sample before the τ suppression procedure. MC values are scaled for luminosity and trigger efficiency (0.79 and 0.96) and validation procedure outcome (0.65 and 0.9).

where N_{obs} is the number of observed events, ϵ_{sig} is the signal efficiency rescaled by 35%, B_{exp} is the expected background rescaled by 35%. With the previous assumptions, the BAT toolkit can estimate the 90% CL upper limit on the cross section $\sigma_{Z'}$ by means of Equation 5.1. We may compute in addition our expected sensitivity on $\sigma_{Z'}$, defined as the average upper limit obtained by an ensemble of pseudo-experiments with the expected background B_{exp} and no signal.

In the absence of a signal model, we cannot estimate the signal efficiency for the LFV Z' and need to use a slightly modified version of Equation 5.1, in which $\sigma_{Z'} \times \epsilon_{sig}$ must be considered as single parameter. We apply the same procedures and considerations as before and rescale the expected number of background events by 10%.

The final results together with the expected sensitivities are shown in the next section 5.9.

5.9. Results and Outlook

After the unblinding of the $\mu\mu$ and $e\mu$ samples, we perform the final measurement on data using the techniques shown in Section 5.7 and 5.8.

As a first step, we check the assumptions made in Section 5.7.3, where we derived scaling factors for the MC expectations with a partially reversed τ suppression procedure. In Figure 5.14 the recoil mass spectra for the unblinded $\mu\mu$ and $e\mu$ samples are shown before the application of the τ suppression and MC values were scaled to take into account the trigger efficiency (0.79 for $\mu\mu$ and 0.96 for $e\mu$) and the result of the validation procedure (0.65 and 0.9 respectively). The agreement looks overall good.

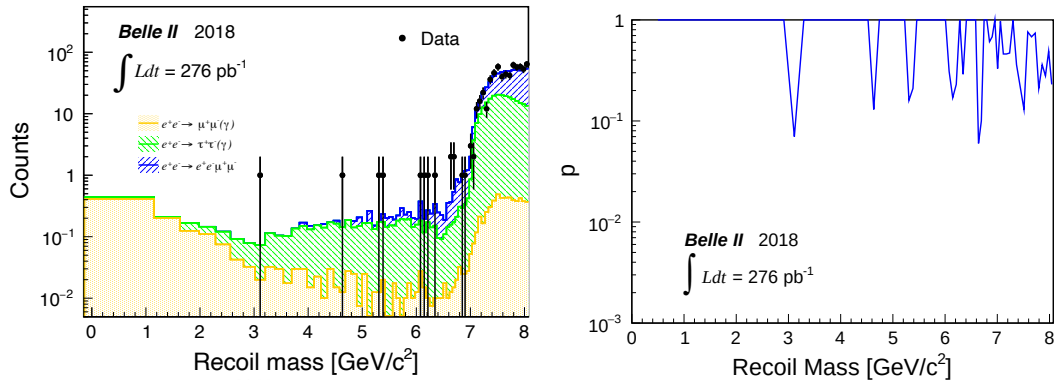

Figure 5.15.: Recoil mass spectrum after unblinding for $\mu\mu$ sample (left), where MC values are scaled for luminosity and trigger efficiency (0.79) as well as for the validation procedure outcome (0.65); p-values as a function of the recoil mass (right)

5.9.1. Standard Z'

The recoil mass spectrum after the τ suppression for the $\mu\mu$ sample is shown on the left in Figure 5.15. We first check the background only hypothesis by defining p-values as the probability to get a result greater or equal than the observed one. The results are shown on the right in Figure 5.15, where both statistical and systematic uncertainties are taken into account. No anomaly is observed, with all the results standing well below the 3σ equivalent level. Results for the 90% CL upper limits on $\sigma(e^+e^- \to \mu^+\mu^-\,\text{invisible})$ are shown in Figure 5.16. The cross section results can then be translated in terms of upper limits on the coupling constant g' in Figure 5.17.

5.9.2. LFV Z'

As before, we apply the τ suppression procedure on the unblinded $e\mu$ sample and present the recoil mass spectrum in Figure 5.18. The background only hypothesis is again checked with p-values, which are shown on the right in Figure 5.18. No anomaly is observed. Results for 90% CL upper limits on $\epsilon \times \sigma\,[e^+e^- \to e^\pm\mu^\mp\,\text{invisible}]$ are finally given in Figure 5.19.

5.9.3. Outlook

Even though no excess has been observed in both searches, these measurements allowed to demonstrate the capability of the Belle II detector to perform studies of events in which final states are only partially reconstructed. On top that, only data recorded during the commissioning phase was used for the analysis. It will therefore be worthwhile to repeat these measurements in the near future for different reasons. At the time of writing, the Belle II detector has collected a data set of $\mathcal{L} = 213\,\text{fb}^{-1}$, leading to much higher statistics. The identification of muons with information provided by the KLM instead of ECL-based

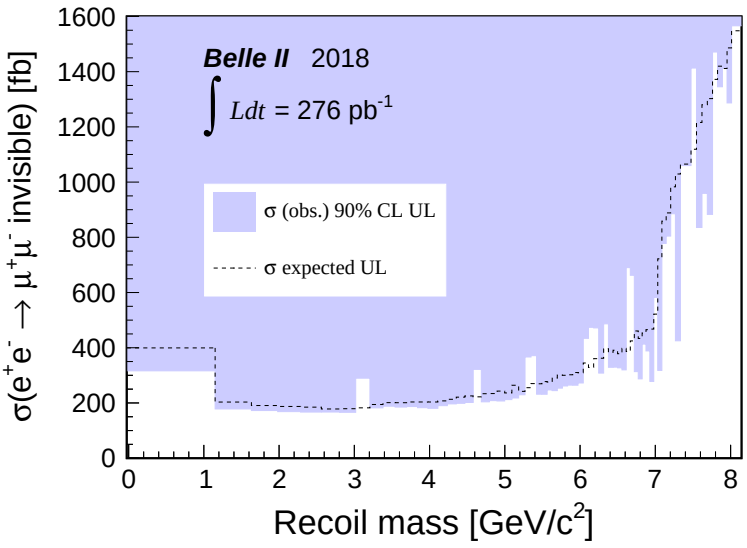

Figure 5.16.: 90% CL upper limits to $\sigma(e^+e^- \to \mu^+\mu^-$ invisible). The dashed line shows the expected sensitivity.

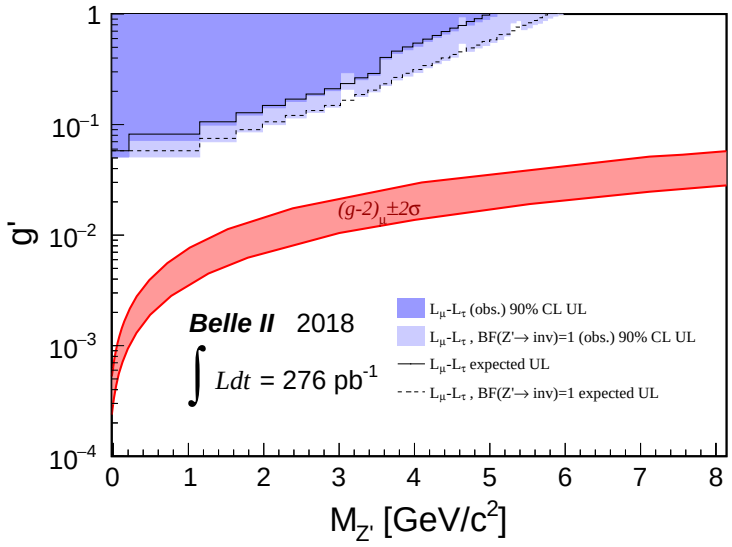

Figure 5.17.: 90% CL upper limits on coupling constant g'. Dark blue filled areas show the exclusion regions for g' at 90% CL, assuming the $L_\mu - L_\tau$ predicted BF for $Z' \to$ invisible; light blue areas are for BF($Z' \to$ invisible)=1. The solid and dashed lines are the expected sensitivities in the two hypotheses. The red band shows the region that could explain the muon anomalous magnetic moment $(g-2)_\mu \pm 2\sigma$.

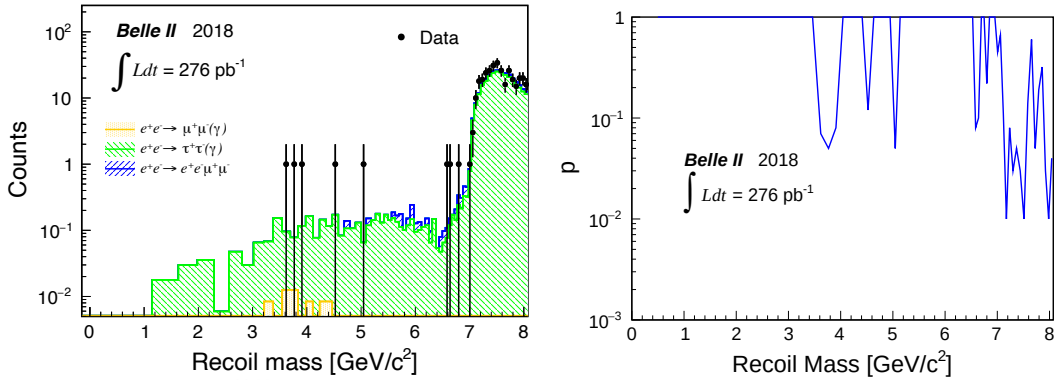

Figure 5.18.: Recoil mass spectrum after unblinding for $e\mu$ sample (left), where MC values are scaled for luminosity and trigger efficiency (0.96) as well as for the validation procedure outcome (0.9); p-values as a function of the recoil mass (right)

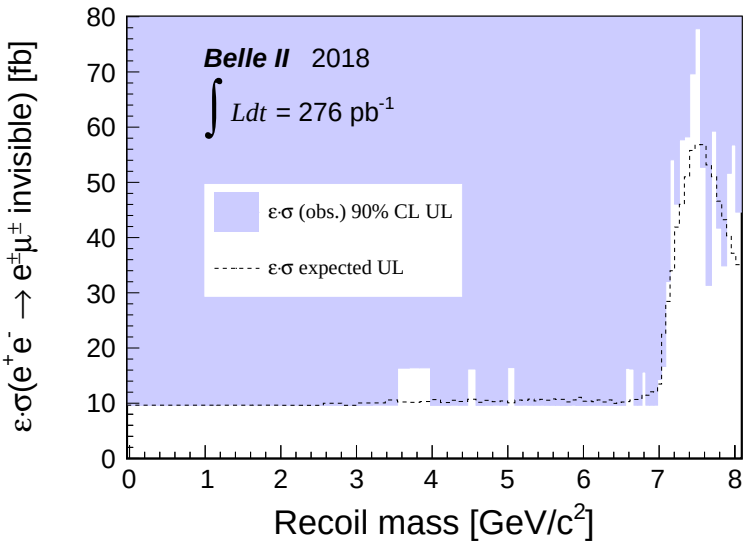

Figure 5.19.: 90% CL upper limits on efficiency times cross section $\epsilon \times \sigma\,[e^+e^- \to e^\pm\mu^\mp \text{ invisible}]$. The dashed line shows the expected sensitivity.

variables will increase the purity of the candidate events. Since the commissioning run, a deeper knowledge of the detector has been gained, so that systematic effects can be reduced. Finally, with the use of more advanced MVA tools, it will be possible to cover non-trivial regions of the phase space and possibly probe the $g-2$ band.

Conclusion

In my thesis, I presented two dark sector searches that have been performed with data collected by the Belle II detector. The experimental signature in both cases was given by a pair of muons plus large missing energy. These two physics analysis were preceded by a performance study of the Belle II trigger system.

I studied several CDC trigger lines, each of them activated by at least two tracks reconstructed in the drift chamber with a minimal opening angle. Their respective efficiencies were evaluated to be at the order of 85-90%. In addition, different dependencies of the trigger efficiency w.r.t angular variables and track parameters have been investigated and assigned as a systematic uncertainty to the overall efficiency value. A complementary approach to trigger on a two-muon-track signature is given by the KLM trigger. The latter was observed to be less performant, while multiple dependencies related to the detector geometry were found. While all the previous results were measured with data samples, a reliable trigger simulation in MC samples is crucial. The performance of TSIM was studied for the CDC trigger lines, where comparable results were found. Finally, I studied the impact of several analysis-specific cuts on the trigger efficiency in anticipation of the following two dark sector searches.

In the measurement of the Dark Higgsstrahlung process, I have been searching for the simultaneous production of a dark photon and a dark Higgs, in which the former decays into two muons and the latter is long-lived and escapes detection. A signal may then be identified by a peak in the two-dimensional distribution of the dimuon and recoil mass. After applying different selection criteria in order to reduce background contribution from SM processes, candidate events were organized in two-dimensional mass windows. The remaining background contamination was suppressed with a dedicated procedure based solely on kinematic features and the helicity angle. With the usage of two control samples, the whole analysis procedure was validated, where an overall good data/MC agreement was observed. Various systematic uncertainties related to the detector performance and analysis methods have then been considered and evaluated to be at the order of 6% for signal and background respectively. A Bayesian approach was chosen for the final statistical interpretation of the measurement, while the Look-Elsewhere-Effect arising from the high number of mass windows was expressed in terms of Bayes factors. As the measurement was not finalized at the time of writing, only a sensitivity estimate based on MC samples was provided, predicting this search to probe non-trivial regions in the phase space of kinetic mixing parameter times dark coupling constant.

In the second search, I focused on the invisible decays of a light Z' boson belonging either to a $L_\mu - L_\tau$ symmetry or coupling to all leptons, while also being sensitive to LFV effects. For both measurements, the signature is given by a bump in the recoil mass distribution. As background contributions arise from the same SM processes as for the

previous search, a similar set of selection criteria have been identified. A dedicated tau suppression procedure was deployed to suppress the most dominant background source, based on the different production mechanism of signal and background, and using MVA techniques. This method turned out to be only effective in the low recoil mass region. During the data validation, a discrepancy of 25% was discovered for $\mu\mu$ events, which could not further be clarified. Half of the value was assigned as a systematic uncertainty in addition to other effects caused by the detector and τ suppression procedure. After unblinding, a Bayesian approach was applied for the computation of upper limits with the data collected during the commissioning run. While 90% CL upper limits on the production cross section were calculated for both the LFV and standard Z', upper limits on the coupling constant g' were computed in addition for the latter.

Bibliography

[1] Catherine Heymans. *The Dark Universe*. 2399-2891. IOP Publishing, 2017. ISBN: 978-0-7503-1373-5. DOI: 10.1088/978-0-7503-1373-5. URL: http://dx.doi.org/10.1088/978-0-7503-1373-5.

[2] H. Merkel et al. "Search for Light Gauge Bosons of the Dark Sector at the Mainz Microtron". In: *Phys. Rev. Lett.* 106 (25 June 2011), p. 251802. DOI: 10.1103/PhysRevLett.106.251802.

[3] H. Merkel et al. "Search at the Mainz Microtron for Light Massive Gauge Bosons Relevant for the Muon $g-2$ Anomaly". In: *Phys. Rev. Lett.* 112 (22 2014), p. 221802. DOI: 10.1103/PhysRevLett.112.221802.

[4] S. Abrahamyan et al. "Search for a New Gauge Boson in Electron-Nucleus Fixed-Target Scattering by the APEX Experiment". In: *Phys. Rev. Lett.* 107 (19 2011), p. 191804. DOI: 10.1103/PhysRevLett.107.191804.

[5] P. Adlarson et al. "Search for a dark photon in the $\pi^0 \to e^+e^-\gamma$ decay". In: *Physics Letters B* 726.1 (2013), pp. 187–193. DOI: 10.1016/j.physletb.2013.08.055.

[6] G. Agakishiev et al. "Searching a dark photon with HADES". In: *Physics Letters B* 731 (2014), pp. 265–271. DOI: 10.1016/j.physletb.2014.02.035.

[7] D. Babusci et al. "Limit on the production of a light vector gauge boson in Φ meson decays with the KLOE detector". In: *Physics Letters B* 720.1 (2013), pp. 111–115. DOI: 10.1016/j.physletb.2013.01.067.

[8] D. Babusci et al. "Search for light vector boson production in $e^+e^- \to \mu^+\mu^-\gamma$ interactions with the KLOE experiment". In: *Physics Letters B* 736 (2014), pp. 459–464. DOI: 10.1016/j.physletb.2014.08.005.

[9] A. Anastasi et al. "Limit on the production of a new vector boson in $e^+e^- \to U\gamma$, $U \to \pi^+\pi^-$ with the KLOE experiment". In: *Physics Letters B* 757 (2016), pp. 356–361. DOI: 10.1016/j.physletb.2016.04.019.

[10] A. Anastasi et al. "Limit on the production of a low-mass vector boson in $e^+e^- \to U\gamma$, $U \to e^+e^-$ with the KLOE experiment". In: *Physics Letters B* 750 (2015), pp. 633–637. DOI: 10.1016/j.physletb.2015.10.003.

[11] A. Anastasi et al. "Combined limit on the production of a light gauge boson decaying into $\mu^+\mu^-$ and $\pi^+\pi^-$". In: *Physics Letters B* 784 (2018), pp. 336–341. DOI: 10.1016/j.physletb.2018.08.012.

[12] J. P. Lees et al. "Search for a Dark Photon in e^+e^- Collisions at BaBar". In: *Phys. Rev. Lett.* 113 (20 2014), p. 201801. DOI: 10.1103/PhysRevLett.113.201801.

[13] M. Ablikim et al. "Dark photon search in the mass range between 1.5 and 3.4 GeV/c2". In: *Physics Letters B* 774 (2017), pp. 252–257. DOI: 10.1016/j.physletb.2017.09.067.

[14] R. Aaij et al. "Search for $A' \to \mu^+\mu^-$ Decays". In: *Phys. Rev. Lett.* 124 (4 2020), p. 041801. DOI: 10.1103/PhysRevLett.124.041801.

[15] E Kou et al. "The Belle II Physics Book". In: *Progress of Theoretical and Experimental Physics* 2019.12 (Dec. 2019). ISSN: 2050-3911. DOI: 10.1093/ptep/ptz106. URL: http://dx.doi.org/10.1093/ptep/ptz106.

[16] Brian Batell, Maxim Pospelov, and Adam Ritz. "Probing a Secluded U(1) at B-factories". In: *Phys. Rev. D* 79 (2009), p. 115008. DOI: 10.1103/PhysRevD.79.115008. arXiv: 0903.0363 [hep-ph].

[17] J. P. Lees et al. "Search for Low-Mass Dark-Sector Higgs Bosons". In: *Phys. Rev. Lett.* 108 (21 2012), p. 211801. DOI: 10.1103/PhysRevLett.108.211801.

[18] I. Jaegle et al. "Search for the Dark Photon and the Dark Higgs Boson at Belle". In: *Phys. Rev. Lett.* 114 (21 2015), p. 211801. DOI: 10.1103/PhysRevLett.114.211801.

[19] A. Anastasi et al. "Search for dark Higgsstrahlung in $e^+e^- \to \mu^+\mu^-$ and missing energy events with the KLOE experiment". In: *Physics Letters B* 747 (2015), pp. 365–372. DOI: 10.1016/j.physletb.2015.06.015.

[20] Brian Shuve and Itay Yavin. "Dark matter progenitor: Light vector boson decay into sterile neutrinos". In: *Physical Review D* 89.11 (June 2014). ISSN: 1550-2368. DOI: 10.1103/physrevd.89.113004. URL: http://dx.doi.org/10.1103/PhysRevD.89.113004.

[21] Wolfgang Altmannshofer et al. "Explaining dark matter and B decay anomalies with an $L_\mu - L_\tau$ model". In: *JHEP* 12 (2016), p. 106. DOI: 10.1007/JHEP12(2016)106. arXiv: 1609.04026 [hep-ph].

[22] B. Abi et al. "Measurement of the Positive Muon Anomalous Magnetic Moment to 0.46 ppm". In: *Phys. Rev. Lett.* 126 (14 Apr. 2021), p. 141801. DOI: 10.1103/PhysRevLett.126.141801. URL: https://link.aps.org/doi/10.1103/PhysRevLett.126.141801.

[23] Roel Aaij et al. "Test of lepton universality in beauty-quark decays". In: (Mar. 2021). arXiv: 2103.11769 [hep-ex].

[24] J. P. Lees et al. "Search for a muonic dark force at BABAR". In: *Phys. Rev. D* 94.1 (2016), p. 011102. DOI: 10.1103/PhysRevD.94.011102. arXiv: 1606.03501 [hep-ex].

[25] Albert M Sirunyan et al. "Search for an $L_\mu - L_\tau$ gauge boson using Z$\to 4\mu$ events in proton-proton collisions at $\sqrt{s} = 13$ TeV". In: *Phys. Lett. B* 792 (2019), pp. 345–368. DOI: 10.1016/j.physletb.2019.01.072. arXiv: 1808.03684 [hep-ex].

[26] David Curtin et al. "Illuminating Dark Photons with High-Energy Colliders". In: *JHEP* 02 (2015), p. 157. DOI: 10.1007/JHEP02(2015)157. arXiv: 1412.0018 [hep-ph].

[27] Kazunori Akai, Kazuro Furukawa, and Haruyo Koiso. "SuperKEKB collider". In: *Nuclear Instruments and Methods in Physics Research Section A: Accelerators, Spectrometers, Detectors and Associated Equipment* 907 (Nov. 2018), pp. 188–199. ISSN: 0168-9002. DOI: 10.1016/j.nima.2018.08.017. URL: http://dx.doi.org/10.1016/j.nima.2018.08.017.

[28] SuperB Collaboration. *SuperB: A High-Luminosity Asymmetric e+ e- Super Flavor Factory. Conceptual Design Report*. 2007. arXiv: 0709.0451 [hep-ex].

[29] P. M. Lewis et al. "First Measurements of Beam Backgrounds at SuperKEKB". In: *Nucl. Instrum. Meth. A* 914 (2019), pp. 69–144. DOI: 10.1016/j.nima.2018.05.071. arXiv: 1802.01366 [physics.ins-det].

[30] T. Abe et al. *Belle II Technical Design Report*. 2010. arXiv: 1011.0352 [physics.ins-det].

[31] J. Kemmer and G. Lutz. "New detector concepts". In: *Nuclear Instruments and Methods in Physics Research Section A: Accelerators, Spectrometers, Detectors and Associated Equipment* 253.3 (1987), pp. 365–377. ISSN: 0168-9002. DOI: https://doi.org/10.1016/0168-9002(87)90518-3. URL: https://www.sciencedirect.com/science/article/pii/0168900287905183.

[32] Valerio Bertacchi et al. "Track finding at Belle II". In: *Comput. Phys. Commun.* 259 (2021), p. 107610. DOI: 10.1016/j.cpc.2020.107610. arXiv: 2003.12466 [physics.ins-det].

[33] Christoph Schwanda et al. "Performance of the Belle II Silicon Vertex Detector". In: *PoS* Vertex2019 (2020), p. 014. DOI: 10.22323/1.373.0014.

[34] Umberto Tamponi. *The TOP counter of Belle II: status and first results*. 2018. arXiv: 1811.04532 [hep-ex].

[35] Peter Križan, Samo Korpar, and Toru Iijima. "Study of a nonhomogeneous aerogel radiator in a proximity focusing RICH detector". In: *Nuclear Instruments and Methods in Physics Research Section A: Accelerators, Spectrometers, Detectors and Associated Equipment* 565.2 (Sept. 2006), pp. 457–462. ISSN: 0168-9002. DOI: 10.1016/j.nima.2006.05.233. URL: http://dx.doi.org/10.1016/j.nima.2006.05.233.

[36] S. Longo et al. "CsI(Tl) pulse shape discrimination with the Belle II electromagnetic calorimeter as a novel method to improve particle identification at electron–positron colliders". In: *Nuclear Instruments and Methods in Physics Research Section A: Accelerators, Spectrometers, Detectors and Associated Equipment* 982 (Dec. 2020), p. 164562. ISSN: 0168-9002. DOI: 10.1016/j.nima.2020.164562. URL: http://dx.doi.org/10.1016/j.nima.2020.164562.

[37] J. Alwall et al. "The automated computation of tree-level and next-to-leading order differential cross sections, and their matching to parton shower simulations". In: *JHEP* 07 (2014), p. 079. DOI: 10.1007/JHEP07(2014)079.

[38] LeptonID group and Belle II Collaboration. "Muon and electron identification efficiencies and hadron-lepton mis-identification rates at Belle II for Moriond 2021". In: (Mar. 2021). For Moriond 2021.

[39] Giovanni Punzi. "Sensitivity of searches for new signals and its optimization". In: *eConf* C030908 (2003). Ed. by L. Lyons, R. P. Mount, and R. Reitmeyer, MODT002. arXiv: physics/0308063.

[40] Wouter Verkerke and David P. Kirkby. "The RooFit toolkit for data modeling". In: *eConf* C0303241 (2003). Ed. by L. Lyons and Muge Karagoz, MOLT007. arXiv: physics/0306116.

[41] Allen Caldwell, Daniel Kollár, and Kevin Kröninger. "BAT – The Bayesian analysis toolkit". In: *Computer Physics Communications* 180.11 (Nov. 2009), pp. 2197–2209. ISSN: 0010-4655. DOI: 10.1016/j.cpc.2009.06.026. URL: http://dx.doi.org/10.1016/j.cpc.2009.06.026.

[42] David J. C. MacKay. *Information Theory, Inference & Learning Algorithms*. USA: Cambridge University Press, 2002. ISBN: 0521642981.

[43] James Berger et al. "Objective Bayesian Methods for Model Selection: Introduction and Comparison". In: *Lecture Notes-Monograph Series* 38 (Jan. 2001), pp. 135–207. DOI: 10.2307/4356165.

[44] F. Pedregosa et al. "Scikit-learn: Machine Learning in Python". In: *Journal of Machine Learning Research* 12 (2011), pp. 2825–2830.